02
October 2019
Volume 1 Issue 2

Semiconductor Science and Information Devices

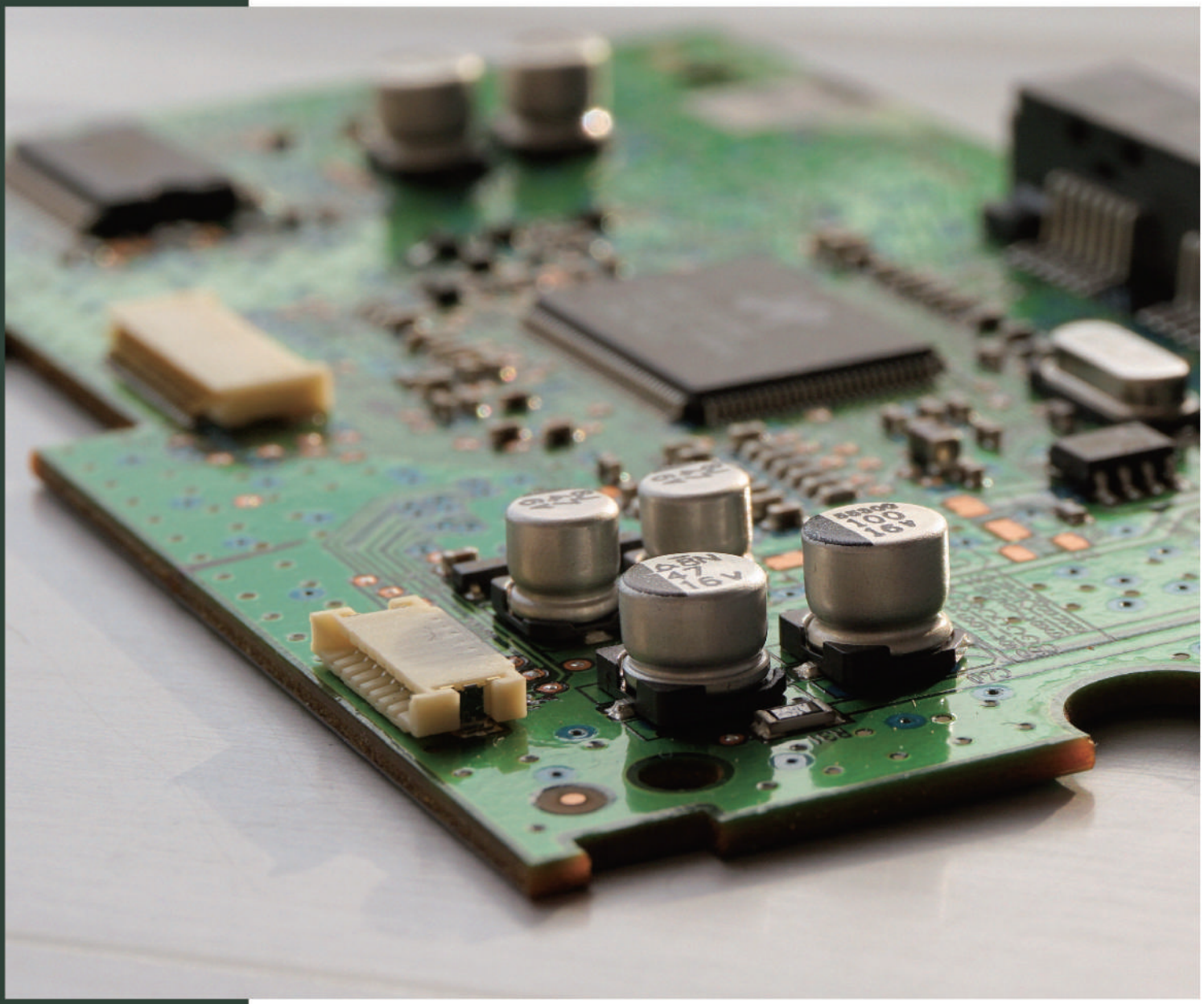

BILINGUAL PUBLISHING CO.
Pioneer of Global Academics Since 1984

APSCI | creative commons | CNKI 中国知网 www.cnki.net 中国知识基础设施工程
Google scholar | Crossref | MyScienceWork

Volume 1 | Issue 2 | 2019 October | ISSN 2661-3212 (Online)

ISSN 2661-3212 02
9 772661 321190
Price: S$30.00

Volume 1 Issue 2 • October 2019 • ISSN 2661-3212 (Online)

Semiconductor Science and Information Devices

BILINGUAL PUBLISHING CO.
Pioneer of Global Academics Since 1984

BILINGUAL PUBLISHING CO.
Pioneer of Global Academics Since 1984

Volume 1 | Issue 2 | October 2019 | Page 1-57
Semiconductor Science and Information Devices

Contents

Article

BILINGUAL PUBLISHING CO.
Pioneer of Global Academics Since 1984

Semiconductor Science and Information Devices
https://ojs.bilpublishing.com/index.php/ssid

ARTICLE

Heuristic Order Reduction of NARX-OBF models Applied to Nonlinear System Identification

Elder Oroski[1*] Beatriz Pês[2] Adolfo Bauchspiess[3] Marco Antonio Freitas do Egito Coelho[3]

1. Federal University of Technology of Paraná (UTFPR), Avenida Sete de Setembro 3165, 80230-901, Curitiba-PR, Brazil
2. Federal Institute of Paraná (IFPR), Rua Engenheiro Tourinho, 829, Campo Largo-PR, Brazil
3. University of Brasília (UnB), Campus Darcy Ribeiro, Asa Norte, Brasília-DF, Brazil

ARTICLE INFO

Article history
Received: 29 October 2019
Accepted: 11 November 2019
Published Online: 31 December 2019

Keywords:
NARX-OBF Models
Genetic Algorithm
Levenberg Marquardt
System identification

ABSTRACT

Nonlinear system identification concerns the determination of the model structure and its parameters. Although the designers often seek the best model for each system, it can be tricky to determine, at the same time, the best structure and the parameters which optimize the model performance. This paper proposes the use of a Genetic Algorithm, GA, and the Levenberg-Marquardt, LM, method to obtain the model parameters, as well as perform the order reduction of the model. In order to validate the proposed methodology, the identification of a magnetic levitator, operating in closed loop, was performed. The class NARX-OBF, Nonlinear Auto Regressive with eXogenous input-Orthonormal Basis Function, was used. The use of OBF functions aims to reduce the number of terms in NARX models. Once the model is found, the order reduction is performed using GA and LM, in a hybrid application, capable of determining the model parameters and reducing the original model order, simultaneously. The results show, considering the inherent trade-of between accuracy and computational effort, the proposed methodology provided an implementation with good mean square error, when compared with the full NARX-OBF model.

1. Introduction

A system can be defined as a structure in which different variables interact and produce observable signals. In the same way, a model expresses the relation between observable quantities. Therefore, allowing the prediction of properties and behavior of an object [1].

In control engineering, modeling systems is a constant need. The model can provide a better understanding of the system operation, it can also be a powerful prediction tool which may prevent faults in the real system [2].

System Identification can be regarded as the field responsible for relating a purely mathematical model to a system. That is, in the development of the model, only data concerning the system input and output are needed [3]. That approach is known as black box modeling and it is very appealing, since no simplifying assumptions are requested when building the model [4].

There are several classes of models that can be used in the development of a black box model. The designer must consider representation capability and computational ef-

**Corresponding Author:*
Elder Oroski,
Federal University of Technology of Paraná (UTFPR), Avenida Sete de Setembro 3165, 80230-901, Curitiba-PR, Brazil;
Email: oroski@utfpr.edu.br

 DOI: https://doi.org/10.30564/ssid.v1i2.1341

fort when choosing a class. That is not an easy choice and is often empirically made. As examples of classes of nonlinear models frequently mentioned in literature, one can cite Volterra Series [5] and NARX [6], Nonlinear Auto Regressive with eXogenous input. These classes may present a dimensionality problem, since the number of terms to be determined in the model is often high [3].

The dimensionality problem is less critical in NARX models, since past outputs are considered in the model, which reduces the number of terms required by the model. Additionally, it is possible to reduce the computational cost of NARX models even more, selecting the most relevant series' terms [7] (in other words, performing the order reduction of the model).

Order reduction techniques are specially interesting for the representation of highly nonlinear systems, since the number of terms in a polynomial model increases with the nonlinearity degree of the system [3]. NARX models are known for the high representation capability. In order to avoid the loss of this characteristic, the order reduction must be carefully parametrized [8].

It is worth mentioning that the use of OBF, Orthonormal Basis Functions, is widely known in literature. ARX-OBF [9], which are Infinite Impulse Response, IIR, models and Volterra-OBF [8,10,11], which are Finite Impulse Response, FIR, models have already been proposed. NARX-OBF models [11], which can be seen as a feedback version of the Volterra-OBF models, have also been treated in previous work.

It can be considered that a NARX-OBF model is a more compact implementation of the classical NARX models. That is, the use of OBF reduces the number of terms necessary to the model. In order to improve the performance of the NARX-OBF models, this paper proposes an order reduction methodology for this class of models.

A Genetic Algorithm, GA, is used to select the most representative terms of the full NARX-OBF model. Thus, simplifying the model realization and reducing the simulation time. The evaluation function applied in the GA is inspired by the Akaike Information Criterion [12], AIC. This criterion quantifies the impact in the Mean Square Error (MSE) caused by the insertion of a new term in the model. At the same time, the AIC penalizes the insertion of this new term, since it increases the model complexity.

With a fitness function which considers the AIC, the GA proposed in this work is capable of realize the joint minimization of the MSE and of the number of terms in the model. That is, the GA performs a multi-objective optimization, aiming the simplest model with the best representation.

It is important to mention that the use of GA in the order reduction of NARX polynomial models has already been investigated [13]. However, in this paper it is proposed the use of GA as a mechanism of search for the poles of the Kautz functions, in NARX-OBF models, and also to reduce the number of terms in the series that implement such a model. Furthermore, in the proposed methodology, the GA acts by interleaving its actions with the Levenberg-Marquardt method, which is the latter responsible for determining the coefficients of the NARX-OBF model.

The main contributions of this work can be defined as:

(1) the joint minimization of: (1) the MSE and; (2) the complexity of the NARX-OBF models, (i.e., the joint search for the model structure and its parameters);

(2) the interleaving application of the GA method (searching for Kautz poles and the model structure), and the Levenberg Marquardt method (which search for models' coefficients).

This paper is divided as follows: section 2 presents the structure of NARX-OBF models, section 3 gives a summarized description of the methods for parameter selection, section 4 presents the identification of the magnetic levitation system, section 5 presents the main results obtained and, finally, section 6 is dedicated to conclusions and future work.

2. NARX-OBF Models

This section is dedicated to present basic concepts regarding orthonormal functions and NARX-OBF models [11].

2.1 Orthonormal Basis Functions

The main property of orthonormal functions is expressed by Eq. (1).

$$\langle \psi_m(k), \psi_n(k) \rangle = \begin{cases} 0 & m \neq n, \\ 1 & m = n, \end{cases} \tag{1}$$

in which $k, m, n \in Z$, and $\varphi_m(k)$ and $\varphi_n(k)$ are orthonormal functions and $<\cdot>$ is an inner product, defined by Eq. (2).

$$\langle \psi_m(k), \psi_n(k) \rangle = \sum_{k=-\infty}^{\infty} \psi_m(k) \psi_n^*(k), \tag{2}$$

in which $\varphi_n(k)^*$ represents the complex conjugate of $\varphi_n(k)$. To be classified as orthonormal, a function must satisfy the following requirements:

$$\begin{aligned} &- \langle \psi_m, \psi_n \rangle = 0, \quad \text{for } m \neq n; \\ &- |\psi_n| = 1, \quad \forall\, n; \end{aligned}$$

DOI: https://doi.org/10.30564/ssid.v1i2.1341

in which $|\varphi_n(k)| = \sqrt{\langle \varphi_n(k), \varphi_n(k) \rangle}$.

As examples of orthonormal functions, one might mention Hermite, Jacobi, Laguerre, Legendre, Kautz and the Generalized Orthonormal Basis Functions, GOBF. In this work, Kautz functions are employed.

2.2 Kautz Functions

Kautz functions are orthonormal functions parametrized by complex poles [8,9]. Equations (3) and (4) present the general form of Kautz functions:

$$K_{2m}(z) = \frac{\sqrt{(1-\tau^2)(1-\sigma^2)}}{z^2+\sigma(\tau-1)z-\tau}\left[\frac{-\tau z^2+\sigma(\tau-1)z+1}{z^2+\sigma(\tau-1)z-\tau}\right]^{m-1}, \quad (3)$$

$$K_{2m-1}(z) = \frac{z(z-\sigma)\sqrt{1-\tau^2}}{z^2+\sigma(\tau-1)z-\tau}\left[\frac{-\tau z^2+\sigma(\tau-1)z+1}{z^2+\sigma(\tau-1)z-\tau}\right]^{m-1}, \quad (4)$$

in which $m \in N$, stands for the complex variable associated with the Z transform, $K_{2m}(z)$ and $K_{2m+1}(z)$ are the even and odd Kautz functions, respectively. Considering that β and $\overline{\beta}$ are the complex conjugate poles that parametrize these functions, and can be expressed by:

$$\sigma = (\beta + \overline{\beta})/(1 + \beta\overline{\beta}), \quad (5)$$

$$\tau = -\beta\overline{\beta}. \quad (6)$$

The use of orthonormal functions in nonlinear models aims to reduce the number of terms required by the Volterra or NARX models [8,10]. In this context, FIR models described by Kautz basis (as Volterra-OBF models) can be implemented by concatenated filters, as depicted in Figure 1.

The idea behind of NARX-OBF models came from the Volterra-OBF models. Thus, NARX-OBF can be seen as a feedback version of Volterra-OBF model [11]. Eq. (7) is the mathematical expression of a NARX-OBF model.

$$\hat{y}(k) = M_u(k) + M_y(k) + M_{uy}(k), \quad (7)$$

in which $M_u(k)$, $M_y(k)$ and $M_{uy}(k)$ stands for the input, output and hybrid model components, respectively. These components are expressed by equations (8), (9) and (10).

$$M_u = \sum_{m=1}^{n} c_m^u w_m^u + \sum_{p=1}^{n}\sum_{q=p}^{n} c_{p,q}^u w_p^u w_q^u, \quad (8)$$

$$M_y = \sum_{m=1}^{m} c_n^y w_m^y + \sum_{p=1}^{m}\sum_{q=p}^{m} c_{p,q}^y w_p^y w_q^y, \quad (9)$$

$$M_{uy} = \sum_{p=1}^{m}\sum_{q=1}^{n} c_{p,q}^{uy} w_q^u w_q^y, \quad (10)$$

in which the terms w_i^u are versions of the input, $u(k)$, filtered by a i-*th* order Kautz function, being i=1, 2,..., n. The terms w_j^y are versions of the output, $y(k)$ filtered by a j-*th* order Kautz function, being j=1, 2, ..., m. Further, c_i^u(for i=1, 2, ..., n), c_j^y j (for j=1, 2, ..., m) and c_{jl}^{uy} (for k=1, 2, ..., m, and l=1, 2, ..., n), are the coefficients of input, output and hybrid terms (nonlinear combination between the filtered input and output signals), respectively.

NARX-OBF models can also be expressed in the concatenated filters form, Figure 2 shows the idea. It is worth mentioning that, in this work, the NARX-OBF model is truncated in the 2nd order kernel. Once the model is defined, it is necessary to determine its parameters, in order to capture the system's dynamic whose one desire to model. In this scenario, next section is dedicated to detailing the parameter selection in NARX-OBF models.

3. Parameter Selection in NARX-OBF Models

As stated in section 1, the goal of this work is to determine the structure and parameters of an ARX-OBF model for a nonlinear system. To that end, a methodology which combines a Genetic Algorithm, GA, and the Levenberg-Marquardt, LM, method is proposed. The GA is used to find the model structure. It is worth pointing out that the GA searches for the terms that best represent the system dynamic. Thus, the algorithm finds a simplified structure for the model, aiming to reduce the computational effort.

The GA is also used in the search for the pole that parametrizes the orthonormal functions. Further, LM is the method used to find the coefficients of the model.

An appealing advantage of heuristic methods concerns stability. NARX-OBF models are feedback models and, therefore, might be unstable. Instability is a problem for conventional parameter determination methods, which may not be able to solve the estimation problem. Heuristic methods, however, are based on a population of solutions. These solutions are categorized regarding the fitness function. A solution resulting in an unstable model is poorly evaluated. Hence, the natural dynamic of the GA is able to neglect unstable models.

Next sections are dedicated to present the main ideas concerning GAs and LM method.

 DOI: https://doi.org/10.30564/ssid.v1i2.1341

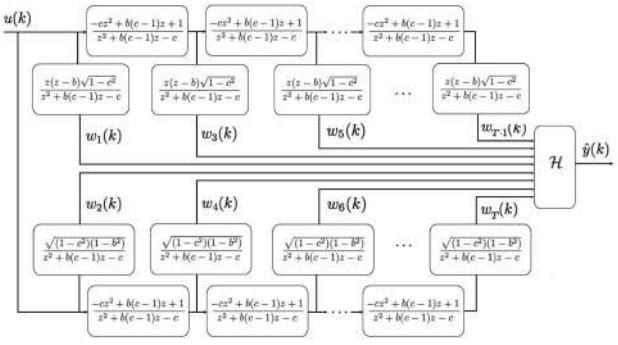

Figure 1. OBF model with Kautz dynamics [8]. $u(k)$ is the input and $\hat{y}(k)$ is the estimated output of the system to be identified [11]

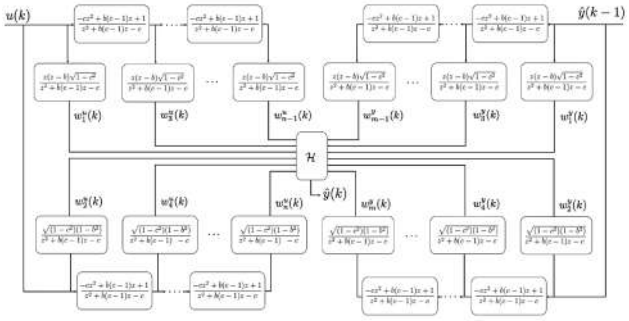

Figure 2. NARX-OBF model in the form of concatenated filters. Operations expressed by equations (8), (9) and (10) are represented by the H operator [11]

3.1 Genetic Algorithms

In the last decades, optimization problems have motivated great improvements in mathematics and engineering. Methods like Newton, steepest descendent and Levenberg-Marquardt have made possible the solution of a series of design optimization problems [14]. However, these methods require strong conditions to have their convergence proved, such as availability of gradients and convexity [15]. In several industrial applications the designer has to deal with some peculiarities such as nonlinearity, non-convexity, existence of several local minima, and presence of discrete and continuous design variables, among others [16].

Optimization methods that can potentially circumvent the problems mentioned above are the heuristic algorithms. Some advantages of these algorithms include: (i) these methods do not require gradient information and can be applied to problems in which the gradient is not defined; (ii) these algorithms are not "trapped" in local minima, if correctly tuned; (iii) these methods can be applied to discontinuous functions; (iv) these algorithms provide a set of sub-optimal solutions instead of a single solution.

Among the most popular heuristic algorithms are the Genetic Algorithms, GA [17], the Ant Colony Optimization, ACO [18], and the Particle Swarm Optimization, PSO [19], all inspired by biological principles.

Genetic Algorithm, GA, was developed by John Holland in the 1960s. Inspired by Darwin's evolutionary ideas, Holland has created a method in order to solve optimization problems that dispenses Jacobian or Hessian matrices of the problem [17]. The GA extracts an emergent behavior of convergence. Emerging behaviors involve the application of simple rules, over and over again, which generates complex behaviors [17].

In a GA, each individual is modeled as a set of constants [C_1, C_2, C_3..., C_n], called genes. These constants form a vector, C, known as a chromosome.

$$\mathfrak{C}: \boxed{c_1}\boxed{c_2}\boxed{c_3}\boxed{\ldots}\boxed{c_n}$$

such constants are real for the treated problem. GA have a whole population, P, of chromosomes:

$$\mathcal{P} = \{\mathfrak{C}_1, \mathfrak{C}_2, \mathfrak{C}_3, ..., \mathfrak{C}_m\}, \tag{11}$$

in which each chromosome is analyzed by an evaluation function, known as a fitness function, $Fit(C):R^n \rightarrow R$, and the chromosomes with the best fitness will have greater reproducing likelihood in the next GA generations.

Genetic Algorithm is a highly parallel mathematical algorithm which transforms a population of mathematical objects, with well-defined evaluation function, $Fit(C)$, in a new population of mathematical objects, following the Darwinian principles of reproduction of the most adapted.

According to Algorithm 1, a classical GA creates a random population of solutions, expressed by P. This population consists of possible solutions, C, to the problem addressed.

Algorithm 1: Genetic Algorithm

```
Initializes the population of solutions, P;
Simulates the model generated by each chromosome;
Fitness is calculated for each chromosome, F_it(C);
while F_it > Stop_criterion do
    The best individual is saved;
    Selecting parents;
    Apply Crossover Operator;
    Apply Mutation Operator;
    Simulate the model corresponding to each
      chromosome;
    Evaluate Fitness function for each chromosome;
```


DOI: https://doi.org/10.30564/ssid.v1i2.1341

The solutions are, then, evaluated by the function *Fit*(*C*). After these steps, the best individuals (chromosomes with the lowest image in the evaluation function,*Fit*) are (more likely) selected to be progenitors of the next generation.

The Crossover and Mutation operators are applied to the population and the generated individuals are evaluated. This cycle is repeated until the stop criterion is reached, i.e., the fitness value of the best chromosome is smaller than a certain threshold: $Fit(C) < Stop_{\text{criterion}}$.

It should be emphasized that GAs do not guarantee convergence to the optimum of the problem, and may end up confined to a local region [20]. A point x_1 is a local minimum if there is a neighborhood v (of x_1), such that $f(x_1) \leq f(x)$ for $x \in v$[14].

3.1.1 Crossover

The Crossover operator was inspired by the biochemical process of Crossing-Over, in which parts of two chromosomes are exchanged in the process of sexual reproduction [20]. Figure 3 shows the Crossover operator action under chromosomes $f=[f_1, f_2, f_3..., f_n]$, and $g=[g_1, g_2, g_3..., g_n]$. This operator performs the local search in the search space [17].

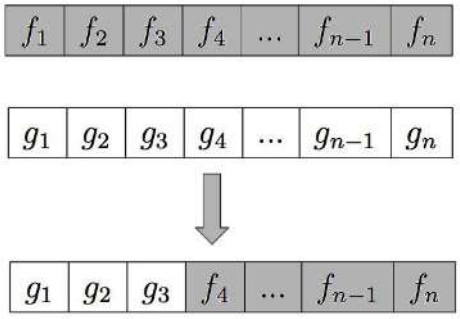

Figure 3. Example of Crossover operator

3.1.2 Mutation

The Mutation operator can perform an exploration (in the searching space) by inserting a random constant into a random gene position, as expressed in Figure 4.

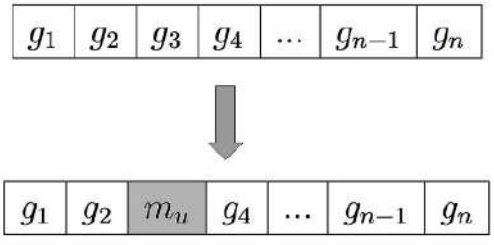

Figure 4. Example of Mutation operator

This operator has essentially the global search function, being complemented by the crossover operator, that performs local searches, composing the mechanism of a classical Genetic Algorithm.

3.2 Levenberg-Marquardt

The Levenberg-Marquardt method can be derived by substituting the exact line search strategy (see [15]), for the Confidence Regression strategy (see [14]). The use of the Confidence Regression strategy avoids the main problem of the Gauss Newton method, which occurs when the Jacobian, $J(x)$), stop being full rank, or near to it [14]. Generally, the Hessian of a generic function, $f(x)$, can be approximated as:

$$\nabla^2 f(x) \approx J_\xi(x)^T J_\xi(x), \tag{12}$$

In order to simplify (12), $\nabla^2 f(x)$ can be expressed by $B(x)$, as (13).

$$B(x) = J_\xi(x)^T J_\xi(x) \approx \nabla^2 f(x). \tag{13}$$

The idea of the LM method is to disturb the matrix $B(x)$, considering $B(x)+\rho I$, for > 0. This method can be understood as the Gauss-Newton method with the following modification:

$$\begin{cases} x_{k+1} = x_k + \Delta x_k \\ \Delta x_k = -[J_\xi(x)^T J_\xi(x) + \lambda I]^{-1} [J_\xi(x)^T \xi(x)], \end{cases} \tag{14}$$

in which $\lambda \in \mathbb{R}$ and I is the identity matrix.

It is reasonable to consider the use of hybrid algorithms. Such algorithms behave as LM, for small residues, and apply the Newton method, for larger residues [14]. As the Gauss-Newton methods, LM is based on an expansion into Taylor's series [21]. The search mechanism used by the Levenberg-Marquardt method can be observed in the algorithm 2.

Algorithm 2: Levenberg-Marquardt Algorithm.

Let be $x_0 \in \mathbb{R}^n$;
Calculate d_0, solution of:
$[B(x_0) + \lambda I]\, \Delta x_0 = -\nabla f(x_0)$;
in which: $B(x) = J_\xi(x)^T J_\xi(x)$;
$x_1 = x_0 + \Delta x_0$;
k=1;
while $\nabla f(x_k) \neq 0$ **do**
  Calculate Δx_k, solution of:
  $[B(x_k) + \lambda I]\, \Delta x_k = -\nabla f(x_k)$;
  Determine x_{k+1};
  $x_{k+1} = x_k + \Delta x_k$;
  k=k+1

 DOI: https://doi.org/10.30564/ssid.v1i2.1341

3.3 Proposed Methodology

NARX-OBF models, in their complete form, have a high number of terms [8,9], therefore, reducing the order of the model is interesting from a computational perspective.

In order to reduce the model order, the GA fitness function take two aspects under consideration: (i) the number of terms, N_C; and (ii) the minimization of the *MSE*. Eq. (15) expresses the fitness function used in this work, which was inspired by the Akaike criterion [12].

$$f_{it}(MSE, NC) = N \times MSE + 0.1\, N_C \times log(N), \quad (15)$$

in which N is the number of samples in the input and output signals of the system, *MSE* is the mean square error, N_C stands for the number of coefficients involved in the model and the multiplier 0.1 is an empirical coefficient, used to balance the weight of terms.

The genes used in the GA are depicted in Figure 5. The real and imaginary parts of the Kautz function pole and the presence of terms coefficients in the NARX-OBF model are genes in the GA chromosome. Thus, the evolutionary dynamics of the GA is responsible for selecting the terms of the model which are representative for the system to be identified, performing an order reduction of the NARX-OBF model.

$Real(\beta)$	$Imag(\beta)$		
p_1	p_2	$\cdots$	p_n

Figure 5. Structure of genes that compose a chromosome in the proposed GA. is the pole of the Kautz functions and the genes of the vector represent the presence or absence of each term of the NARX-OBF model, in its simplified version

Note: If, e.g., p1 is 0 the first term of the NARX-OBF model is disregarded. If p2 is 1, the second term of the series is maintained.

In the proposed methodology the idea is interleaving a heuristic algorithm, GA, and a deterministic one, LM algorithm. Mixing these two algorithms, one can achieve the advantages of heuristic algorithms (do not get stuck in local minima) and the advantages of deterministic algorithms (the guaranty of finding the global minimum in a concave region of the search space). In this context, GA is responsible for finding: (i) the orthonormal functions pole; and (ii) the NARX-OBF model structure, whereas the LM is responsible for finding the model coefficients. The loop interaction between the two algorithms is illustrated in Figure 6.

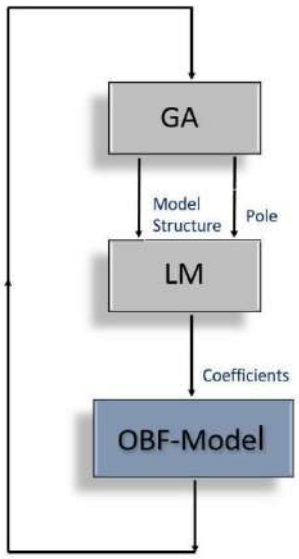

Figure 6. Search mechanism of OBF-model parameters

In order to testing this methodology, in the next section, it will be presented the identification process of a non-linear system.

4. Identification of a Magnetic Levitator

In order to validate the proposed method for reducing the order of a NARX-OBF model, a magnetic levitation system was chosen and identified. The system consists of 2 permanent magnets and a mobile magnetic disk. Four coils, operated two at a time, are able to control the disk movement. In this paper, the model is obtained concerning the x-axis. That is, the movements in the axes y and z are neglected [22]. A schematic of the system is depicted in Figure 7.

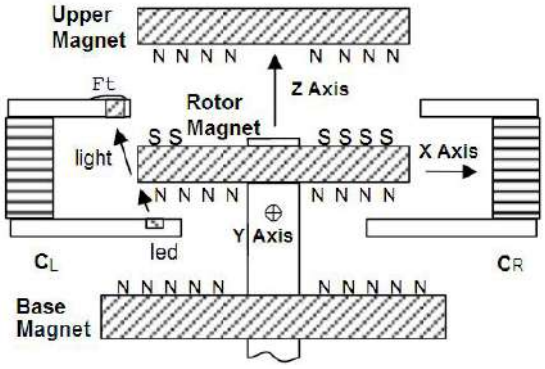

Figure 7. Magnetic levitator schematic, adapted from [22]

The identification of a nonlinear system, such as the one in Figure 7, starts by the application of a Persistently Exciting, PE, signal to its input. A signal is said to be per-

DOI: https://doi.org/10.30564/ssid.v1i2.1341

sistently exciting if, considering the need to estimate N_p parameters, it has spectral power in N_p bands of frequency [4].

A widely used kind of PE signal is the Pseudo-Random Multi Level Signal, PRMLS. The variable range of the signal amplitude is desirable in the identification of nonlinear systems, since it provide the excitation of the system several dynamics [3].

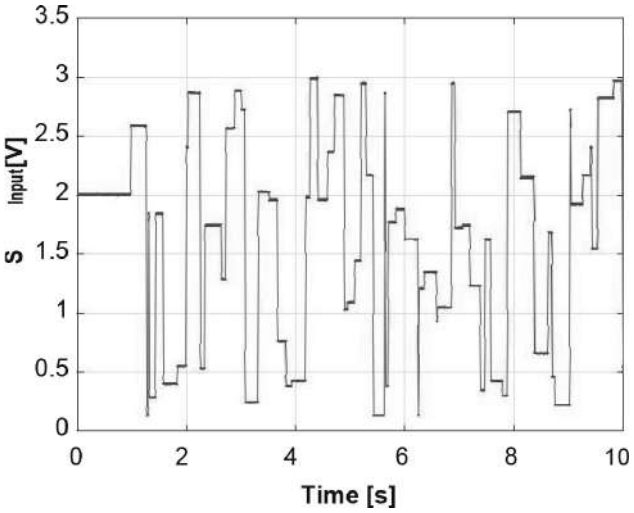

Figure 8. Input data sampled in the magnetic levitator

According to Earnshaw's theorem [23], the system in Figure 7 is unstable. Thus, in order to circumvent the instability problem, the system operates in closed loop under the action of a Proportional Integral, PI, controller.

Figure 9 depicts the system output response to the input signal (presented in Figure 8). Both signals, input and output, are composed by 100,000 samples. The sampling period is of 1 ms. Moreover, in the validation of the model, 20,000 samples were used.

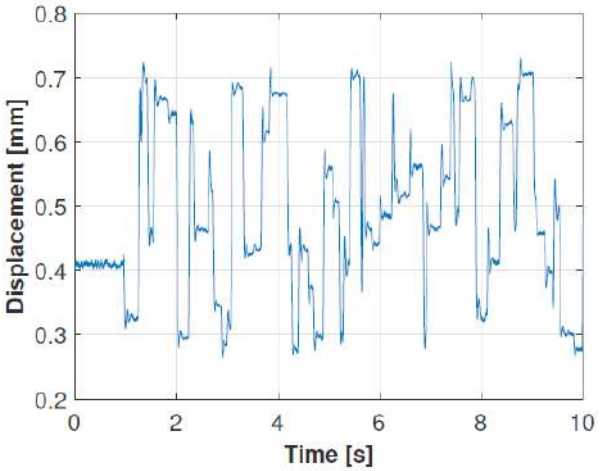

Figure 9. Output data sampled in the magnetic levitator

Table 1. Genetic Algorithm Parameters

Parameter	Value
Population	200 Chromosomes
Selection Method	Tournament
Mutation Rate	varies linearly (5 to 20 %)
Crossover Rate	varies linearly (80 to 40 %)

Table 1 shows the specifications of the GA, which performed the parameter search for the NARX-OBF model. It is worth to emphasize that the metric applied in the identification process aims the minimization of the *MSE* as well as the reduction of the model complexity, as expressed in Eq. (15).

Genetic algorithms have a stochastic component [17]. Thus, there is no guarantee that the *MSE* has reached its global minimum. However, if the GA is well tuned, it is possible to find reasonable parameters. Further, in this work, the algorithm applies the GA to search the model structure and the OBF pole, and applies Levenberg-Marquardt method to find the model coefficients, interweaving the methods. It is important to mention that the GA loop keeps going on until the stop criterion is reached, i.e., the *MSE* of the best solution reach a value smaller than Ɛ. The complete structure of this hybrid GA can be seen in Figure 10.

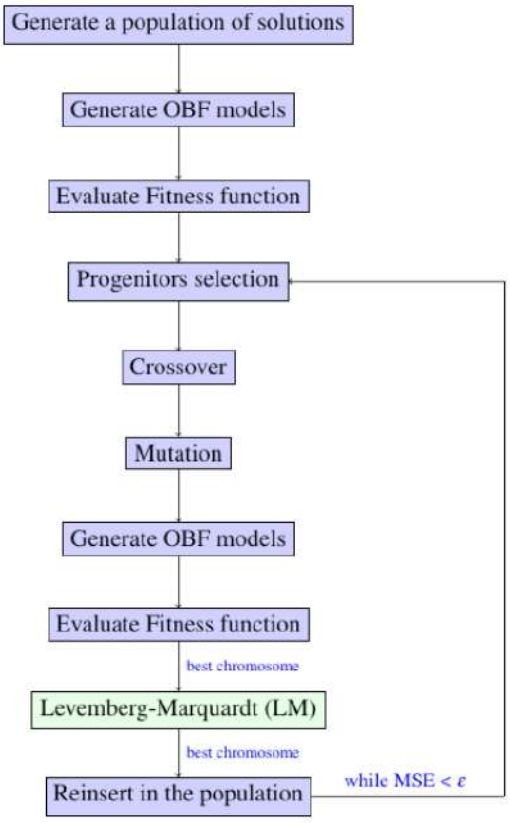

Figure 10. The proposed Genetic Algorithm structure

 DOI: https://doi.org/10.30564/ssid.v1i2.1341

expressed as a flowchart, $\mathfrak{E}$ is a higher limit for the MSE

Next section is dedicated to present the main results obtained in the identification of the magnetic levitator.

5. Results

After the closed-loop identification of the magnetic levitator, the *MSE* obtained in each complete NARX-OBF model, with different numbers of orthonormal functions, is shown in Table 2. In this table, N_F stands for the number of orthonormal functions used, and N_C corresponds to the number of coefficients for each NARX-OBF model. The larger N_C, the greater is the number of terms in the model. Therefore, models with larger N_C are more time consuming, computationally speaking.

Table 2. MSE for Complete NARX-OBF Models

N_F	N_c	Pole	MSE
2	14	0.6479 ± 0.3812i	1.9416×10^{-3}
4	44	0.5521 ± 0.4012i	9.7212×10^{-4}
6	90	0.6017 ± 0.0686i	5.4947×10^{-6}

The *MSE* for the NARX-OBF models with order reduction, and their fitness values, can be seen in Table 3.

Table 3. MSE for simplified NARX-OBF models

N_F	N_c	Pole	MSE	Fitness
2	8	0.3833 ± 0.7870i	1.8370×10^{-3}	40.1808
4	11	0.4770 ± 0.5850i	3.5540×10^{-3}	11.8331
6	54	0.5487 ± 0.0289i	3.5256×10^{-4}	30.2768

Figures 11, 12 and 13 illustrate the time responses of the reduced order NARX-OBF models cited in Table 3.

In order to make a visual comparison, Figure 14 depicts the performance of the complete NARX-OBF model, mentioned in Table 2.

Comparing tables 2 and 3 one can see that removing some terms of the complete NARX-OBF model does not represent a significant *MSE* increasing. Furthermore, analyzing the first row of tables 2 and 3, it is possible to see that removing 6 terms of the complete model leads to a small reduction in the *MSE*. This result shows that not all terms of the complete model are in accordance with the system dynamic. Therefore, removing these terms has small impact in the *MSE*. Thus, some results obtained by order reduction of NARX-OBF models can approximate complete NARX-OBF models without loss of generality.

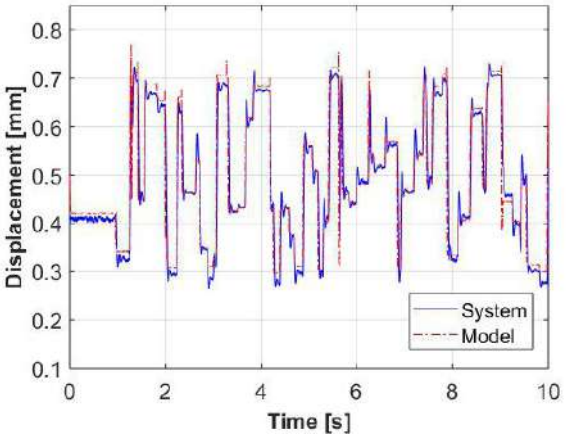

Figure 11. Identification results for the magnetic levitator, with reduced order NARX-OBF, using 2 Kautz functions and 8 coefficients (terms)

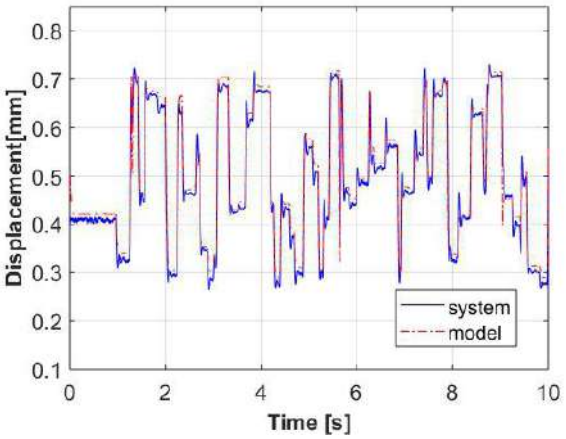

Figure 12. Identification results for the magnetic levitator, with reduced order NARX-OBF, using 4 Kautz functions and 11 coefficients (terms)

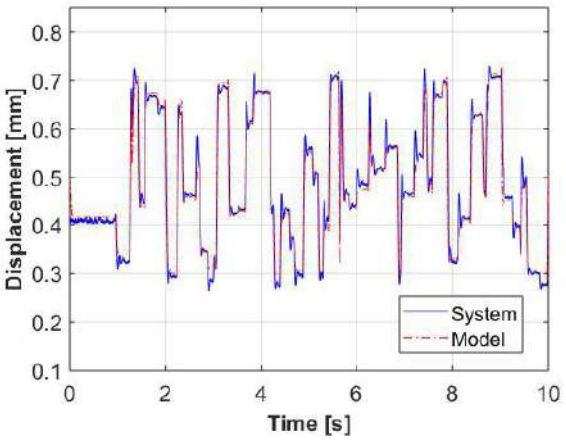

Figure 13. Identification results for the magnetic levitator, with reduced order NARX-OBF, using 6 Kautz functions and 54 coefficients (terms)

DOI: https://doi.org/10.30564/ssid.v1i2.1341

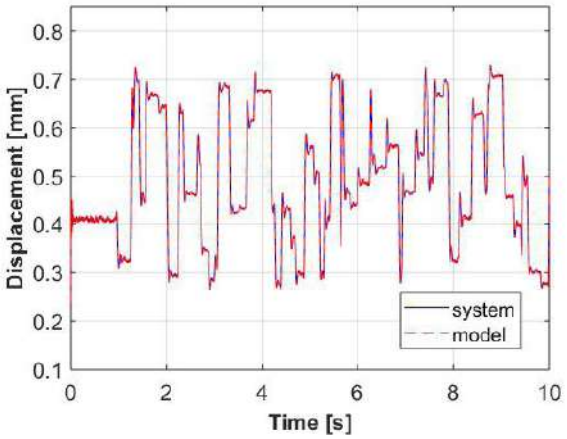

Figure 14. Identification results for the magnetic levitator, with complete NARX-OBF, using 6 Kautz functions and 90 coefficients (terms)

The time that each simplified model, expressed in Table 3, took to be simulated is shown in Table 4. The simulation time was computed for 10 simulations of each model, the average of the simulation time is expressed in the final row of Table 4. In this table, K indicates the number of Kautz functions and C, the number of coefficients. Thus, the model 2K 8C stands for the model with 2 Kautz functions and 8 coefficients, which is in the first row of Table 3.

Next section presents the main conclusions of this work.

Table 4. Simulation time for simplified NARX-OBF models

Time	2K 8C [s]	4K 11C [s]	6K 54C [s]
1	0.1124	0.2796	0.3806
2	0.1039	0.2535	0.3599
3	0.1057	0.2300	0.3521
4	0.1284	0.3708	0.4583
5	0.0905	0.2021	0.3107
6	0.0885	0.1995	0.3089
7	0.8889	0.2032	0.3075
8	0.0903	0.2008	0.3040
9	0.0892	0.1949	0.3074
10	0.0888	0.2027	0.3059
Average Time	0.0906	0.2032	0.3107

6. Conclusion

This paper proposes a method to obtain the order reduction of a NARX-OBF model. A Genetic Algorithm combined with the Levenberg-Marquardt method is used to find the model structure and parameters. The validation of the proposed methodology was based on the closed-loop identification of a magnetic levitator.

The results shown in tables 2 and 3 allow the conclusion that the order reduction is not only possible, but has little impact in the *MSE* value. Thus, one might say that some of the terms which compose the complete NARX-OBF model can be suppressed without lost the capacity of representing the system behavior. Moreover, in Table 3 it is possible to observe that the best fitness value is found in the intermediate situation, between the minimum *MSE* and the minimum number of terms, N_C. This case portrays the optimization of both criteria at the same time.

It is important to mention that GA is a probabilistic method and there is no guarantee in achieving the best *MSE* in the identification process. However, in average, it is possible to find reasonable parameters, as shown in tables 2 and 3.

The next steps of this work include the use of Genetic Programming to select the candidates to compose the simplified NARX-OBF model and the use of GOBFs (Generalized Orthonormal Basic Functions) instead of only Kautz functions.

Acknowledgment

The authors gratefully acknowledge the support provided by UTFPR and UnB.

References

[1] L. Ljung. System Identification - Theory for the user, Prentice Hall - PTR, 1999.

[2] K. J. Aström, T. Hägglund. Advanced PID Control, ISA, 2011.

[3] S. A. Billings. Nonlinear System Identification: NAR-MAX Methods in the Time, Frequency and Spatio-Temporal Domains, John Wiley & Sons, 1st. ed., 2013.

[4] R. Isermann, M. Munchhof. Identification of Dynamic Systems: An Introduction with Applications. Springer-Verlag Berlin Heidelberg, 2011.

[5] S. Silva. Nonlinear Mechanical System Identification using Discrete-Time Volterra Models and Kautz Filter, 9th. Brazilian Conference on Dynamics, Control and their Ap-plications, 2010.

[6] A. Rahrooh, S. Shepard. Identification of Nonlinear Systems using NARMAX Models, Elsevier - Nonlinear Analisis, n. 71, pp. 1198-1202, 2009.

[7] O. Akanyeti, I. Rañó, U. Nehmzow, S. A. Billings. An application of Lyapunov stability analysis to improve the performance of NARMAX models, Robotics and Autonomous Systems, 2009, 58: 229-238.

[8] P. S. C. Heuberger, P. M. J. Van der Hof, B. Wahl-

 DOI: https://doi.org/10.30564/ssid.v1i2.1341

berg. Modelling and Identification with Rational Orthogonal Basis Functions. Springer Press, 1st. Edition, 2005.

[9] D. T. Lemma, M. Ramasamy, M. Shuhaimi. Closed-loop Identification of Systems with uncertain Time De-lays using ARX-OBF structure, Journal of Process Control, 2011, 21(8): 1148-1154.

[10] A. da Rosa, R. J. G. Campello, W. C. Amaral. Exact Search Directions for Optimizations of Linear and Non-linear Models based on Generalized Orthonormal Functions, IEEE Trans. on Automatic Control, 2009, 54(12): 2757-2772.

[11] E. Oroski, A. Bauchspiess, R. H. Lopes. Identification of a Magnetic Levitator using NARX-OBF Models and Genetic Algorithm, International Journal of Modeling, Identification and Control, 2017, 28(4): 307-317.

[12] H. Akaike. A new Look at the Statistical Model Identification, IEEE Trans. on Automatic Control, 1974, 19(6): 716-723.

[13] C. M. Fonseca, E. M. Mendes, P. J. Fleming, S. A. Billings. Nonlinear Model Term selection with Genetic Algorithms, IEEE Workshop on Natural Algorithms in Signal Processing, 1974, 2(27): 1-8.

[14] J. Nocedal, S. Wright. Numerical Optimization, Springer, 1999.

[15] S. Boyd, L. Vandenberghe. Convex Optimization, Cambridge Press, 2009.

[16] J. Mockus, W. Eddy, G. Reklaitis. Bayesian Heuristic Approach to Discrete and Global Optimization: Algorithms, Visualization, Software and Applications, Kluwer Academic Publishers, 1st ed., 1997.

[17] J. Koza. Genetic Programming: On the Programming of Computers by Means of Natural Selection, MIT Press, 6th ed, 1998.

[18] C. Solnon. Ant Colony Optimization and Constraint Programing, Wiley Press, 1st ed., 2010.

[19] A. E. Olssom. Particle Swarm: Theory, Techniques and Applications, New Science Publishers, 1st ed., 2011.

[20] A. D. Coley. An Introduction to Genetic Algorithms for Scientists and Engineers, Would Scientific, 1999.

[21] D. W. Marquardt. An Algorithm for Least Squares Estimation of Nonlinear Parameters, Journal of Society for Industrial and Applied Mathematics, 1963, 11(2): 431-441.

[22] M. A. E. Coelho. Permanent Magnet based Magnetic Levitation Kit, International Journal of Applied Electromagnetics and Mechanics, 2015, 47: 963-973.

[23] L. Tonks. Note on Earnshaw's Theorem, Electrical Engineering, 1940, 59(3): 118-119.

DOI: https://doi.org/10.30564/ssid.v1i2.1341

BILINGUAL PUBLISHING CO.
Pioneer of Global Academics Since 1984

Semiconductor Science and Information Devices
https://ojs.bilpublishing.com/index.php/ssid

ARTICLE

A Novel Process for SiGe Core-Shell JAM Transistors Fabrication and Thermal Annealing Effect on Its Electrical Performance

Ashish Kumar Wen-Hsi Lee*

Department of Electrical Engineering, National Cheng Kung University, Taiwan

ARTICLE INFO

Article history
Received: 10 November 2019
Accepted: 19 November 2019
Published Online: 31 December 2019

Keywords:
Junctionless-accumulation (JAM) FET
Junctionless (JL) FET
SiGe core-shell
Rapid thermal anneal Subthreshold swing (SS)

ABSTRACT

In this study, we fabricate Si/SiGe core-shell Junctionless accumulation mode (JAM)FinFET devices through a rapid and novel process with four main steps, i.e. e-beam lithography definition, sputter deposition, alloy combination annealing, and chemical solution etching. The height of Si core is 30 nm and the thickness of Si/SiGe core-shell is about 2 nm. After finishing the fabrication of devices, we widely studied the electrical characteristics of poly Si/SiGe core-shell JAM FinFET transistors from a view of different Lg and Wch. A poly-Si/SiGe core -shell JAMFETs was successfully demonstrated and it also exhibits a superior subthreshold swing of 81mV/dec and high on/off ratio > 10^5 when annealing for 1hr at 600°C. The thermal diffusion process condition for this study are 1hr at 600°C and 6hr at 700°C for comparison. The annealing condition at 700oC for 6 hours shows undesired electrical characteristics against the other. Results suggests that from over thermal budget causes a plenty of Ge to precipitate against to form SiGe thin film. Annealing JAMFETs at low temperature shows outstanding Subthreshold swing and better swing condition when compared to its counterpart i.e. at higher temperature. This new process can still fabricate a comparable performance to classical planar FinFET in driving current.

1. Introduction

Complementary metal-oxide-semiconductor (CMOS) device have been the dominant device for ultra large -scale integration (ULSI) in semiconductor industry for decades due to its high speed and low power consumption. In recent years, owing to the limitation in miniaturization of VLSIs, we are looking for a novel material introduction to replace the planar Si channel devices in order to achieve high performance. Alternate channel materials such as Ge and SiGe are in great interest due to their higher mobility than Si. Moreover, stereoscopic channel structure are the primary methods to advance performance.

Si/SiGe core-shell hetero-structures are recognized as the most promising solutions to further continue the Moore's law beyond conventional planar bulk technologies are in great interest for p-type high-performance MOSFET. Core/shell structures with either Si or Ge as the core or shell have been researched such as Ge/Si [1], SiGe/Si [2], or Si/Ge [3] core/shell NW hetero-structures have been proposed to improve the hole transport in p-type FETs. Compared to traditional 2D Si planar devices, core-shell hetero-structure devices offer higher drive current

**Corresponding Author:*
Wen-Hsi Lee,
Department of Electrical Engineering, National Cheng Kung University, No.1, University Road, Tainan City 701, Taiwan (R.O.C.);
Email: leewen@mail.ncku.edu.tw

 DOI: https://doi.org/10.30564/ssid.v1i2.1399

and strong gate controllability due to its geometrical advantage. A core-shell MOSFET fabrication approach passes through two-step process. First, grow core structure through bottom-up [2-4] or top-down [1,5] methods. Second, the shell structure around the core is grown by chemical vapor deposition (CVD). However, there exist a challenge in this method that hetero-epitaxy is very difficult in the case of horizontal layers [6].

In this study, we fabricate core-shell devices through a rapid and novel process with four steps, i.e. e-beam lithography definition, sputter deposition, alloy combination annealing, and chemical solution etching. Different from above methods, we introduce a whole low cost and low thermal budget methods for core-shell structure fabrication a new choice.with the miniaturization of the channel length, the diffusion problem of short-channel junction doping occurs and it is difficult to accurately control the abrupt junctions [7]. Thus, the junctionless (JL) FETs have been proposed to solve the problem in the fabrication of ultra-shallow and abrupt junctions profile [8-10]. Different from inversion-mode (IM) FETs, because channel and S/D of junctionless (JL) FETs have the same heavily doping concentration and doping types, there is no PN junctions exists between channel and S/D. Furthermore, (JL) FETs have different conduction mechanism compared to the inversion-mode (IM) FETs.

Figure 1 shows the cross-sectional structures of p-type FETs along the S/D direction showing the doping profile, including (a) inversion mode (IM) FETs, (b) junctionless (JL) FETs [9,10]. Owing to thermal diffusion of S/D dopants into the channel, (IM) FETs has a shorter effective channel length than the physical channel length. For the (JL) FETs, because the work function difference between the gate electrode and the channel pushes away the depletion region from gate edge to the S/D, it has a longer effective channel length than the physical channel length [11]. Hence, (JL) FETs are regarded as having stronger immunity against short-channel effects than (IM) FETs [12-14].Because of the large number of carriers, there is a big challenge in the (JL) FETs process that carriers in the channel are difficultly fully depleted. For this reason, the channel dimension of (JL) FETs must be a small cross-sectional area. However, (JL) FETs have a critical issue which is high S/D parasitic resistance due to the small channel dimension and random dopant fluctuation (RDF) [15]. To overcome these problems, junctionless accumulation mode (JAM) FETs have been proposed. Junctionless accumulation mode (JAM) FET with additional S/D implantation have been implemented for lowering the S/D parasitic resistance [9,16,17], as shown in Figure 2. Different from conduction mechanism of (JL) FETs, when devices turn on, (JAM) FETs have an accumulation layer at the channels surface [9].

In this study, we proposed a (JAM) FETs but without channel doping, the SiGe channel is intrinsic. And we depend S/D implantation with B^{11+} to demonstrate a p-type junctionless accumulation mode FETs. After introducing several concepts above, we can briefly clarify the target to effectively achieve novel way of process for fabricating SiGe Core-Shell transistors.

2. Experimental Procedure

In this study, we demonstrate a Si core cladded with a SiGe shell JAMFET, there are several methods to fabricate Si core / SiGe shell structure, such as SiGe condensation [6,18] or directly epitaxy SiGe layer on the Si fins [19]. Here, we choose DC sputter to deposit Ge on the Si fins. The reason why we choose sputter deposition to fabricate core-shell is that sputtering has advantages such as high purity and vacuum, furthermore, it can form a thin film in low temperature.

Main process flow is shown in Figure 3. Device fabrication begins on a 6-inch Si wafer grown with 200 nm wet oxide, after that, a 50-nm-thick Si_3N_4 layer is deposited on it. Then the 40-nm-thick undoped amorphous Si (α-Si) layer is deposited via low-pressure chemical vapor deposition (LPCVD), then α-Si is transformed to poly-Si through solid-phase crystallization (SPC) for 24 hrs at 600°C in N_2 ambient.

The active region is defined by E-beam stepper and reactive-ion etching (RIE) to form a poly-Si fin-channel. Then, 12-nm-thick amorphous Ge (α-Ge) layer is deposited by sputter and 20-nm-thick $PESiO_2$ is deposited on amorphous Ge layer to prevent Ge from oxidation during the thermal process. The combination of amorphous Ge between poly-Si is via the horizontal furnace tube in different annealing temperature and time i.e. 1 hr at 600°C and 6 hr at 700°C to form the different Ge content in SiGe channel. However, the Ge completely covers whole wafer during sputtering. Because the etching selective ratio between SiGe and Ge is different, we depend on wet etching method to remove the residual Ge on the Si_3N_4 layer. We choose the etching solution from a few papers[20,21] and the suitable choice is $(HCl+H_2O_2)$: H_2O 0.5% at the room temperature. As mentioned in process flow, the poly-Si core/poly-SiGe shell structure channel is fabricated. Next, the gate oxide of 7-nm-thick Al_2O_3 is deposited by ALD and the TiN is deposited immediately as gate metal. After the gate patterning, B^{11+} implantation (1×10^{15} cm^{-2} at 10 keV) was carried out to form p-type S/D and the dopant activation is done through microwave annealing and the schematic configurations of key process steps for the po-

DOI: https://doi.org/10.30564/ssid.v1i2.1399

ly-Si / SiGe core-shell JAMFETs are shown in Figure 4. Finally, material and electrical performance of poly-Si/ SiGe JAMFET were analyzed and discussed for two thermal annealing condition i.e. 1 hr at 600°C and 6 hr at 700°C.

3. Results and discussion

Figure 5 shows the depth profile of active region after the SiGe combination annealing by the X-ray photoelectron spectroscopy. As shown in Figure 5, the SiGe shell composition can be observed, the content of Ge at the channel surface are 20.8%,36.4% and 32.9% for different annealing condition (1hr at 600°C,1hr at 700°C and 6hrs at 700°C), respectively. In addition, no matter which annealing condition is, the profile of Ge has higher content at the surface forming a SiGe alloy. When etching depth reaches a deeper position, the Ge content decrease obviously about below 5%. In this paper, we will mainly perform observe electrical performance at annealing condition for 1hr at 600°C and 6hrs at 700°C It is noteworthy that when the annealing temperature is 700°C, more Ge penetrating into the Si layer than annealing temperature is 600°C. Hence, the Ge penetration is severe for higher annealing temperature. Finally, SiGe is detected on the shell of this structure through energy dispersive spectrometer (EDS). From Figure 6 we can demonstrate that the element content on the shell of silicon and germanium is 85.35% and 14.65%.

In this part, we investigate the material analysis results and electrical parameters of poly-Si /SiGe core-shell JAMFETs with different SiGe combination annealing conditions. The measured dimensions of channel width (W_{ch}) are 40 nm,60 nm,80 nm and 100 nm and gate length (L_g) are 60 nm,80 nm,100 nm,120 nm,150 nm,200 nm and 400 nm. Figure 7 shows the cross-sectional transmission electron microscope (TEM) image of poly-Si/SiGe core-shell JAMFET. In Figure 7, a rectangular shape core-shell structure is successfully fabricated in which channel width (W_{ch}) × channel height (H_{ch}) is (68 × 30)nm and effective width (W_{eff}) is 128 nm. We observe that the white region is a 2.17 nm-thick thin SiGe layer cladding on a 30 nm-thick poly Si layer after chemical solution etching and a 5.16 nm-thick Al_2O_3 layer and a 63.25 nm-thick TiN surround the core-shell channel.

We expect that the specific condition of annealing can combine Ge and Si at the channel surface but rarely penetrates Ge into Si. There are mainly two SiGe combination annealing condition i.e. 1hr at 600° and 6hrs at 700°C in N_2 ambient. The sample structure is poly $Si_{1-x}Ge_x$ (x = 20% ~ 37%) / poly Si / wet SiO_2 / substrate. Furthermore, we investigate the electrical characteristics such as I_D versus V_G, threshold voltage, subthreshold swing, DIBL and on current of the condition of Poly-Si /SiGe core-shell JAMFETs when SiGe combination annealing condition is 1hr at 600°C and 6hrs at 700°C with different dimension. The electrical performance of poly-Si/SiGe core- shell JAMFETs were measured at room temperature by semiconductor device analyzer (KEITHLEY, version V9.1 SP3). Figure 8 shows the outstanding transfer characteristics of poly-Si/SiGe core -shell JAMFET with channel width =40nm and gate length of 100nm for different annealing activation time. i.e. for 1hr at 600°C and 6hr at 700°C, respectively. The p-type Poly-Si / SiGe core-shell devices for 1hr annealing at 600°C perform a superior S.S. in comparison to the annealing for longer duration of annealing at 700°C and the resulting value is 81 mV/dec and 101 mV/dec, respectively and I_{ON}/I_{OFF} ratio is > 10^5. It indicates that there is improvement in sub-threshold swing when annealing for less annealing duration and temperature. Subthreshold swing was relatively higher in case of high annealing condition of Si/SiGe core shell JAMFET device. This may be due to the relatively higher interface trap density in SiGe channel when annealing at high temperature. Figure 9 displays the on-state current for p-type Poly-Si / SiGe core-shell JAMFETs as function of different channel width and fixed gate length=100nm, where gate voltage(Vg) was varied from 0 to -2.4V with a step of -0.6V. The resulting drain current is higher in case of annealing for 6hr at 700°C when compared to its counterpart i.e. annealing for 1hr at 600°C. In an ideal MOSFET, I_d is expected to be linearly dependent on V_{gs}, as shown by equation (1).

$$I_d = C_{ox}\mu\frac{W}{L}\left[\left(V_{gs}-V_t\right)V_{ds}-\frac{V_{ds}^2}{2}\right] \quad (1)$$

Where, I_d= Drain current, C_{ox}= Oxide capacitance.

To extract V_t, an often-used method is the transconductance method, where the improved transconductance g_m is given by:

$$gm = \frac{W}{L}\frac{2a}{q}C_{OX}^2\left(V_{gs}-V_t\right)V_{ds} \quad (2)$$

Where; α= common base current gain, q=magnitude of electron charge.

Figure 10 and Figure 11 shows I_D vs V_G characteristics of the poly-Si / SiGe core-shell JAMFET at various fin width and fixed gate length of 100nm for 1hr at 600°C and 6hr at 700°C. The figure shows that there is no strong dependence between on current as the channel

 DOI: https://doi.org/10.30564/ssid.v1i2.1399

width varies and the gate length except for that the minimum device of W_f= 60 nm demonstrating lower on current. By comparing the two figures, we know that the V_t roll-off phenomenon due to short channel effect is much more severe on the device for longer duration of thermal annealing condition. Furthermore, the sub-threshold properties and on-off current ratio are also degraded when the channel width increases. Figure 12 shows the distribution of subthreshold swing (SS) as function of gate length of 100nm and various channel width for 1hr at 600°C and 6hr at 700°C, respectively. It reveals that as the channel width increases from 40nm to 100nm ,the subthreshold swing also increases somewhat linearly. The minimum subthreshold swing was observed at channel width of 40nm for 1hr at 600°C and the maximum swing was observed at channel width of 100nm for 6hr at 700°C,indicating the degradation of gate controllability. Subthreshold swing remains almost constant and low in the annealing condition of 1hr at 600°C for channel width of 40nm and 60nm. In contrast, the electrical performance of neutral beam etched devices is similar within the gate length region of 150 ~ 400 nm, indicating better control of the interface properties. Figure 13 shows the dependence of threshold voltage a function of different gate length at a fixed fin width=60nm under two different annealing condition for poly-Si/SiGe core-shell JAMFETs. Figure 13(a) shows the short channel effect in terms of decreasing threshold value as it is annealed at low annealing duration for 600°Cfrom and the highest threshold voltage is about 0.299V at W_{ch} x L_g of 60 nm x 120 nm and the lowest threshold voltage is about -1.72V at W_{ch} x L_g of 60 nm x 200 nm.

From Figure 13(b), We observe that the rough trend of threshold voltage is decrease with gate length becoming long shows the short channel effects. The highest threshold voltage is about 1.53V at W_{ch} x L_g of 60 nm x 80 nm and the lowest threshold voltage is about -2.95V at W_{ch} x L_g of 60 nm x 400 nm. It is noticeable that the increase in gate length of channel material results in decrease on V_{th} of JAMFETs. Figure 14 shows the dependency of ON current on gate length of poly-Si/SiGe core-shell JAMFET at channel width of 40nm for 1hr at 600°C and 60nm for 6hr at 700°C, respectively. With the decrease in fin width, generally a slight increase in threshold voltage and a decrease in on current can be observed. In a thinner body, there are fewer amounts of inversion charge, and this is observed as a decrease in sub-threshold current and an increase in threshold voltage. With regards to the decrease in on current, it is directly related to the decrease in channel width, as can be referred in equation 1.For higher annealing temperature and longer duration ,On current slightly decreases with increase in gate length and the similar phenomena is observed for lower annealing temperature. From Figure 15 we can recognize that Ge is precipitated due to over thermal budget treatment in 6hrs 700°C annealing process. Our poly-Si/SiGe core-shell JAMFETS have shown quite good channel width scalability at low temperature thermal annealing when compared to longer annealing criterion. We realized a Si core cladded with a SiGe shell MOSFET which is fabricated with DC sputter to deposit Ge on the Si fins and through the horizontal furnace annealing in N_2 ambient and chemical etching process to remove residual Ge. In this study, driving current of silicon germanium for these devices is boosted. Although the V_{TH} displays there are still have SCE in these devices.

4. Conclusions

In this study we have demonstrated a Poly-Si /SiGe core-shell structure and investigated the electrical characteristics of Poly-Si /SiGe core-shell JAMFETs. The experimental results can be confirmed in the cross-sectional transmission electron microscope (TEM) image and energy dispersive spectrometer (EDS). A Poly-Si / SiGe core-shell gate stack is displayed in cross-sectional transmission electron microscope (TEM) image. There is a very thin SiGe layer cladding the Si fin forming a Si/ SiGe core-shell structure. The results of this study provide demonstration of novel technologies as well as physical insight into their performance. Studying in the terms of the electrical performance of Ion and S.S., we can observe that SiGe combination in the condition of 1hr 600°C precisely transfer and effectively enhance the electrical characteristics. The JAMFETs with channel width of 40nm and gate length of 100nm for 1hr at 600°C demonstrates the outstanding subthreshold swing of 81mV/dec and on/ off ratio $>10^5$. Compare to above results, the Ion of SiGe combination in the condition of 6hrs 700°C doesn't show the behavior which SiGe can strengthen the drive current. Also, the value of SS of SiGe combination in the condition of 6hrs 700°C is higher than previous conditions. Furthermore, we introduced a whole low cost and low thermal budget methods for core-shell structure fabrication as a new option.

Acknowledgements

The author would like to thank National Cheng Kung University, Tainan, Taiwan, for the financial support and also gratefully acknowledge Yi Jin for some part of experiments and prfsr. Wen Hsi Lee for his technical contribution to this work.

DOI: https://doi.org/10.30564/ssid.v1i2.1399

Appendixes

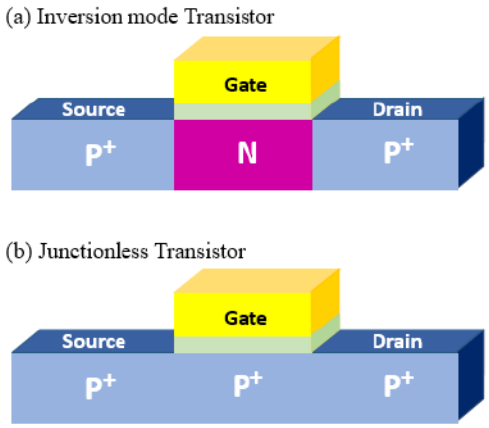

Figure 1. Cross-sectional structures of p-type FETs along the S/D direction (a) inversion mode (IM) FETs, (b) junctionless (JL) FETs

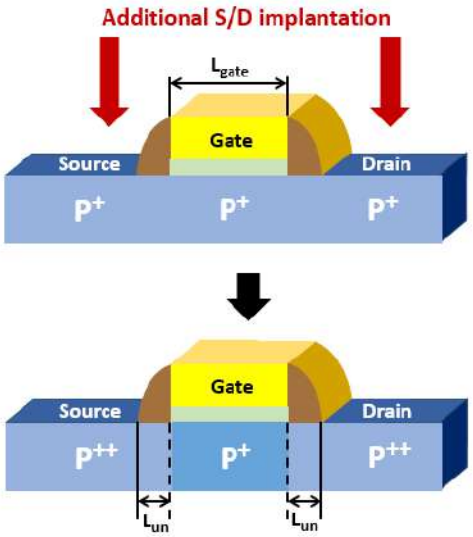

Figure 2. Junctionless (JAM) FET with additional S/D implantation

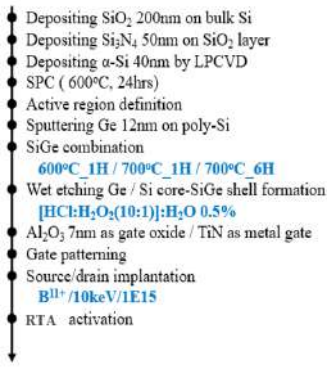

Figure 3. Process flow of the poly-Si / SiGe core-shell JAMFETs

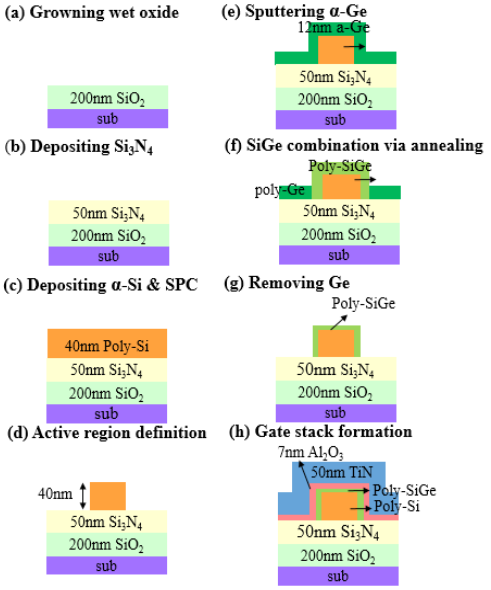

Figure 4. Schematic configurations of key process steps for the poly-Si / SiGe core-shell JAMFETs

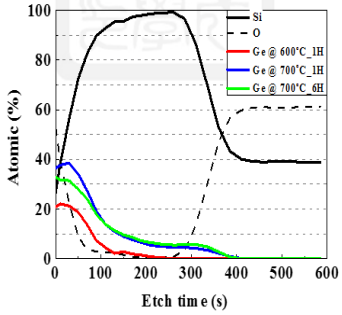

Figure 5. The depth profile of active region with three SiGe combination annealing condition,i.e.600°C_1hr,700°C_1hr,700°C_6hr

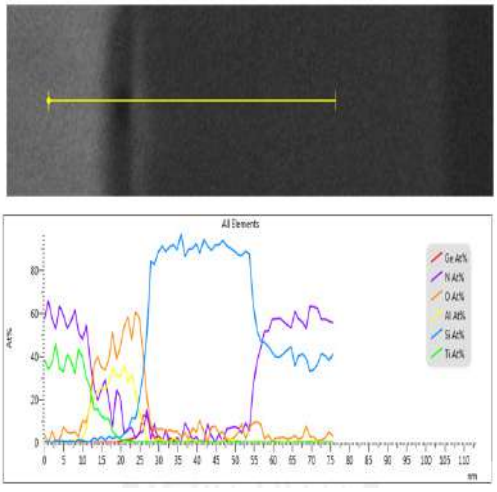

Figure 6. The element content distribution of poly-Si / SiGe core-shell JAMFETs by energy dispersive spectrometer

 DOI: https://doi.org/10.30564/ssid.v1i2.1399

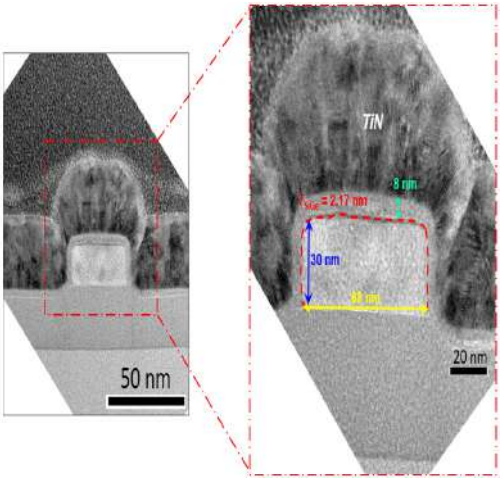

Figure 7. Cross-sectional TEM image of poly-Si / SiGe core-shell JAMFETs along the gate (b) The enlarged TEM image with H_{ch} = 30 nm, W_{ch} = 68 nm

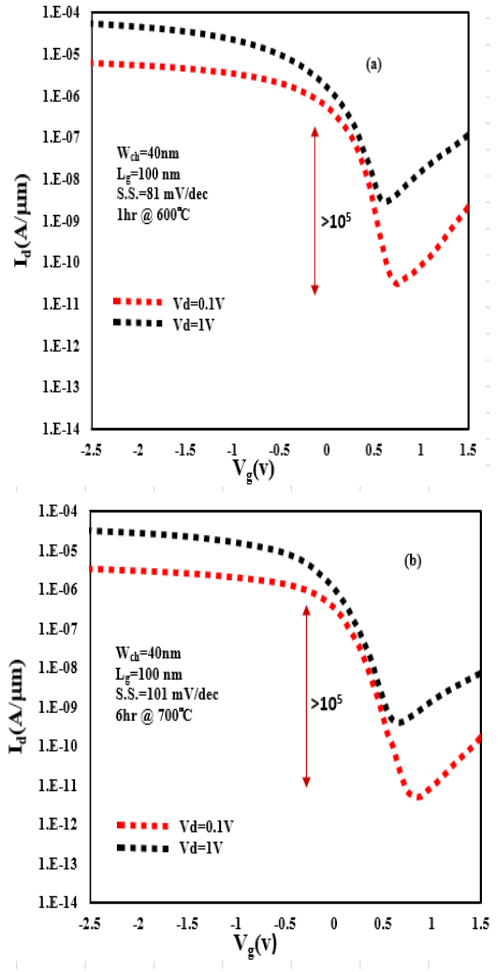

Figure 8. The outstanding transfer characteristics of the poly-Si / SiGe core-shell JAMFET at (a)Wch of 40 nm and Lg of 100 nm for 1hr at 600°C (b) Wch of 40 nm and Lg of 100 nm for 6hr at 700°C, respectively

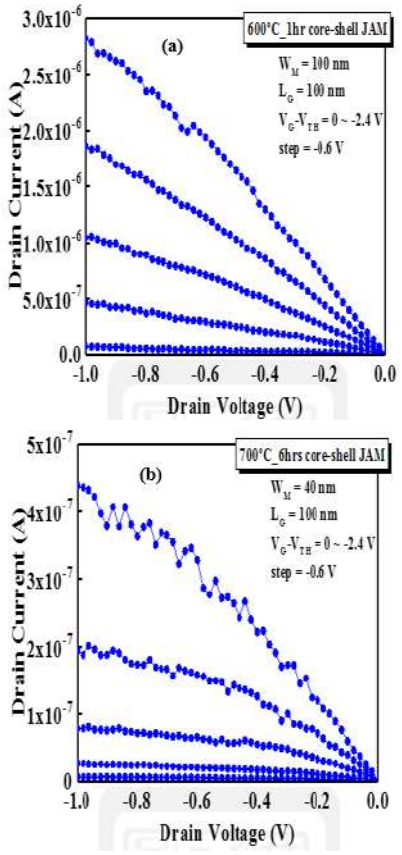

Figure 9. The outstanding I_D-V_D of the poly-Si / SiGe core-shell JAMFET at (a)W_{ch} of 100 nm and L_g of 100 nm for 1hr at 600°C (b) W_{ch} of 40 nm and L_g of 100 nm for 6hr at 700°C, respectively

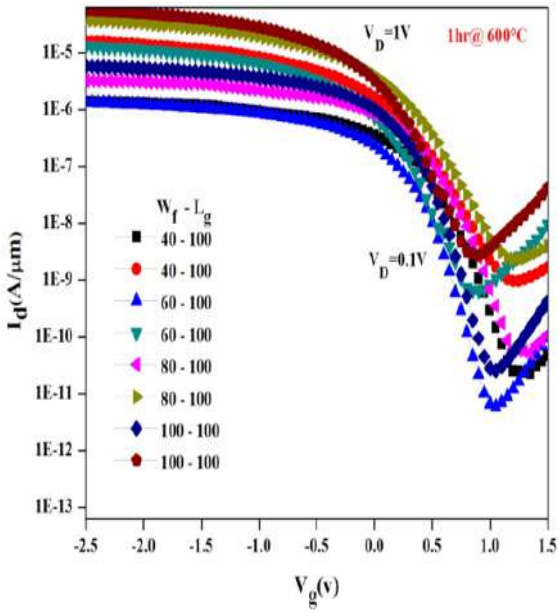

Figure 10. I_D vs V_G characteristics of the poly-Si / SiGe core-shell JAMFET at various fin width and fixed gate length of 100nm for 1hr at 600°C

DOI: https://doi.org/10.30564/ssid.v1i2.1399

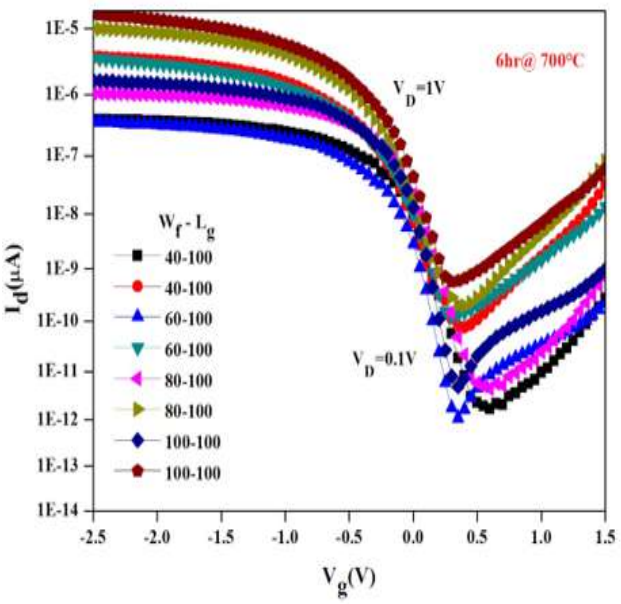

Figure 11. I_D vs V_G characteristics of the poly-Si / SiGe core-shell JAMFET at various channel width and fixed gate length of 100nm for 6hr at 700°C

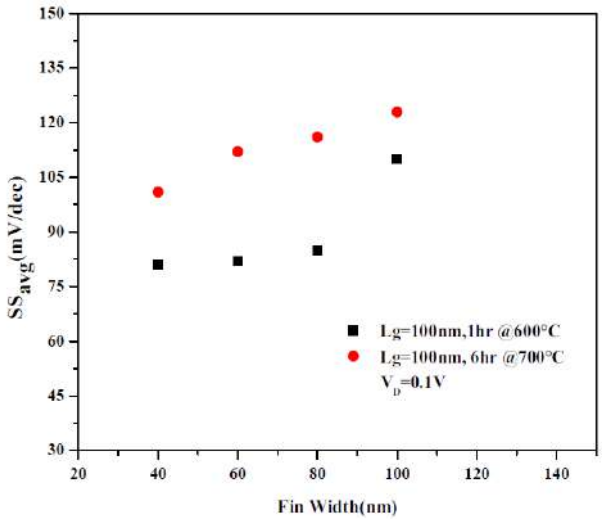

Figure 12. Distribution of subthreshold swing (SS) vs various channel width and fixed gate length of 100nm for 1hr at 600°C and 6hr at 700°C, respectively

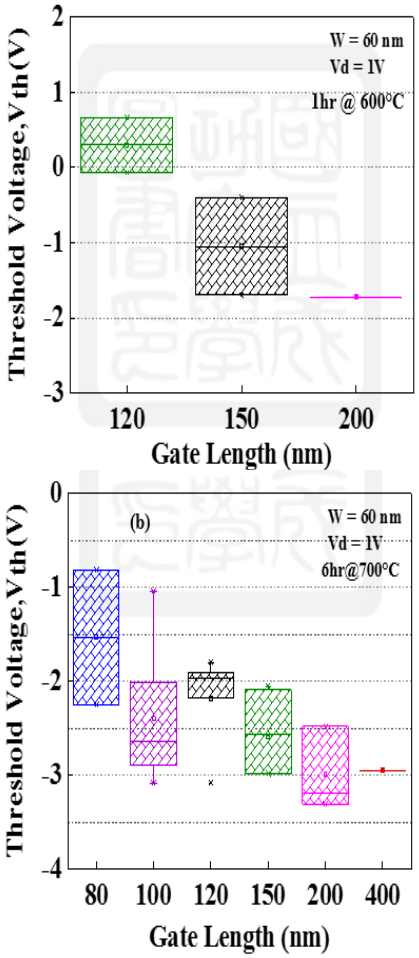

Figure 13. The comparison for statistic distributions of V_{th} for the poly-Si / SiGe core-shell JAMFETs at W_{ch} of 60 nm with different L_g for different annealing condition,(a) for 1hr at 600°C, (b) for 6hr at 700°C, respectively

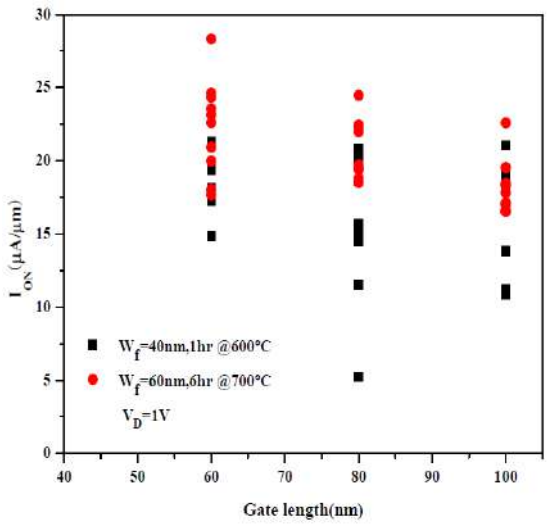

Figure 14. Dependency of ON current on gate length of poly-Si/SiGe core-shell JAMFET at channel width of 40nm for 1hr at 600°C and 60nm for 6hr at 700°C, respectively

 DOI: https://doi.org/10.30564/ssid.v1i2.1399

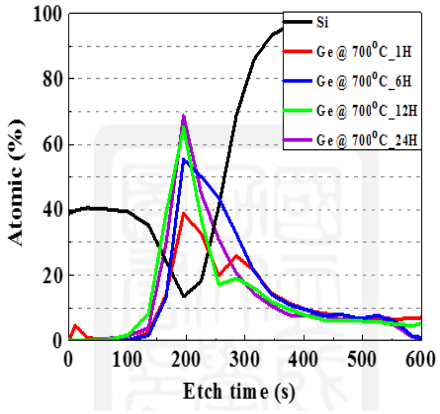

Figure 15. The depth profile of active region with four SiGe combination annealing condition,i.e.700°C_1hr,700°C,_6hrs, 700°C_12hrs and 700°C_24hrs

References

[1] Xiang, J., et al.. Ge/Si nanowire heterostructures as high-performance field-effect transistors. nature, 2006, 441(7092): 489.

[2] Jiang, Y., et al.. Omega-gate p-MOSFET with nanowirelike SiGe/Si core/shell channel. IEEE Electron Device Letters, 2009, 30(4): 392-394.

[3] Hashemi, P., et al.. Width-dependent hole mobility in top-down fabricated Si-core/Ge-shell nanowire metal-oxide-semiconductor-field-effect-transistors. Applied Physics Letters, 2010, 96(6): 063109.

[4] Woo Lee, J., et al.. Short channel mobility analysis of SiGe nanowire p-type field effect transistors: Origins of the strain induced performance improvement. Applied Physics Letters, 2012, 101(14): 143502.

[5] Schmidt, V., et al.. Silicon nanowires: a review on aspects of their growth and their electrical properties. Advanced Materials, 2009, 21(25-26): 2681-2702.

[6] David, T., et al.. Tailoring Strain and Morphology of Core–Shell SiGe Nanowires by Low-Temperature Ge Condensation. Nano letters, 2017, 17(12): 7299-7305.

[7] Pham, D., L. Larson, J.-W. Yang. FinFET device junction formation challenges. in 2006 International Workshop on Junction Technology. IEEE, 2006.

[8] Lee, C.-W., et al.. Junctionless multigate field-effect transistor. Applied Physics Letters, 2009, 94(5): 053511.

[9] Lee, C.-W., et al.. Performance estimation of junctionless multigate transistors. Solid-State Electronics, 2010, 54(2): 97-103.

[10] Colinge, J.-P., et al.. Nanowire transistors without junctions. Nature nanotechnology, 2010, 5(3): 225.

[11] Kim, T.K., et al.. First demonstration of junctionless accumulation-mode bulk FinFETs with robust junction isolation. IEEE Electron Device Letters, 2013, 34(12): 1479-1481.

[12] Kranti, A., et al. Junctionless nanowire transistor (JNT): Properties and design guidelines. in 2010 Proceedings of the European Solid State Device Research Conference. IEEE, 2010.

[13] Han, M.-H., et al.. Device and circuit performance estimation of junctionless bulk FinFETs. IEEE Transactions on Electron Devices, 2013, 60(6): 1807-1813.

[14] Park, C.-H., et al.. Electrical characteristics of 20-nm junctionless Si nanowire transistors. Solid-State Electronics, 2012, 73: 7-10.

[15] Leung, G. C.O. Chui, Variability impact of random dopant fluctuation on nanoscale junctionless FinFETs. IEEE Electron Device Letters, 2012, 33(6): 767-769.

[16] Rios, R., et al.. Comparison of junctionless and conventional trigate transistors with $ L_ {g} $ down to 26 nm. IEEE electron device letters, 2011, 32(9): 1170-1172.

[17] Jeon, D.-Y., et al.. Low-temperature electrical characterization of junctionless transistors. Solid-State Electronics, 2013, 80: 135-141.

[18] Hashemi, P., et al.. High-mobility high-Ge-content Si 1− x Ge x-OI PMOS FinFETs with fins formed using 3D germanium condensation with Ge fraction up to x~ 0.7, scaled EOT~ 8.5 Å and ~ 10nm fin width. in 2015 Symposium on VLSI Circuits (VLSI Circuits), IEEE, 2015.

[19] Adhikari, H., et al.. High mobility SiGe shell-Si core omega gate pFETS. in 2009 International Symposium on VLSI Technology, Systems, and Applications. IEEE, 2009.

[20] Sioncke, S., et al.. Etch rates of Ge, GaAs and InGaAs in acids, bases and peroxide based mixtures. ECS Transactions, 2008, 16(10): 451-460.

[21] Huygens, I.M., W.. Gomes, and K. Strubbe, Etching of germanium in hydrogenperoxide solutions. ECS Transactions, 2007, 6(2): 375-386

DOI: https://doi.org/10.30564/ssid.v1i2.1399

BILINGUAL PUBLISHING CO.
Pioneer of Global Academics Since 1984

Semiconductor Science and Information Devices
https://ojs.bilpublishing.com/index.php/ssid

ARTICLE

Intrinsic Photoconductivity of Few-layered ZrS2 Phototransistors via Multiterminal Measurements

Rukshan M. Tanthirige[1] Carlos Garcia[2] Saikat Ghosh[3] Frederick Jackson II[1] Jawnaye Nash[1] Daniel Rosenmann[4] Ralu Divan[4] Liliana Stan[4] Anirudha V. Sumant[4] Stephen A. McGill[2] Paresh C. Ray[1] Nihar R. Pradhan[1,2*]

1. Layered Materials and Device Physics Laboratory, Department of Chemistry, Physics and Atmospheric Science, Jackson State University, Jackson, MS 39217, USA
2. National High Magnetic Field Laboratory, Tallahassee, FL 32310, USA
3. Kunming University of Science and Technology, Kunming 650500, China
4. Center for Nanoscale Materials, Argonne National Laboratory, 9700 S-Cass Avenue, Lemont, IL-60439, USA

ARTICLE INFO

Article history
Received: 4 December 2019
Accepted: 17 December 2019
Published Online: 31 December 2019

Keywords:
Field-effect transistors
Zirconium sulphide
Phototransistor
Responsivity
Quantum efficiency

ABSTRACT

We report intrinsic photoconductivity studies on one of the least examined layered compounds, ZrS_2.Few-atomic layer ZrS_2 field-effect transistors were fabricated on the Si/SiO_2 substrate and photoconductivity measurements were performed using both two- and four-terminal configurations under the illumination of 532 nm laser source. We measured photocurrent as a function of the incident optical power at several source-drain (bias) voltages. We observe a significantly large photoconductivity when measured in the multiterminal (four-terminal) configuration compared to that in the two-terminal configuration. For an incident optical power of 90 nW, the estimated photosensitivity and the external quantum efficiency (EQE) measured in two-terminal configuration are 0.5 A/W and 120%, respectively, under a bias voltage of 650 mV. Under the same conditions, the four-terminal measurements result in much higher values for both the photoresponsivity (R) and EQE to 6 A/W and 1400%, respectively. This significant improvement in photoresponsivity and EQE in the four-terminal configuration may have been influenced by the reduction of contact resistance at the metal-semiconductor interface, which greatly impacts the carrier mobility of low conducting materials. This suggests that photoconductivity measurements performed through the two-terminal configuration in previous studies on ZrS_2 and other 2D materials have severely underestimated the true intrinsic properties of transition metal dichalcogenides and their remarkable potential for optoelectronic applications.

**Corresponding Author:*
Nihar R. Pradhan,
Layered Materials and Device Physics Laboratory, Department of Chemistry, Physics and Atmospheric Science, Jackson State University, Jackson, MS 39217, USA; National High Magnetic Field Laboratory, Tallahassee, FL 32310, USA;
Email: nihar.r.pradhan@jsums.edu

 DOI: https://doi.org/10.30564/ssid.v1i2.1526

1. Introduction

Transition Metal Dichalcogenides (TMDs) is one of the groups of two-dimensional layered crystals coupled through Van der Waals interactions that have attracted great attention in the research community for their promising potential in high performing electronic and optoelectronic devices [1–10]. They inherit strong interaction with light as most of their bandgaps lie in the visible region, high room temperature mobilities and conductivities have given them a unique position in the semiconductor industry [11,12]. Among the layered compounds, including those of group VIB and VIIB elements such as Mo, W and Re have been extensively studied compared to TMDs of group IVB elements; Zr, Hf and Rf. Despite the lack of attention, theoretical investigations suggest those monolayers Zr or Hf based TMDs may exhibit higher mobilities than that of group VIB counterparts [13]. In addition, ZrX_2 compounds (X: chalcogen) predicted to show strain-induced indirect-to-direct bandgap transitions [14,15] and even semiconductor-to-metal phase transitions [16]. MoS_2 has been the most widely studied TMD for its electrical and optical properties, particularly due to its direct bandgap of 1.8 eV in monolayer, tunable layer dependent band structure and natural availability [17,18]. In the monolayer, MoS_2 based field effect transistors (FETs) can achieve high ON/OFF current ratios in the order of 10^8 and high responsivity [19,20]. Previous studies report a wide range of responsivities from mA/W to 10^4 A/W [20–24] for monolayer and few-layered MoS_2 FETs, which depend on the incident optical power, source-drain (bias), back-gate voltages, and the type and quality of electrical contacts. Lopez-Sanchez et al. [20] reported a high responsivity of 880 A/W under a source-drain bias voltage of 8 V and an applied gate voltage of 60 V. However, Choi et al. [25] demonstrated that FETs based on multilayer MoS_2 have wider spectral range, high responsivity and high room temperature mobilities compared to that of monolayer MoS_2 FETs. Tsai et al. [26] observed that few-layered MoS_2 FETs exhibit high broadband gains (13.3), high detectivities (10^{10} $cmHz^{1/2}/W$) and ultrafast photoresponse (rise time of 70 μs and fall time of 110 μs). Pak et. al. [23] reported high responsivities for monolayer MoS_2 when the FET is in the ON state ($V_g > 0$ V), however in contrast, Lee et. al. [27] observed high responsivities for few-layered MoS_2 FETs while in the OFF state ($V_g < 0$ V).

Similar to MoS_2, other TMDs such $MoSe_2$ and WSe_2 have exhibited promising optoelectronic characteristics in both monolayer and few-layered forms [6,8]. Abderrahmane et. al. [28] observed an ultrahigh photosensitivity of 97.1 A/W and an impressive external quantum efficiency (EQE) of 22666% for a few-layered $MoSe_2$ FET at zero gate voltage. These observations signify that optoelectronic properties and transport mechanisms of MoS_2 and other TMD based FETs show a clear difference between monolayer and multilayer forms. WSe_2 is another layered TMD with bandgaps ranging from 1.3 eV (bulk) to 1.8 eV (monolayer) that shows p-type conductivity unlike MoS_2 or $MoSe_2$ [29]. Early studies showed that WSe_2 has a poor responsivity of 8 mW/A when the FET is in the OFF state, which increases drastically when the FET is set to the ON state, but it inherited poor switching speeds of 5 s [30]. In contrast, our previous study on tri-layer WSe_2 crystals synthesized via chemical vapor transport (CVT) showed high speed switching behavior of 5 μs [6]. Our most recent study on few-layered WSe_2 FETs showed promising optoelectronic properties with high responsivity of 85 A/W and ultrahigh EQE of over 19600% [31]. In addition, the metal contact semiconductor interface and the type of metal contacts play an important role on transport properties as they change the height of the Schottky barrier [30]. In addition to the electrical transport, their phototransport properties can be greatly affected by contact resistance [10,31].

Electrical transport measurements of most TMDs were conducted using two metal contacts, where both current and voltage are sourced and measured using the same terminals, in which contact resistance can dominate the transport properties. Although the contacts-driven carrier mobility can be utilized in certain applications such as in gas sensing devices [32], it hinders the ability to investigate intrinsic properties of semiconductor devices. Some of the recent reports claim observing intrinsically higher carrier mobilities and conductivities with four terminal measurements, i.e. two terminals to measure/inject the current and the other two terminals use to sense the voltage drop across the channel [4,9,10,33]. The advantage of four-terminal configuration is that it eliminates the influence of the contact resistance, which is vital when measuring intrinsic material transport properties of materials with low carrier mobilities. For the search of new materials and their functional properties, here we explored the phototransport properties of a few- layered ZrS_2 phototransistor with four terminals, which has not been reported in the literature. The bandgap of bulk ZrS_2 is 1.4 eV,

DOI: https://doi.org/10.30564/ssid.v1i2.1526

whereas the monolayer shows 2 eV [34,35]. The reported mobility of few-layered ZrS_2 FET varies between 0.1 - 1 cm^2/Vs [36–38]. Further, electrical transport studies of the ZrS_2 nanobelts show extremely high photoresponsivity [16] under UV light illumination despite its poor mobility of 1 10^{-5} cm^2/Vs. In this study, we performed photoconductivity measurements of two-dimensional ZrS_2 FET with both two-terminal and four-terminal configurations. The main aim is to characterize intrinsic optical properties of this less known compound for various electro-optic devices as a single component or in heterostructure, which is one of the current focuses of 2D research. We observed a significant improvement in photo conductivity with the four-terminal configuration, just by restricting the role of the contact resistance. The measured photoresponsivity (R) and external quantum efficiency (EQE) with the four–terminal configuration was enhanced by 1200% compared to that with the two-terminal measurements for the same device. These results are in good agreement with those for WSe_2 phototransistors in our recent study [31], in which we observed a 370% and a 461% higher photoresponsivity and EQE, respectively, with the four-terminal configuration. Thus, we believe that intrinsic electrical and optical properties of TMDs are significantly higher than their previously reported values, which opens new possibilities for improved photo-transistors and related devices where contact resistance play a significant role in measuring transport properties of the materials.

2. Results and Discussion

Few layered ZrS_2 single crystals were grown by chemical vapor transport (CVT) technique using the procedure used to grow other TMDs such as WSe_2, $MoSe_2$, MoS_2, ReS_2 etc. [29,31]. Thin layers of ZrS_2 were mechanically exfoliated from bulk crystal using scotch tape technique and subsequently transferred on to a clean 270 nm thick SiO_2 film grown on a p-doped Si substrate. Single to few-layered ZrS_2 flakes were identified by optical and atomic force microscopy. These layered crystals were characterized by Raman spectroscopy to verify their composition and crystal quality. Figure 1 presents the Raman spectrum of the ZrS_2 layer using a laser source of wavelength λ= 532 nm for varying thicknesses of ZrS_2 flakes. Here, the strong signal at 330 cm^{-1} represents the characteristic out-of-plane mode (A_{1g}) of ZrS_2, which increases with the sample thickness from bilayer (2L) to nearly twenty atomic layers (20L). The weak E_g mode is at 247 cm^{-1}. These observed Raman modes are similar to the previously observed Raman data on few-layered ZrS_2 crystals [35,36,39]. Figure 1 (b)-(d) display the optical micrograph images of layered ZrS_2 crystals exfoliated on to the Si/SiO_2 substrate. Raman data was collected from the several exfoliated flakes to verify the crystal quality. Supplementary Figure S1 shows AFM height image with height trace of one of the exfoliated ZrS_2 thin flakes.

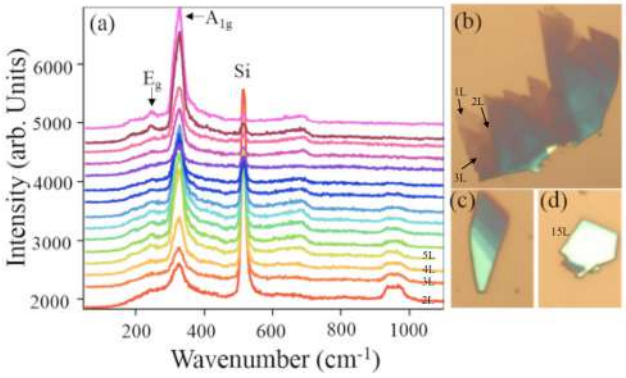

Figure 1. (a) Thickness dependent Raman spectrum of ZrS_2 crystals on Si/SiO_2 substrate. The Raman modes A_{1g} and E_g are labeled. (b)-(d) are the optical micrograph images of exfoliated ZrS_2 crystals showing single layer to few atomic layers of flakes

The field-effect transistor (FET) was fabricated on 285 nm thick p-doped Si/SiO_2 substrate by electron-beam lithography and electron beam evaporation technique. The devices were annealed at T = 300° C in forming gas followed by high vacuum annealing for 20 hours at 120° C. Figure 2(a) shows an optical micrograph image of a ZrS_2 FET device with four terminal contacts of Cr (5 nm)/Au (80 nm) with two voltage (V_1 and V_2) and two current leads (S and D) to measure the photoconductivity. To evaluate photon induced transport properties in the two-terminal configuration, the two voltage leads (S and D) were used to source voltage and measure the current of the device. The back-gate voltage (V_{bg}) was applied between the p-doped Si substrate and the source, and was varied to control the charge accumulation in the channel. Figure 2(b) illustrates the schematics of the FET and typical measurements obtained in the presence of a 532 nm laser under ambient conditions in a dark room environment. A dual channel Keithley Sourcemeter model 2612A was employed to apply the source-drain voltage (V_{ds}) (V_{ds} is applied between V_1 and V_2 in four-terminal configuration) and measure the source-drain current (I_{ds}), and the model 2635 was used to apply and control the gate voltage.

 DOI: https://doi.org/10.30564/ssid.v1i2.1526

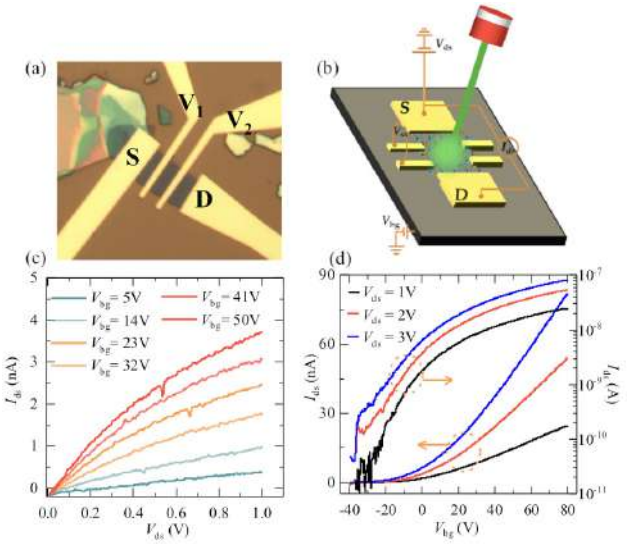

Figure 2. Optical micrograph image of ZrS_2 FET in multi-terminal contacts fabricated on the Si/SiO_2 substrate using Cr/Au (5/80 nm thick) metals. The thickness of the flake is 8-10 nm. (b) Schematic of the device and measurement scheme. (c) I_{ds} vs V_{ds} at several applied constant V_{bg} and (d) I_{ds} vs V_{bg} at constant V_{ds} = 1, V, 2V and 3V in the linear and logarithmic scale.

Figure 2(c) shows the source-drain current (I_{ds}) measured as a function of the source-drain voltage (V_{ds}) in the four-terminal configuration at several applied gate voltages (V_{bg}) from 5 V to 50 V. At lower V_{bg} values, 5 V and 14 V, the I_{ds} - V_{ds} plot shows a near linear behavior. This can be ascribed to the thermionic emission of carriers between metal contacts and ZrS_2 layer above the Schottky barrier at room temperature. However, for higher applied gate voltages (V_{bg}), the source-drain current (I_{ds}) starts displaying a non-linear variation with increasing source-drain voltage (V_{ds}). This nonlinear behavior can be attributed to non-ohmic contacts due to high Schottky barrier height between metal contacts and the few-layered ZrS_2 semiconducting channel. Figure 2(d) presents the measured I_{ds} as a function of applied gate voltage V_{bg} for constant source-drain voltages V_{ds} from 1 V to 3 V. The plot on the left current-axis displays the linear variation of I_{ds} with respect to V_{bg}. The I_{ds} with positive applied gate voltages (V_{bg}) affirms that the ZrS_2 sample is electron-doped or n-type FET. The plot using the right current-axis, shows the same variation of source-drain current (I_{ds}) in the semi-logarithmic scale as a function of V_{bg}. The observed ON to OFF current ratio of the few-layered ZrS_2 FET is 10^4. This current is much smaller than that showed by other TMDs such as MoS_2, WSe_2 reported in the literature but agrees with the results by Zhu et al. [38] on ZrS_2 FETs. Considering the linear region (V_{bg} > 50 V) of the I_{ds} vs V_{bg} plot, the four-terminal field-effect mobility of the FET can be calculated by the following equation [4,31].

$$\mu = \frac{l_v}{WC_i}\frac{1}{C_i}\frac{d(I_{ds}-I_o)/V_{ds}}{dV_{bg}} \quad (1)$$

Where, l_v is the length of the channel between voltage leads V_1 and V_2, V_{ds} (=V_{12}) is the voltage between V_1 and V_2, and I_o is the off current, W is the channel width. Ratio l_v/W for our device in 0.6. C_i is the gate capacitance per unit area, given by $C_i = \varepsilon\varepsilon_o/d$ = 11.7 x 10^{-9} F/cm^2. Where, ε and ε_o are the dielectric constant of SiO_2 and the permitivity of free space, respectively, and d is the thickness of the dielectric material, i.e. 285 nm for the SiO_2 layer used in our experiment. The four-terminal electron-mobility of this device calculated from equation (1) is 0.5-1 cm^2/Vs at room temperature. Similar mobilities of ZrS_2 FETs were reported previously on Si/SiO_2 substrate [36] or even when FET is fabricated on the h-BN substrate [37]. This value is much larger than the reported mobility by Shimazu et al. [39] measured on a 28 nm thick flake. In contrast, the four terminal mobilities of WSe_2 and MoS_2 are 145 cm^2/Vs [31] and 306 cm^2/Vs [4], respectively. This shows that ZrS_2 is too resistive; hence any attempt to find the two-terminal mobilities is highly affected by the contact resistance. In our previous studies on MoS_2 based FETs, we observed a similar pattern, i.e. the four-terminal mobility is significantly larger than the two-terminal mobility [4]. Mobility on ZrS_2 FET can be improved further by using suitable metal contacts or 2D metallic contacts like graphene and substrate where density of charge trap is lower than the rough Si/SiO_2 substrate. The low mobility could be attributed to defects and impurities in the crystals from CVT technique where transport agents were used for the synthesis.

We conducted both two-terminal and four-terminal photoconductivity measurements using a home-made microscope and data acquisition system equipped with a 532 nm monochromatic laser in darkroom environment. These values were compared with standard two-terminal photoconductivity measurements to evaluate the near intrinsic photoresponse of ZrS_2. More details of the experimental setup and the technique are explained in our previous study, performed to evaluate intrinsic photoresponse of WSe_2 [31]. Since the laser spot was larger than the sample size, the power illuminated on the sample P_{opt} can be estimated by,

$$P_{opt} = \frac{P}{\pi r^2}A \quad (2)$$

Where r, P and A are the radius of the laser spot, the power of the laser and the area of the sample, respectively. The radius of the laser spot (r) was measured using a lithographically patterned marker on the substrate. The dark current, I_{dark} was measured by varying the source-

DOI: https://doi.org/10.30564/ssid.v1i2.1526

drain voltage V_{ds} from 50 mV to 650 mV, in the absence of any laser illumination on the sample, i.e. $I_{dark} = I_{ds}$ for P = 0 W. The back-gate voltage (V_{bg}) was kept at -40 V to ensure that the device is in the OFF state. Next, I_{ds} was recorded as a function of P_{opt} by sweeping the laser power (P) from 10 nW to 50 μW using the attenuator. The back-gate voltage (V_{bg}) was fixed at -40 V and the source-drain voltage (V_{ds}) was varied from 50 mV to 650 mV for each set of measurements. The photo-induced current (I_{ph}) was calculated by subtracting the dark current from I_{ds} obtained by illuminating with light, i.e. $I_{ph} = I_{light} - I_{dark}$, measured at the same source-drain voltage (V_{ds}). I_{ph} shows a sudden rise and then a gradual increase with P_{opt} in both two and four-terminal configurations (See supporting information Figure S2). Figure-3 (a) and (b) show the photoresponsivity (R) of the device, $R = I_{ph}/P_{opt}$, as a function of optical power (P_{opt}) illuminated on the sample, for both two-terminal and four-terminal configurations. In the logarithmic scale, R decreases almost linearly as a function of increasing optical power, indicating that trap states in ZrS_2 layer or at the interface between ZrS_2 and SiO_2 play a dominant role. This indicates that ZrS_2 based FETs are suitable for high sensitive optical detection with low optical power as the trap states can significantly alter the sensitivity and efficiency of photo detectors. In addition, both the photocurrent and the photoresponsivity gradually increase with the source-drain voltage (V_{ds}). For the two-terminal configuration, the responsivity increases from 0.03 A/W at 50 mV to 0.5 A/W at 650 mV, when the optical power on the sample (P_{opt}) is approximately 90 nW. However, in the four-terminal configuration, the responsivity rises from 0.14 A/W at 50 mV to 6 A/W at 650 mV for the same (P_{opt}). Thus, the responsivity values extracted from the four-terminal measurements are significantly larger than the values extracted from two-terminal measurements. This increase in responsivity in four-terminal measurements is due to the elimination of contact resistance associated with the metal and semiconductor junction. The highest responsivity, R for two-terminal measurements, 0.5 A/W at V_{ds} = 650 mV and V_{bg} = -40 V, jumps to 6 A/W in the four-terminal measurements under the same V_{ds} and V_{bg}, which is nearly a 1200% enhancement. Our measured R value is much higher than the reported value for the same material by Wang et al. [36]. These values of R are also two orders of magnitude higher than the reported results by Mattinen et al., where they used Atomic Layer Deposition (ALD) method to synthesize large scale ZrS_2 crystals [40]. By fitting the responsivity as a function of optical power on the sample to the power law $R \alpha P^{-\gamma}$, when V_{ds} = 650 mV, we obtained the γ = 0.84 and γ = 0.87 for the two-terminal and four-terminal configurations, respectively.

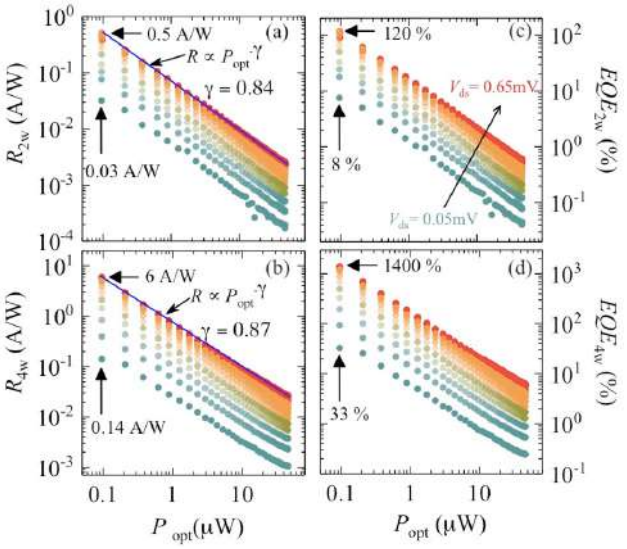

Figure 3. (a) and (b) display the photoresponsivity measured in two- and four-terminal configurations respectively as a function of incident optical power. (c) and (d) are the estimated external quantum efficiencies (EQE) for two- and four-terminal measurements for few layered ZrS_2 phototransistor. Blue solid lines in (a) and (b) are the least square fit to the experimental data

Next, we estimate the external quantum efficiency (EQE), which is defined as the number of electron-hole pairs generated by the number of photons illuminated on the phototransistor, using the following expression [10,31].

$$EQE = \frac{I_{ph}}{P_{opt}} \frac{hc}{\lambda q} = R \times \frac{hc}{\lambda q} \quad (3)$$

Where, P_{opt} is the optical power incident on the sample, h is the plank constant, c is the speed of light, λ is the wavelength of the laser source, and q is the electron charge. As shown in Figure 3 (c) and (d), the EQE follow a similar variation as R as a function of optical power (EQE $\propto R^{-\alpha}$). In the logarithmic scale, EQE decreases linearly with increasing P_{opt} at constant source-drain and back-gate voltages in the FET's OFF state, and EQE increases with the source-drain voltage for a given optical power on the sample. EQE increases from 8% to 120% when the source-drain voltage is increased from 50 mV to 650 mV in two-terminal measurements, however, it jumps from 33% to 1400% for the same source-drain voltage interval in the four-terminal configuration. This very high quantum efficiency of 1400% in four-terminal measurements compared to that estimated through two-terminal measurements, 120%, signifies that the four-terminal configuration produces a considerably higher EQE. This is nearly 1200% increase compared to the much adopted two-terminal configuration. In one of our previous studies to

 DOI: https://doi.org/10.30564/ssid.v1i2.1526

determine the photoresponsivity of WSe_2, we made a similar observation, where the EQE increased by 344% when it was estimated using a four-terminal configuration [31]. The linear decrease of EQE with increasing incident optical power has been observed for other 2D crystals [10,31] and believed to be a result of electron-hole recombination, which may have been stimulated by the radiation. However, the observed high EQE values in this study indicate that the recombination process is either hindered or enhanced by the generation of electron- hole pairs caused by the large surface to volume ratio of our few-layered ZrS_2 device. EQE values exceeding 100% suggests that one photon may have generated multiple electron-hole pairs, however the excitation frequency remains too low for this to occur. Studies performed by Li et. al. [41] and Ulanganathan et. al. [42] claim that high EQE and photoresponsivity are due to localized trapped states that slows the recombination process. They argue that one type of photo generated carriers is trapped in localized states, which expands the lifespan of the other carriers to circulate multiple times through the channel and source meters before the recombination. This process enhances the effective gain of the device as one photon seems to have created a substantially large photo-induced current due to slow a recombination process. This process yields EQE values exceeding 100%.

This study was performed for a single wavelength (λ=532 nm) as we focused on finding the dependence of photoresponsivity and photoinduced current on incident optical power in a multi-terminal configuration. The dark current was primarily due to thermally excited minority charge carriers. When the device is illuminated, the total current comes from thermally excited minority charge carriers (dark current), photogenerated current by electron-hole pairs, and the current induced by the photo thermoelectric effect (PTE) at the metal-semiconductor interface [43], as the whole device is exposed to the laser radiation, i.e. both the Cr/Au metal contacts and ZrS_2 semiconducting channel. Under laser illumination, the metal contacts become warmer than the semiconductor and their difference in Seebeck coefficients induces a net current flow across the metal-semiconductor interface, from the metal (hot) to semiconductor (cold) [43]. Since the size of the laser spot (700-800 μm^2) is much larger that the area of the device including metal contacts (100 μm^2), the net current flow across the channel due to PTE should be zero, as the currents from the two metal contacts to the semiconductor flow on opposite directions and cancels out. This leaves the dark current and the photogenerated current as contributing factors when the device is under illumination.

The dependence of R and EQE in the four-terminal configuration with the source-drain voltage (V_{ds}) in the logarithmic scale is shown in Figure 4, based on extracted data from Figure 3 (c) and (d), for selected incident optical powers. Upon fitting with the power law ($R \propto V^{-\alpha}$), we found that the dependence of R with V_{ds} is slightly non-linear with exponent α=1.6. The highest value estimated for R is 6 A/W at V_{ds} = 650 mV and P_{opt} = μW that significantly decreases as we increase the optical power. However, previous studies have reported very high responsivities for WSe_2 phototransistors under ultra-low incident optical power and higher bias voltages [28]. This mismatch might have come from the low absorption of ZrS_2 at 532 nm compared to that of WSe_2. ZrS_2 shows high absorption in the range of 300 nm to 400 nm in heterostructure geometry with h-BN or graphene compared to 532 nm in WSe_2 [44]. The responsivity also largely depends upon the incident optical power, applied drain-source and gate voltages used. As an example, a high R of 880 A/W was reported for monolayer MoS_2 based FETs under a very low incident optical power of 150 pW (V_{ds} = 8 V and V_{bg} = -70 V), which sharply dropped to 4 A/W as the incident optical power increased to 250 nW [20]. In comparison, the R value estimated in our study for ZrS_2 FET at 250 nW (0.25 μW) and V_{ds} = 650 mV (0.65 V) is approximately 2 A/W (Fig- ure 3 b), which can be extrapolated to approximately 110 A/W at V_{ds} = 8 V (Figure 4 a). This is in good agreement with our previous study on few-layered WSe_2, which shows a very high R value when it was measured with the four-terminal configuration (R = 85 A/W at P_{opt} = 248 nW and V_{ds} = 1 V) [31]. This illustrates that the four-terminal configuration-based measurements have resulted in a much higher R and EQE values than those of previously reported on ZrS_2 phototransistor.

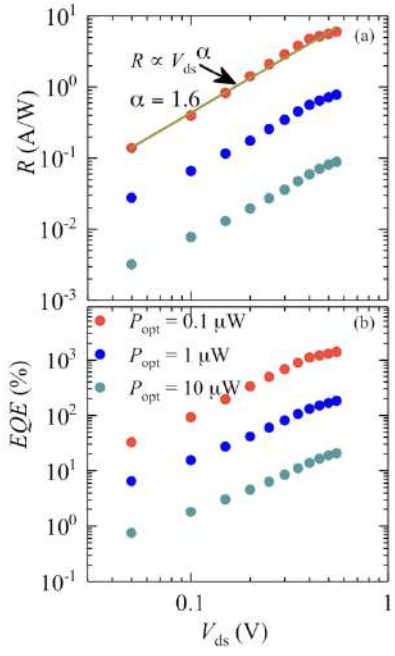

Figure 4. (a) Responsivity and (b) EQE as a function of V_{ds} extracted at constant illuminated optical power. Red line rep-resents the fitting of R in power law to extract the exponent α

DOI: https://doi.org/10.30564/ssid.v1i2.1526

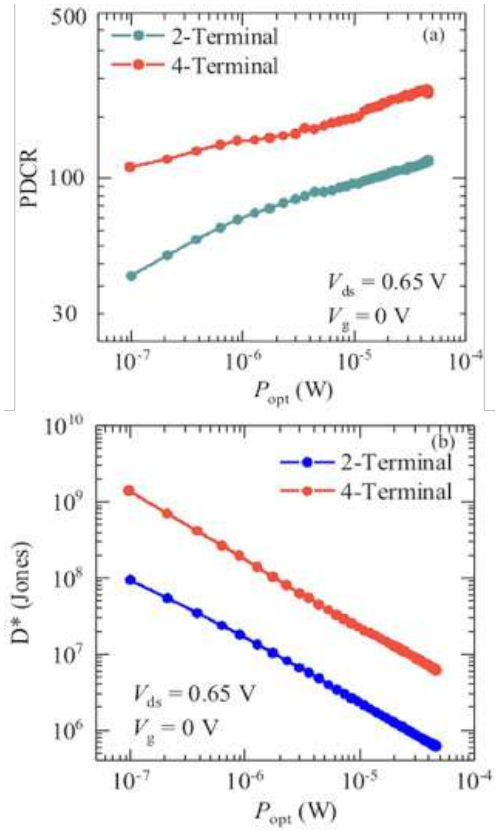

Figure 5. (a) PDCR and (b) Detectivity of few layered ZrS2 phototransistor as a function of illuminated optical power

We further explored the photo dark current ratio (PDCR) and detectivity (D) of our ZrS_2 based photo-transistor as presented in Figure 5, which demonstrates the photodetection application and the figure of merit to use for the performance of photodetector of ZrS_2 based phototransistor. PDCR is estimated by measuring the ratio of photocurrent and dark current (PDCR = $(I_{light} - I_{dark})/I_{dark} = I_{ph} / I_{dark}$, where I_{light} is the current measured with light illuminated and I_{dark} is the dark current with no light illumination. Figure 5 (a) shows the PDCR values of few layered ZrS_2 measured in two and four-terminal configurations as a function of increasing optical power. The PDCR values measured in 4-terminal method ranges between 100 at 0.1 μW and 275 at 0.4 mW optical power under applied V_{ds} = 0.65 V, which are much higher than some of the reported photodetectors currently in use such as AlN, GaN, SiC, Ga_2O_3 etc. [45-48] and similar to the MoS_2 photodetector reported earlier [26]. The specific detectivity is extracted from the relation given by $D^* = R\sqrt{A} / \sqrt{2qI_{dark}}$, where R is the photoresponsivity, A is the area of the detector, q is the unit of charge, and I_{dark} is the dark current. As shown in Figure 5 b, D^* varies linearly with optical power from 10^7 Jones at 1 mW power to 10^9 Jones at 0.1 μW incident optical power in the OFF state of the transistor (V_{bg} = 0 V) and small V_{ds} = 0.065 V. Similar detectivities were also reported on few layered MoS_2 [26]. Higher value of the detectivity can be obtained in the ON state of the transistor and by applying higher V_{ds} [30].

3. Conclusion

We report the intrinsic photo transport properties of few layered ZrS_2 phototransistors measured with multi- terminal configuration. We studied the dependence of photocurrent, photoresponsivity and the external quantum efficiency as a function of incident optical power and bias voltage when the FET is in the OFF state at a fixed back-gate voltage. The estimated photoresponsiv ity R and EQE values show that four-terminal measurements result extremely high values, at least one order of magnitude higher than that with two-terminal configurations. This clearly indicates that the optical properties of FETs based on few-layered TMDs can be significantly enhanced by minimizing the contact resistance. Here, the ZrS_2 FET with approximately 10 atomic layers of ZrS_2 shows an impressive R and EQE values through four-terminal measurements representing an improvement of 1200%, over the values estimated through traditional two-terminal configuration. Furthermore, few-layered ZrS_2 shows an excellent photo sensitivity factor (PDCR) that is up to 275 at low applied bias and zero gate voltage when measured in four-terminal configuration. Few-layered ZrS_2 also shows high detectivity at low incident optical power. This signifies that a four-terminal configuration is more suitable when investigating intrinsic optoelectronic properties of TMD based FETs, particularly 2D materials where contact resistance plays a crucial role to determinate of incident the intrinsic transport properties, which can be ultimately utilized for the fabrications of devices that require high yields and high sensitivities. We believe that measuring the intrinsic optoelectronic properties of 2D materials, TMDs would make them promising candidates for a wide range of future applications. The electrical and optical properties of ZrS_2 reported here will guide to fabricate heterostructure devices based 2D TMDS where ZrS_2 can provide the high yields and sensitivities required for optical applications.

Acknowledgments

N. R. P. acknowledged NSF-PREM through NSF-DMR-1826886, HBCU-UP Excellence in research NSF-DMR-1900692. A portion of this work was performed at the National High Magnetic Field Laboratory, which is supported by the National Science Foundation Cooperative Agreement No. DMR-1644779 and the State of Flor-

 DOI: https://doi.org/10.30564/ssid.v1i2.1526

ida. This work was performed, in part, at the Center for Nanoscale Materials, a U.S. Department of Energy Office of Science User Facility, and supported by the U.S. Department of Energy, Office of Science, under Contract No. DE-AC02-06CH11357.

Supporting Information

The supplementary materials contain the Figure S1, which is the variation of photocurrent as a function of incident optical power under different bias voltages for both two-terminal and four- terminal configurations.

Supplementary Materials

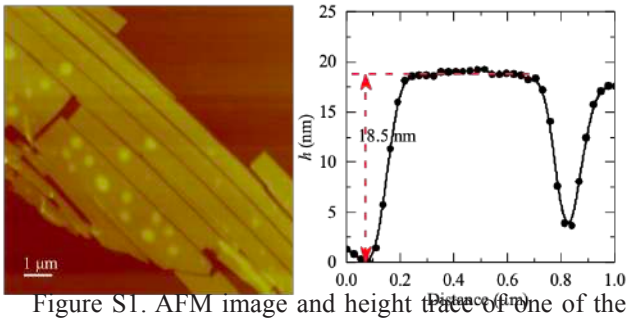

Figure S1. AFM image and height trace of one of the exfoliated flakes of ZrS_2 on to Si/SiO_2 substrate

Note: AFM height measurements were performed on several exfoliated crystals of ZrS_2 on Si/SiO_2 substrate using Veeco Dimension 3100 AFM setup. The flakes used for optical measurements are from 8 nm to 15 nm thick.

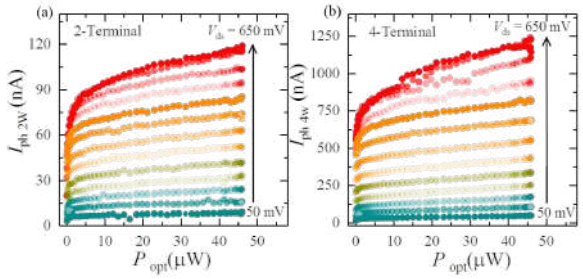

Figure S2. Photocurrent vs incident optical power

Note: The photocurrent as a function of incident optical power under several bias voltages for (a) two-terminal configuration (b) four-terminal configuration (I_{ph2W} and I_{ph4W} denote the photocurrent with two and four-terminal configurations, respectively). The four-terminal photocurrent is significantly larger (>1000 %) than the two-terminal current. Under both configurations, the photocurrent increases with the bias voltage.

References

[1] H. Wang, L. Yu, Y. H. Lee, Y. Shi, A. Hsu, M. L. Chin, L.J. Li, M. Dubey, J. Kong, T. Palacios. Integrated circuits based on bilayer MoS2 transistors, Nano letters, 2012, 12: 4674.

[2] B. Radisavljevic, A. Radenovic, J. Brivio, V. Giacometti, A. Kis. Single-layer MoS2 transistors, Nature nanotechnology, 2011, 6: 147.

[3] N. R. Pradhan, D. Rhodes, S. Feng, Y. Xin, S. Memaran, B.-H. Moon, H. Terrones, M. Terrones, and L. Balicas, Field-effect transistors based on few-layered α-MoTe2, ACS nano, 2014, 8: 5911.

[4] N. Pradhan, D. Rhodes, Q. Zhang, S. Talapatra, M. Terrones, P. Ajayan, L. Balicas. Intrinsic carrier mobility of multi-layered mos2 field-effect transistors on SiO2, Applied Physics Letters, 2013, 102: 123105.

[5] N. R. Pradhan, D. Rhodes, Y. Xin, S. Memaran, L. Bhaskaran, M. Siddiq, S. Hill, P. M. Ajayan, L. Balicas. Ambipolar molybdenum diselenide field-effect transistors: field-effect and hall mobilities, Acs Nano, 2014, 8: 7923.

[6] N. R. Pradhan, J. Ludwig, Z. Lu, D. Rhodes, M. M. Bishop, K. Thirunavukkuarasu, S. A. McGill, D. Smirnov, L. Balicas. High photoresponsivity and short photoresponse times in few-layered WSe2 transistors, ACS applied materials & interfaces, 2015, 7: 12080.

[7] S. Memaran, N. R. Pradhan, Z. Lu, D. Rhodes, J. Lud- wig, Q. Zhou, O. Ogunsolu, P. M. Ajayan, D. Smirnov, A. Fernandez-Dom´ınguez, et al.. Pronounced photovoltaic response from multilayered transition-metal dichalcogenides pn-junctions, Nano letters, 2015, 15: 7532.

[8] N. R. Pradhan, Z. Lu, D. Rhodes, D. Smirnov E. Manousakis, L. Balicas. An optoelectronic switch based on intrinsic dual schottky diodes in ambipolar MoSe2 field-effect transistors, Advanced Electronic Materials, 2015, 1: 1500215.

[9] N. R. Pradhan, C. Garcia, B. Isenberg, D. Rhodes, S. Feng, S. Memaran, Y. Xin, A. McCreary, A. R. H. Walker, A. Raeliarijaona, et al.. Phase modulators based on high mobility ambipolar rese 2 field-effect transistors, Scientific reports, 2018, 8: 12745.

[10] C. Garcia, N. Pradhan, D. Rhodes, L. Balicas. S. McGill. Photogating and high gain in res2 field-effect transistors, Journal of Applied Physics, 2018, 124: 204306.

[11] G. Fiori, F. Bonaccorso, G. Iannaccone, T. Palacios, D. Neumaier, A. Seabaugh, S. K. Banerjee, L. Colombo. Electronics based on two-dimensional materials, Nature nanotechnology, 2014, 9: 768.

[12] Q. H. Wang, K. Kalantar-Zadeh, A. Kis, J. N. Coleman, M. S. Strano. Electronics and optoelectronics of two-dimensional transition metal dichalcogenides, Nature nanotechnology, 2012, 7: 699.

[13] W. Zhang, Z. Huang, W. Zhang, Y. Li. Two-dimensional semiconductors with possible high room temperature mobility, Nano Research, 2014, 7: 1731.

[14] H. Guo, N. Lu, L. Wang, X. Wu, X. C. Zeng, Tuning

DOI: https://doi.org/10.30564/ssid.v1i2.1526

electronic and magnetic properties of early transition-metal dichalcogenides via tensile strain, The Journal of Physical Chemistry C, 2014, 118: 7242.

[15] Y. Li, J. Kang, J. Li. Indirect-to-direct band gap transition of the ZrS2 monolayer by strain: first- principles calculations, Rsc Advances, 2014, 4, 7396.

[16] A. Kumar, H. He, R. Pandey, P. Ahluwalia, K. Tankeshwar, Semiconductor-to-metal phase transition in monolayer ZrS2: Gga+ u study, in AIP Conference Proceedings (AIP Publishing, 2015, 1665: 090016.

[17] H. J. Conley, B. Wang, J. I. Ziegler, R. F. Haglund Jr, S. T. Pantelides, K. I. Bolotin. Bandgap engineering of strained monolayer and bilayer MoS2, Nano letters, 2013, 13: 3626.

[18] T. Cheiwchanchamnangij, W. R. Lambrecht, Quasi-particle band structure calculation of monolayer, bilayer, and bulk MoS2, Physical Review B, 2012, 85: 205302.

[19] K. F. Mak, C. Lee, J. Hone, J. Shan, T. F. Heinz, Atomically thin MoS2: a new direct gap semiconductor, Physical review letters, 2010, 105: 136805.

[20] O. Lopez-Sanchez, D. Lembke, M. Kayci, A. Raden-ovic, A. Kis. Ultrasensitive photodetectors based on monolayer MoS2, Nature nanotechnology, 2013, 8: 497.

[21] Z. Yin, H. Li, H. Li, L. Jiang, Y. Shi, Y. Sun, G. Lu, Q. Zhang, X. Chen, H. Zhang. Single-layer MoS2 phototransistors, ACS nano, 2011, 6: 74.

[22] D. Kufer, G. Konstantatos. Highly sensitive, encapsulated MoS2 photodetector with gate controllable gain and speed, Nano letters, 2015, 15: 7307.

[23] J. Pak, J. Jang, K. Cho, T.-Y. Kim, J.-K. Kim, Y. Song, W.-K. Hong, M. Min, H. Lee, T. Lee. Enhancement of photodetection characteristics of MoS2 field effect transistors using surface treatment with copper phthalocyanine, Nanoscale, 2015, 7: 18780.

[24] G. Wu, X. Wang, Y. Chen, Z. Wang, H. Shen, T. Lin, W. Hu, J. Wang, S. Zhang, X. Meng, et al.. Ultrahigh photoresponsivity MoS2 photodetector with tunable photocurrent generation mechanism, Nanotechnology, 2018, 29: 485204.

[25] W. Choi, M. Y. Cho, A. Konar, J. H. Lee, G.-B. Cha, S. C. Hong, S. Kim, J. Kim, D. Jena, J. Joo, et al.. High-detectivity multilayer MoS2 phototransistors with spectral response from ultraviolet to infrared, Advanced materials, 2012, 24: 5832.

[26] D.-S. Tsai, K.-K. Liu, D.-H. Lien, M.-L. Tsai, C.-F. Kang, C.-A. Lin, L.-J. Li, J.-H. He. Few-layer MoS2 with high broadband photogain and fast optical switching for use in harsh environments, Acs Nano, 2013, 7: 3905.

[27] H. S. Lee, S.-W. Min, Y.-G. Chang, M. K. Park, T. Nam, H. Kim, J. H. Kim, S. Ryu, S. Im. Mos2 nanosheet phototransistors with thickness-modulated optical energy gap, Nano letters, 2012, 12: 3695

[28] A. Abderrahmane, P. Ko, T. Thu, S. Ishizawa, T. Takamura, and A. Sandhu, High photosensitivity few-layered MoSe2 back-gated field-effect phototransistors, Nanotechnology 25, 365202 (2014).

[29] N. Pradhan, D. Rhodes, S. Memaran, J. Poumirol, D. Smirnov, S. Talapatra, S. Feng, N. Perea-Lopez, A. Elias, M. Terrones, et al.. Hall and field-effect mobilities in few layered *p*-WSe2 field-effect transistors, Scientific reports, 2015, 5: 8979.

[30] W. Zhang, M.-H. Chiu, C.-H. Chen, W. Chen, L.-J. Li, A. T. S. Wee. Role of metal contacts in high-performance phototransistors based on wse2 monolayers, ACS nano, 2014, 8: 8653.

[31] N. R. Pradhan, C. Garcia, J. Holleman, D. Rhodes, C. Parker, S. Talapatra, M. Terrones, L. Balicas, S. A. McGill, Photoconductivity of few-layered *p*-WSe2 phototransistors via multi-terminal measurements, 2D Materials, 2016, 3: 041004.

[32] N. Huo, S. Yang, Z. Wei, S.-S. Li, J.-B. Xia, J. Li, Photoresponsive and gas sensing field-effect transistors based on multilayer WS2 nanoflakes, Scientific reports, 2014, 4: 5209.

[33] N. R. Pradhan, A. McCreary, D. Rhodes, Z. Lu, S. Feng, E. Manousakis, D. Smirnov, R. Namburu, M. Dubey, A. R. Hight Walker, et al.. Metal to insulator quantum-phase transition in few-layered ReS2, Nano letters, 2015, 15: 8377.

[34] Y. Wen, Y. Zhu, S. Zhang. Low temperature synthesis of ZrS2 nanoflakes and their catalytic activity, RSC Advances, 2015, 5: 66082.

[35] S. Manas-Valero, V.Garcıa-Lopez, A.Cantarero, M. Galbiati. Raman spectra of ZrS2 and ZrSe2 from bulk to atomically thin layers, Applied sciences, 2016, 6: 264.

[36] X. Wang, L. Huang, X.-W. Jiang, Y. Li, Z. Wei, J. Li. Large scale ZrS2 atomically thin layers, Journal of Materials Chemistry C, 2016, 4: 3143.

[37] M. Zhang, Y. Zhu, X. Wang, Q. Feng, S. Qiao, W. Wen, Y. Chen, M. Cui, J. Zhang, C. Cai, et al.. Controlled synthesis of ZrS2 monolayer and few layers on hexagonal boron nitride, Journal of the American Chemical Society, 2015, 137: 7051.

[38] Y. Zhu, X. Wang, M. Zhang, C. Cai, L. Xie. Thickness and temperature dependent electrical properties of ZrS2 thin films directly grown on hexagonal boron nitride, Nano Research, 2016, 9: 2931.

[39] Y. Shimazu, Y. Fujisawa, K. Arai, T. Iwabuchi, and K. Suzuki, Synthesis and characterization of zirconium disulfide single crystals and thin-film transis-

 DOI: https://doi.org/10.30564/ssid.v1i2.1526

tors based on multilayer zirconium disulfide flakes, ChemNanoMat, 2018, 4: 1078.

[40] M. Mattinen, G. Popov, M. Vehkamaki, P. J. King, K. Mizohata, P. Jalkanen, J. Raisanen, M. Leskela, M. Ritala. Atomic layer deposition of emerging 2d semiconductors, HfS2 and ZrS2, for optoelectronics, Chemistry of Materials,2019, 31: 5713.

[41] X. Li, J. Carey, J. Sickler, M. Pralle, C. Palsule, C. Vineis, Silicon photodiodes with high photoconductive gain at room temperature, Optics Express, 2012, 20: 5518.

[42] R. K. Ulaganathan, Y. Y. Lu, C. J. Kuo, S. R. Tamalampudi, R. Sankar, K. M. Boopathi, A. Anand, K. Yadav, R. J. Mathew, C.-R. Liu, et al.. High photosensitivity and broad spectral response of multi-layered germanium sulfide transistors, Nanoscale, 2016, 8: 2284.

[43] N. Perea-Lopez, Z. Lin, N. R. Pradhan, A. Iniguez Rabago, A. L. Elıas, A. McCreary, J. Lou, P. M. Ajayan, H. Terrones, L. Balicas, et al., CVD-grown monolayered MoS2 as an effective photosensor operating at low- voltage, 2D Materials 1, 011004, 2014.

[44] X. Zhang, Z. Meng, D. Rao, Y. Wang, Q. Shi, Y. Liu, H. Wu, K. Deng, H. Liu, R. Lu. Efficient band structure tuning, charge separation, visible-light response in ZrS2-based Van der Waals heterostructures, Energy & Environmental Science, 2016, 9: 841.

[45] H. So, D. G. Senesky, ZnO nanorod arrays and direct wire bonding on GaN surfaces for rapid fabrication of antireflective, high-temperature ultraviolet sensors, Applied Surface Science, 2016, 387: 280.

[46] D. S. Tsai, W. C. Lien, D. H. Lien, K. M. Chen, M. L. Tsai, D. G. Senesky, Y. C. Yu, A. P. Pisano, J. H. He, Solar-blind photodetectors for harsh electronics, Scientific reports, 2013, 3: 2628.

[47] C. Lien, D. S. Tsai, S. H. Chiu, D. G. Senesky, R. Maboudian, A. P. Pisano, and J. H. He, Low temperature, ion beam-assisted sic thin films with antireflective ZnO nanorod arrays for high temperature photodetection, IEEE Electron Device Letters, 2011, 32, 1564.

[48] T. C. Wei, D. S. Tsai, P. Ravadgar, J. J. Ke, M. L. Tsai, D. H. Lien, C. Y. Huang, R. H. Horng, J. H. He. See-through Ga2O3 solar-blind photodetectors for use in harsh environments, IEEE Journal of Selected Topics in Quantum Electronics, 2014, 20: 112.

DOI: https://doi.org/10.30564/ssid.v1i2.1526

BILINGUAL PUBLISHING CO.
Pioneer of Global Academics Since 1984

Semiconductor Science and Information Devices
https://ojs.bilpublishing.com/index.php/ssid

ARTICLE

Infrastructure of Synchrotronic Biosensor Based on Semiconductor Device Fabrication for Tracking, Monitoring, Imaging, Measuring, Diagnosing and Detecting Cancer Cells

Alireza Heidari[1,2*]

1. Faculty of Chemistry, California South University, 14731 Comet St. Irvine, CA 92604, USA
2. American International Standards Institute, Irvine, CA 3800, USA

ARTICLE INFO

Article history
Received: 23 April 2020
Accepted: 11 May 2020
Published Online: 10 July 2020

Keywords:
Synchrotronic Biosensor
Copper Zinc Antimony Sulfide
CZAS (Cu1.18Zn0.40Sb1.90S7.2) Semiconductor
Photomultiplier
Semiconductor Device
Tracking
Monitoring
Imaging
Measuring
Diagnosing
Detecting
Cancer Cells
Tris(2,2'-bipyridyl) ruthenium(II)(Ru(bpy)32+)

ABSTRACT

Copper Zinc Antimony Sulfide (CZAS) is derived from Copper Antimony Sulfide (CAS), a famatinite class of compound. In the current paper, the first step for using Copper, Zinc, Antimony and Sulfide as materials in manufacturing synchrotronic biosensor-namely increasing the sensitivity of biosensor through creating Copper Zinc Antimony Sulfide, CZAS (Cu1.18Zn0.40Sb1.90S7.2) semiconductor and using it instead of Copper Tin Sulfide, CTS (Cu2SnS3) for tracking, monitoring, imaging, measuring, diagnosing and detecting cancer cells, is evaluated. Further, optimization of tris(2,2'-bipyridyl)ruthenium(II)(Ru(bpy)32+) concentrations and Copper Zinc Antimony Sulfide, CZAS (Cu1.18Zn0.40Sb1.90S7.2) semiconductor as two main and effective materials in the intensity of synchrotron for tracking, monitoring, imaging, measuring, diagnosing and detecting cancer cells are considered so that the highest sensitivity obtains. In this regard, various concentrations of two materials were prepared and photon emission was investigated in the absence of cancer cells. On the other hand, ccancer diagnosis requires the analysis of images and attributes as well as collecting many clinical and mammography variables. In diagnosis of cancer, it is important to determine whether a tumor is benign or malignant. The information about cancer risk prediction along with the type of tumor are crucial for patients and effective medical decision making. An ideal diagnostic system could effectively distinguish between benign and malignant cells; however, such a system has not been created yet. In this study, a model is developed to improve the prediction probability of cancer. It is necessary to have such a prediction model as the survival probability of cancer is high when patients are diagnosed at early stages.

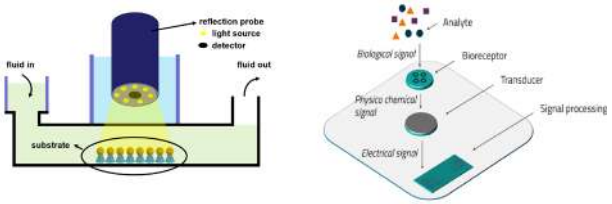

Schematic of infrastructure of synchrotronic biosensor based on semiconductor device fabrication for tracking, monitoring, imaging, measuring, diagnosing and detecting cancer cells

**Corresponding Author:*
Alireza Heidari,
Faculty of Chemistry, California South University, 14731 Comet St. Irvine, CA 92604, USA; American International Standards Institute, Irvine, CA 3800, USA;
Email: Scholar.Researcher.Scientist@gmail.com; Alireza.Heidari@calsu.us; Central@aisi-usa.org

 DOI: https://doi.org/10.30564/ssid.v1i2.1827

1. Introduction

Biosensors are systems for tracking, monitoring, imaging, measuring, diagnosing and detecting the concentration of cancer cells such as proteins, enzymes, nuclides and etc. which produce by various methods and materials depending on the type of biosensor and cancer cells. In optical method of synchrotron, a synchrotronic excites at the presence of activator agent due to applying electrical potential and hence, emits photon. in optical synchrotronic biosensor, the concentration of cancer cells can be measured using this method and stabilizing the synchrotron radiation on the cancer cells. In other words, cancer cells play the role of electrical potential carrier to synchrotron radiation. Hence, the applied potential to synchrotron radiation varies with concentration of cancer cells and therefore, the intensity of emitted photons varies [1-47]. The advantages of synchrotron method compared to other optical methods are (a) It does not necessary to have an excitation source which cause to reduction of optical interferences; (b) Having strong time and position separation power; (c) Simplicity, low cost, high speed and low time of measurement [48-92].

In the produced optical biosensor, as the first sample in the country, Copper Zinc Antimony Sulfide, CZAS (Cu1.18Zn0.40Sb1.90S7.2) semiconductor was used which is one of the most used synchrotron radiation, applied in manufacture of synchrotronic biosensors due to its high quantum efficiency and small size. Small size of Copper Zinc Antimony Sulfide, CZAS (Cu1.18Zn0.40Sb1.90S7.2) semiconductor leads to its easy conjugation with cancer cells which minimizes the interference in immune system of cancer cells [93-121]. In the produced optical sensor, Tris(2,2'-bipyridyl)ruthenium(II) (Ru(bpy)32+) is used as activator agent for Copper Zinc Antimony Sulfide, CZAS (Cu1.18Zn0.40Sb1.90S7.2) semiconductor.

One of the basic characteristics of biosensor is its high sensitivity. Sensitivity of a biosensor is the minimum amount of concentration detection of cancer cells. According to this definition, sensitivity of the produced biosensor increases proportional to increase in intensity of emitted photons from synchrotron radiation. Hence, Copper Zinc Antimony Sulfide, CZAS (Cu1.18Zn0.40Sb1.90S7.2) semiconductor was used for this reason.

Copper Zinc Antimony Sulfide, CZAS (Cu1.18Zn0.40Sb1.90S7.2) semiconductor nanoparticles enhance the intensity of photons due to some advantages. Two time-ionized CZAS nanoparticles easily coop Copper Zinc Antimony Sulfide, CZAS (Cu1.18Zn0.40Sb1.90S7.2) semiconductor ions due to having negative charge and enhance the optical stability of Copper Zinc Antimony Sulfide, CZAS (Cu1.18Zn0.40Sb1.90S7.2) semiconductor because of their optical property. At the other hand, as these molecules are of large active surface, they are able to charge (coop) a large amount of Copper Zinc Antimony Sulfide, CZAS (Cu1.18Zn0.40Sb1.90S7.2) semiconductor molecules. However, CZAS nanoparticles cannot individually stabilize on cancer cells such as antibodies and hence, Copper Zinc Antimony Sulfide, CZAS (Cu1.18Zn0.40Sb1.90S7.2) semiconductor nanoparticles are used to solve this problem [122-184].

The produced Copper Zinc Antimony Sulfide, CZAS (Cu1.18Zn0.40Sb1.90S7.2) semiconductor nanoparticles have negative charge on their surfaces due to the manufacture type and therefore, they can easily absorb functional groups with positive charge (such as amino groups). Many cancer cells are of functional groups with positive charge. To settle Copper Zinc Antimony Sulfide, CZAS (Cu1.18Zn0.40Sb1.90S7.2) semiconductor nanoparticles with negative charge on CZAS, layers with positive charge such as amino groups can be used. Due to small size of nanoparticles, a large number of them settle on CZAS (Figure 1). In addition, regarding the fact that Copper Zinc Antimony Sulfide, CZAS (Cu1.18Zn0.40Sb1.90S7.2) semiconductor nanoparticles are strong electric conductors, they enhance electron transferring process (electrical potential) to Copper Zinc Antimony Sulfide, CZAS (Cu1.18Zn0.40Sb1.90S7.2) semiconductor coop into ZCAS [185-217].

In this project we applied several machine learning techniques on the Wisconsin Diagnostic Breast Cancer data set to classify the cancer based on the feature extracted from images as benign or malignant [50-73].

In the current age, pancreatic cancer is one of the worst forms of cancer. The complications of pancreatic include five types of pancreatitis, benign tumors, malignant tumors, benign cysts and malignant cysts [1-27]. This cancer has a few clinical symptoms than other cancers. Also, if not treated in a timely manner, it also causes other organs of the body and the patient chance of survival is greatly reduced. One of the ways to detect this disease is to use CT scan images. But the appearance of pancreatic complications is very different in a similar category, and their tissue is very similar to healthy abdominal tissues [28-49]. For this reason, it's very difficult to identify the range of complications. In this study, the data contained 151CT scan images. These images are divided into five classes of pancreatitis, malignant tumors, benign tumors, malignant cysts, benign cysts and a healthy class. The pancreatic complications are varied and different, if the diagnostic system is based on simple experts; the possibility of

DOI: https://doi.org/10.30564/ssid.v1i2.1827

achieving high detection accuracy is not possible. According to the results of this study, lonely no classification can detect all diseases and combining these methods is the best option. Therefore, in this study we have achieved high accuracy in prediction (690. 69) by combining the perception, convolution and SVM neural networks.

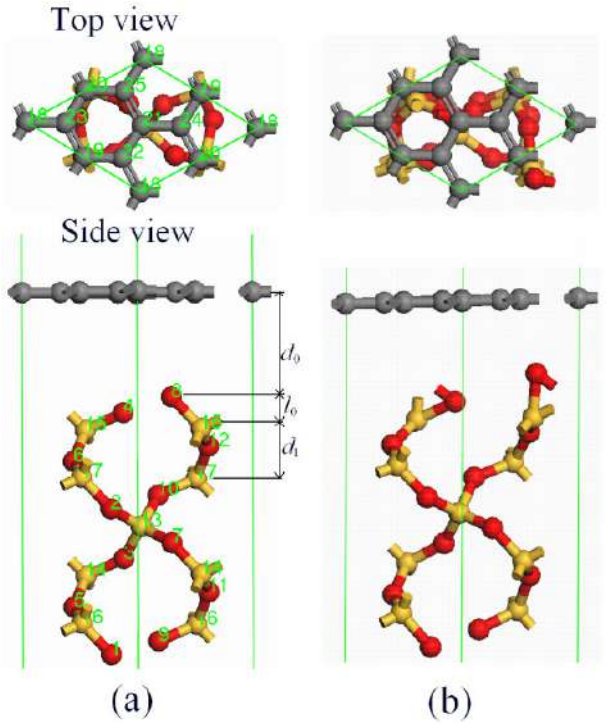

Figure 1. Schematic view of Copper Zinc Antimony Sulfide, CZAS (Cu1.18Zn0.40Sb1.90S7.2) semiconductor

In the current experimental work, in addition to sample preparation and manufacturing sensor device, the effect of semiconductor concentration also is investigated. As it is necessary to prevent any interference on the structure of Copper Zinc Antimony Sulfide, CZAS (Cu1.18Zn0.40Sb1.90S7.2) semiconductor, this issue is investigated in sample preparation and using them in electrochemical system [218-358].

2. Materials, Methods and Techniques

Polyurethane are biocompatible compounds with variety applications in the biomedical fields mostly as drug delivery vehicles. Their various applications are due to their Maneuverable structure with different blocks of diols and isocyanides. In the new presented work, magnetic polyurethane was used as drug carrier which formed of the reaction of Poly-caprolacton and isophoren diisocyanate and finally cyclodextrin as the cross linker. Characterization of the final polymer and certainty of its formation was done through different analytical methods such as FT-IR, TGA, XRD, SEM, TEM and VSM. On the other hand, the percentage of the magnetic nanoparticles in the polymer matrices was tracked using thermal gravimetery analysis. This Nano drug carrier was used for in vitro delivering pharmaceutical agent of doxorubicin. The amount of drug loading and percentage and manner of the drug release were investigated using concentration profile. Cytotoxicity of Nano drug carrier was evaluated using calorimetric method called methylthiazoletetrazolium (MTT) assay on the MCF-7 cell lines and according to the results presented system is very profitable and proper one for delivering Doxorubicin anti-cancer drug [74-93].

Melittin (MEL) is a kind of catalytic peptide that isolated from bee venom. Catalytic peptides are promising drugs for cancer treatment because cancer cells are less likely to develop resistance to a membrane-perturbing agent. However, their nonspecific cytotoxicity has limited their therapeutic applications. In this study, we use citric acid stabilized Fe3O4 magnetic nanoparticles (CA-MNP) as potential magnetic carriers for target delivery of melittin to tumor sites. The morphology and surface functionalization of these magnetic Nano carriers were studied by field emission scanning electron microscopy (FESEM) and Fourier transform infrared. The loading and release profile of MEL were studied by UV spectrophotometry. The results indicate that these magnetic Nano carriers have the high drug loading efficiency and the pH-dependent release behavior. The in vitro cytotoxicity of the MEL-loaded CA-MNP on the MCF-7 breast cancer cell line is similar to that of free MEL in solution at equivalent doses [94-104].

The interest in exploring more effective methods for cancer treatment has increased widely in recent years. In clinical studies it is difficult to determine the temperature distribution in both normal tissue and in tumor during hyperthermia treatment since temperature can be measured in limited number of positions in tissue or tumor. Simulation studies can play crucial role in physician's perception of the temperature distribution in tissue. Hyperthermia treatment is facing some unsolved problems such as the appropriate dosage of magnetic Nano particles required to achieve the optimum temperature which results in apoptosis in tumor cells. In this study, a 2D computational model is created in COMSOL Metaphysics in order to analyze temperature distribution in both normal tissue and tumor during hyperthermia treatment using various dosages of magnetic Nano particles. Temperature distribution is achieved by considering various layers from wave source through to the tumor and also by taking into account the amount of heat generated through the Brownian rotation and the Neel relaxation. Simulations of a spherical tumor located in ellipse tissue were designed. A systematical

 DOI: https://doi.org/10.30564/ssid.v1i2.1827

variation in dosage has been performed. Temperature distribution and maximum temperature in steady state and effect of the dosage of Nano particles [105-117].

In this study, cobalt Ferrite nanoparticles with inverse spinel structures were obtained using co-precipitation of cobalt and iron nitrates. Ammonia 15% was used as an alkaline agent for pH adjustment. Besides, we used oleic acid to coat the cobalt ferrite nanoparticles. XRD analysis showed that the samples included spinel ferrite structure. According to the results of SEM the distribution of the particles was homogeneous and the particles were uniform, and pseudo-spherical in shape. The magnetic properties of the material were analyzed by the VSM that showed the relationship between super-paramagnetic properties of the material and particle size. In this research, for the first time, anti-cancer effects of cobalt ferrite nanoparticles on K562 cell line as an experimental model of acute myeloid leukemia (CML) were examined. Because this compound has the potential to induce differentiation and apoptosis, it can be used in conjunction with other pharmaceutical compounds as a promising candidate for the treatment of blood cancer patients [118-143].

Cancer, as a leading contributor to the global disease burden is characterized by the uncontrolled growth of cells in the body, which makes it one of the most difficult and complex diseases to treat. Dietary sources of natural products including fruits and vegetables have been reported to be associated with reduced risk of a variety of tumors and to have anti-cancer benefits, apart from being a good source of nutrients. Thus, among major groups of anti-cancer drugs, plant extracts have received considerable attention to discover promising cancer therapeutic agents from natural sources. Great interest is currently centered on the biologic activities of quercetin a polyphenol belonging to the class of flavonoids, natural products well known for their beneficial effects on health, long before their biochemical characterization. onion skin waste is rich in bioactive compounds such as phenolic and flavonoids. In this direction, Quercetin, a natural compound abundantly present in Onion skin has great therapeutic potential in the prevention and treatment of cancer. This review focuses on anti-cancer potential of Quercetin with current advancements for its implementation in treatment of cancers [144-173].

Breast cancer is the uncontrolled growth of abnormal cells in the breast area and it is one of the widespread causes of mortality in today's world. So that 8000 people are diagnosed with breast cancer of a year in the world. The exact and precise diagnosis is considered as the vital point in the process of treatment. Among the various methods of screening, thermography is a non-invasive and safe method to detect breast cancer. In this work, a classification algorithm of thermograms with the purpose of detection of breast cancer from gray level co-occurrence matrix based features texture has been proposed. For this purpose, 52 images from the breast of healthy and unhealthy people from the data were collected. The preprocessing and segmentation of data was performed in gray level for the creation of temperature matrix. Finally, the gray level co-occurrence matrix based features was extracted from the matrix and the collection of features using Manhattan technique was the input for weighted K-nearest neighbor classifier. The result of Accuracy was 85.6, Sensitivity was 91.7 and Specificity Index was 81.2 selected as the optimal structure compared to other methods that have been proposed so far [190-203].

Cancer is the third leading cause of death in the world, as well as breast cancer is the second most common cause of death among women in the world. According to calculations by the National Cancer Institute of the United States, one person of every eight women will be diagnosed with breast cancer. Unfortunately, the age of cancer in the world is a decade younger than other developed countries. Therefore, early diagnosis of this disease is essential in the healing process. With detect and remove cancerous tumors in the early stages before spreading to neighboring areas, cancer threats be stopped. Among the various methods of screening, thermography is a non-invasive and safe method to detect breast cancer. In research, at first paid to the automatically way that in this regard, Kenny edge and Hough transform have been enjoying and then a thermography classification algorithm to detect breast cancer based on certain characteristics extraction of the tissue in gray level co-occurrence matrix is provided. For this purpose, 68 healthy and unhealthy images of the breast are collected from the database. Finally, the features set as input are given into the support vector machine classifier. The result of Accuracy was 87.3, Sensitivity was 89.6 and Specificity Index was 83.9 selected as the optimal structure compared to other methods that have been proposed so far [204-224].

Cancer caused by cells goes out of correct pathways. This cell can invade to surrounding healthy cells. There are over 100 different types of cancer and all of them classified by the type of cell that affected. Usually malignancy of gastric cancer starting from layer of the stomach. Gastric cancer has been mentioned as a third cause of death in the world. According to the statistical results, we can see the high frequency of gastric cancer in, Japan, China, Central and South America, Eastern Europe and parts of the middle east. Higher rates usually have been seen group with lower socioeconomic [225-241]. Some signs of this

DOI: https://doi.org/10.30564/ssid.v1i2.1827

cancer are indigestion or heartburn, vomiting, diarrhea, constipation and having blood in stool. Stomach cancer usually detects in early stage. Each factor that increase the chance of developing cancer is known as a risk factor. Some factors that may increase the risk of stomach cancer are: Age, gender, bacteria, family history, race, diet, previous surgery, smoke and obesity [242-266]. Diagnosis of gastric cancer at first are obtained from laboratory tests and biopsy of stomach with endoscopy. In the next step, cancer may be treated with Surgery, radiation therapy, chemotherapy or immunotherapy [267-284].

Lung cancer is one of the deadliest cancers, such that it causes more deaths compared to breast cancer, colon cancer and prostate cancer and it is mainly because it cannot be diagnosed at early stages due to shortage of symptoms, such that survival rate of patients for 5 years after surgery is only 14%; while diagnosing the disease at early stages increases this probability to 70%. Increasing growth of this disease, difficulty of its diagnosis from images and importance of diagnosis at early stages requires CAD methods with high accuracy. In order to realize this important, a novel algorithm is proposed in this study which selects features online using genetic algorithm and statistical functions. Our purpose is to separate effective features among available features. In order to classify data, a series of data called feature is required for which disease features are used. In many datasets, some features do not affect decisions and they are additional. So selecting an appropriate subset of inputs can be effective in classification accuracy and its speed. For this purpose, genetic algorithm with an objective function based on data sparsity and statistical concepts. The proposed method is implemented and results indicate high accuracy of this algorithm in selecting effective features and increasing accuracy of the classifier compared to basic methods and other studies [285-299].

Cancer is a major cause of death with more than 10 million annual patients. It is possible that this number reaches 15 million patients per year by 2020. Though chemotherapy has largely been successful in controlling and treating cancer, live tissue damage, systemic toxicity and side effects in this method are among the issues that cannot be overlooked. In order to reduce the negative effects of anticancer drugs on normal tissues, we need to design Nano-sized carriers that can pass the safety barriers and body tissues and reach their target site. In this work, the size and zeta potential of Nano-carriers PLGA-Cs-Paclitaxel were evaluated. Chitosan connection in physical or conjugated forms may lead to a significant increase of polydispersity. According to the study carried out on the concentration of Chitosan and the type of absorption, it was concluded that nanoparticles size increases with higher concentrations of Chitosan. The zeta potential will increase, provided the conjugation of Chitosan is higher than physical adsorption [300-311].

Cancer stem cells (CSCs) are rare sub-population of tumor with ability to differentiate and self-renew. Some properties of CSCs such as increased ability to repair damaged DNA/RNA, as well as increased expression of transporters responsible for drug efflux make them main agents for resistance to chemotherapy. In colon cancer, FOLFOX is a common therapy. In this study, we have analyzed the effects of FOLFOX on CSCs population of colon cancer cell line. Results show that in addition to a dose-dependent reduction in cell viability, FOLFOX caused a decrease in SP cells relative to untreated controls [344-358].

For the detection of DNA/RNA hybridization, a new electrochemical biosensor was developed on the basis of the interaction of Doxirubicine (DOX) with 22-mer oligonucleotides (from human cancer) a simple bio sensing design to yield an ultrasensitive electrochemical biosensor for cancer biomarker detection on Screen Printed Gold Electrodes (SPGE) without use of any modification on electrode surface perhaps direct detection with the help of electroactive label (DOX) and MicroRNA92a (miRNA) as an biomarker selected for being up-regulated in cancer. The biosensor was assembled in two stages the immobilization of the probe that was modified on an SPGE and second stage of target hybridization of completely match strand electroactive label DOX has been used after hybridization process which is an intercalator with our miRNA strands as a redox indicator for amplifying the electrochemical signal of miRNA 92a. For conformation electrochemical techniques including Cyclic Voltammetry (CV) and Differential Pulse Voltammetry (DPV). were used and hybridization was observed successfully. The final biosensor provided a sensitive detection of miRNA 92a with good selectivity.

Based on the researches, one of the most common cancer among the men is malignant cancer. Which seen after surgery and gland removing completely the amount of PSA in patient increases again and available drugs which have severe side effects cannot effect on rising the PSA. One parameter that without it cancer cells are not able to reproduce is Glutamine Amino Acid. With studying humanity biochemical pathway and Glutamine Amino Acid reabsorbing pathways by cancer cells we understand that two material Ursolic Acid and Resveratrol could dock with a lots of Allosteric Enzymes inside the reabsorbing pathway Glutamine Amino Acid by cancer cells. That inactive enzymes therefore more than 90 % reabsorbing

 DOI: https://doi.org/10.30564/ssid.v1i2.1827

pathways Glutamine Amino Acid will be closed. Docking these two materials Ursolic Acid and Resveratrol with Allosteric enzymes reabsorbing pathways Glutamine Amino Acid by cancer cells and inactivating enzymes with software Autodock-vina and QSAR has been checked. Also Curcumin could stimulate Apoptosis in cancer cells. Since three above substances (Resveratrol, Curcumin, Ursolic acid) exist in available compounds like skin of red apple, turmeric and black grapes, men above forty years old can reduce risk of cancer by combining a big apple with some turmeric and black grapes (as a potion or juice). So it can protect from cancer. After prostate surgery, PSA may raise again. Consumption of this potion in these cases can replace current medications with several adverse effects. Since we could find Ursolic Acid in red apple skin and Resveratrol in black grape and Curcumin in Turmeric, we could extraction and combine these three material and with determining the amount of doze make a medicine. Then doing the next steps like animal test, toxic test and human test. Base on human gene plan (HGP) and humanity biochemical pathway lack of Allosteric enzymes which by two material Ursolic Acid and Resveratrol will be inactivate and therefore non-proliferation cancer cells.

Chemotherapy resistance of cancers have become a big challenge in modern medicine. Recently, in order to overcome the drug resistance issue, producing novel drug which used with previous ones as multidrug treatment became an alternative. One of the compounds that have drawn much attention in this regard is chromenes. Chromenes have a heterocyclic structure with gamma benzopyrone, and anti-cancer activities. Studies tried to produce new derivative of chromenes which have better effect on cancer therapy. In this investigation we produced four novel derivatives of chromenes and studied the effect of these compounds on the human acute lymphoblastic leukemia cell line ofMOLT4. A series of novel 4-hydroxycoumarinhas been synthesized via multi-step protocol. The structure of the new compound was established using spectroscopic method (H-NMR, C-NMR). MOLT4cells were cultured in RPMI medium with 10% fetal bovine serum. The cytotoxic effect of different concentrations (0, 50, 250, 500 and 1000 nM) of novel synthetic compounds were evaluated by the MTT assay and cell counting after different incubation times (24, 48, 72 h). These compounds decreased viability of the MOLT4 cells in a time- and dose-dependent manner. Notably, meaningful differences were found between all concentrations and control groups. However, C2 had fewer IC50 in comparison to other ones. Interestingly, this derivative showed significantly cell toxicity at the concentration of Nano-Molar, while previously reported ones have cell toxicity at micro-Molar concentrations. Dihydrochromeno (3, 4-b) chromenes have anti-neoplastic effects on MOLT4 by inducing of apoptosis. Further studies are needed to find exact mechanisms of its effect.

3. Results and Discussion

In order to recognize the size of produced Copper Zinc Antimony Sulfide, CZAS (Cu1.18Zn0.40Sb1.90S7.2) semiconductor nanoparticles, SEM imaging was used. Figure (2) shows a sample of SEM image produced from Copper Zinc Antimony Sulfide, CZAS (Cu1.18Zn0.40Sb1.90S7.2) semiconductor nanoparticles. In this regard, the average size of these particles is between 15-20 (nm).

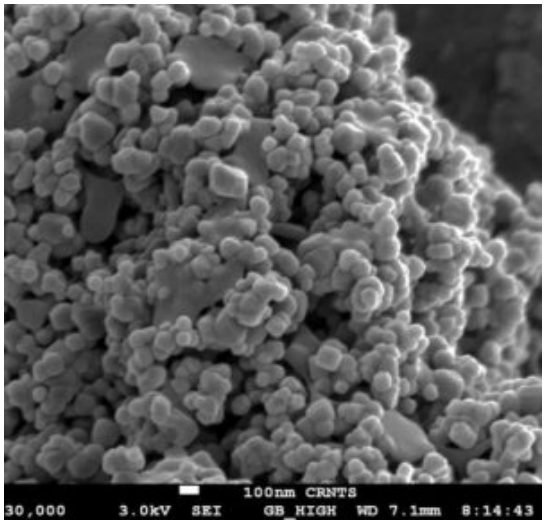

Figure 2. SEM image for the produced Copper Zinc Antimony Sulfide, CZAS (Cu1.18Zn0.40Sb1.90S7.2) semiconductor nanoparticles

Figures 3a and 3b show SEM images for Cu-Zn and Cu-Zn-Sb, respectively. Size of these nanoparticles is about 50 (nm). By comparing the obtained sizes, it was indicated that Cu-Zn nanoparticles are able to load a large number of Cu-Zn-Sb nanoparticles.

Figure 4 shows attenuated total reflectance-Fourier transform infrared (ATR-FTIR) spectra of Cu, Cu-Zn and Cu-Zn-Sb semiconductor. Comparison of absorptive curves indicate 5 (nm) shift of wavelength in the spectrum of Cu-Zn at 450 (nm) which confirms cooping of Copper Zinc Antimony Sulfide, CZAS (Cu1.18Zn0.40Sb1.90S7.2) semiconductor into Cu-Zn-Sb. In addition, according to emission curve, semiconductor manufacture does not change the emitted spectrum of Cu and its synchrotron nature and increasing the emission intensity of semiconductor indicates copping a large number of Copper Zinc Antimony Sulfide, CZAS (Cu1.18Zn0.40Sb1.90S7.2) semiconductor molecules.

DOI: https://doi.org/10.30564/ssid.v1i2.1827

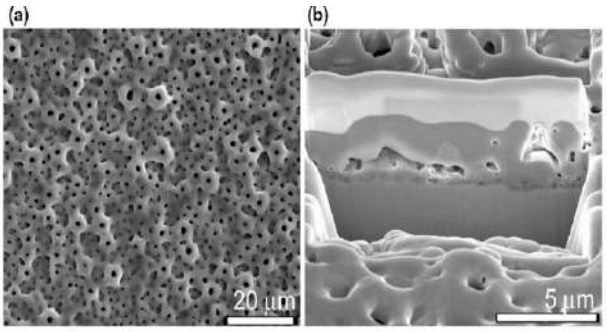

Figure 3. SEM images for (a) Cu-Zn and (b) Cu-Zn-Sb, respectively

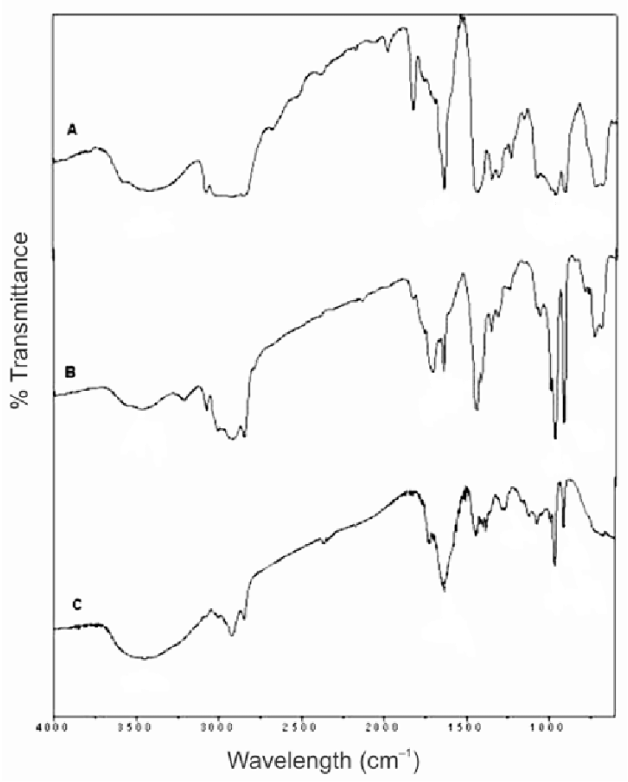

Figure 4. Comparative attenuated total reflectance-Fourier transform infrared (ATR-FTIR) spectra for (a) Cu, (b) Cu-Zn and (c) Cu-Zn-Sb (photo shows vibrational spectra for (a) Cu, (b) Cu-Zn and (c) Cu-Zn-Sb)

As ray emitted from samples is used to affect cancer cells, its amount was measured through selecting optimum concentration of semiconductor on the produced samples and concentration of required Tris(2,2'-bipyridyl)ruthenium(II) (Ru(bpy)32+) solvent before applying synchrotron on cancer cells. In this regard, the intensity of synchrotron of samples in solvents with various concentrations were measured to find optimum concentration of semiconductor in the produced samples for a constant concentration of solvent, as shown in Figure (5). From this test, optimum amount of Copper Zinc Antimony Sulfide, CZAS (Cu1.18Zn0.40Sb1.90S7.2) semiconductor semiconductor was determined as 2 (mg/ml) and then, samples with optimum concentration of semiconductor were tested at different concentrations of Tris(2,2'-bipyridyl)ruthenium(II) (Ru(bpy)32+) solvent and again, optimum synchrotron was obtained as 20 (mM). Figure (6) indicates this optimum amount.

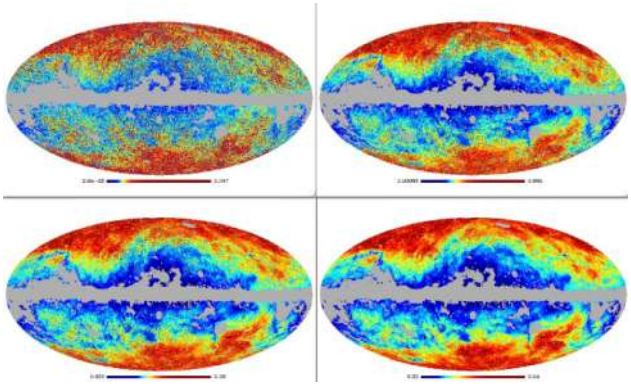

Figure 5. Photon emission for various concentrations of semiconductor (Figure: Optimization graphs of concentration of Copper Zinc Antimony Sulfide, CZAS (Cu1.18Zn0.40Sb1.90S7.2) semiconductor semiconductor)

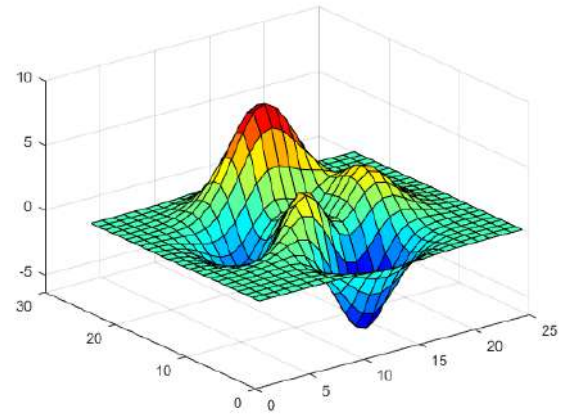

Figure 6. Photon emission for various concentrations of Tris(2,2'-bipyridyl)ruthenium(II) (Ru(bpy)32+) (Figure: Optimization graph of concentration of Tris(2,2'-bipyridyl)ruthenium(II) (Ru(bpy)32+))

4. Conclusions, Summary, Perspectives, Useful Suggestions and Future Studies

As the manufacture of synchrotronic biosensor is performed for the first time in the country, it was necessary to provide appropriate conditions such as high sensitivity and optimizing the effective factors in tracking, monitoring, imaging, measuring, diagnosing and detecting cancer

 DOI: https://doi.org/10.30564/ssid.v1i2.1827

cells before any measurement. Lack of these conditions will lead to loss of cancer cells. Cancer is a major cause of death with more than 10 million annual patients. It is possible that this number reaches 15 million patients per year by 2020. Though chemotherapy has largely been successful in controlling and treating cancer, live tissue damage, systemic toxicity and side effects in this method are among the issues that cannot be overlooked. In order to reduce the negative effects of anticancer drugs on normal tissues, we need to design Nano-sized carriers that can pass the safety barriers and body tissues and reach their target site. In this research, the size and zeta potential of Nano-carriers PLGA-Cs-Paclitaxel were evaluated. Chitosan connection in physical or conjugated forms may lead to a significant increase of polydispersity. According to the study carried out on the concentration of Chitosan and the type of absorption, it was concluded that nanoparticles size increases with higher concentrations of Chitosan. The zeta potential will increase, provided the conjugation of Chitosan is higher than physical adsorption.

References

[1] A. Heidari, C. Brown. Study of Composition and Morphology of Cadmium Oxide (CdO) Nanoparticles for Eliminating Cancer Cells. J Nanomed Res., 2015, 2(5): 20.

[2] A. Heidari, C. Brown. Study of Surface Morphological, Phytochemical and Structural Characteristics of Rhodium (III) Oxide (Rh2O3) Nanoparticles. International Journal of Pharmacology, Phytochemistry and Ethnomedicine, 2015, 1(1): 15-19.

[3] A. Heidari. An Experimental Biospectroscopic Study on Seminal Plasma in Determination of Semen Quality for Evaluation of Male Infertility. Int J Adv Technol., 2016, 7: e007.

[4] A. Heidari. Extraction and Preconcentration of N-Tolyl-Sulfonyl-Phosphoramid-Saeure-Dichlorid as an Anti-Cancer Drug from Plants: A Pharmacognosy Study. J Pharmacogn Nat Prod., , 2016, 2: e103.

[5] A. Heidari. A Thermodynamic Study on Hydration and Dehydration of DNA and RNA−Amphiphile Complexes. J Bioeng Biomed Sci., S, 2016: 006.

[6] A. Heidari. Computational Studies on Molecular Structures and Carbonyl and Ketene Groups' Effects of Singlet and Triplet Energies of Azidoketene O=C=CH-NNN and Isocyanatoketene O=C=CH-N=C=O. J Appl Computat Math, 2016, 5: e142.

[7] A. Heidari. Study of Irradiations to Enhance the Induces the Dissociation of Hydrogen Bonds between Peptide Chains and Transition from Helix Structure to Random Coil Structure Using ATR-FTIR, Raman and 1HNMR Spectroscopies. J Biomol Res Ther., 2016, 5: e146.

[8] A. Heidari. Future Prospects of Point Fluorescence Spectroscopy, Fluorescence Imaging and Fluorescence Endoscopy in Photodynamic Therapy (PDT) for Cancer Cells. J Bioanal Biomed, 2016, 8: e135.

[9] A. Heidari. A Bio-Spectroscopic Study of DNA Density and Color Role as Determining Factor for Absorbed Irradiation in Cancer Cells. Adv Cancer Prev.,, 2016, 1: e102.

[10] A. Heidari. Manufacturing Process of Solar Cells Using Cadmium Oxide (CdO) and Rhodium (III) Oxide (Rh2O3) Nanoparticles. J Biotechnol Biomater, 2016, 6: e125.

[11] A. Heidari. A Novel Experimental and Computational Approach to Photobiosimulation of Telomeric DNA/RNA: A Biospectroscopic and Photobiological Study. J Res Development, 2016, 4: 144.

[12] A. Heidari. Biochemical and Pharmacodynamical Study of Microporous Molecularly Imprinted Polymer Selective for Vancomycin, Teicoplanin, Oritavancin, Telavancin and Dalbavancin Binding. Biochem Physiol., 2016, 5: e146.

[13] A. Heidari. Anti-Cancer Effect of UV Irradiation at Presence of Cadmium Oxide (CdO) Nanoparticles on DNA of Cancer Cells: A Photodynamic Therapy Study. Arch Cancer Res., 2016, 4: 1.

[14] A. Heidari. Biospectroscopic Study on Multi-Component Reactions (MCRs) in Two A-Type and B-Type Conformations of Nucleic Acids to Determine Ligand Binding Modes, Binding Constant and Stability of Nucleic Acids in Cadmium Oxide (CdO) Nanoparticles-Nucleic Acids Complexes as Anti-Cancer Drugs. Arch Cancer Res., 2016, 4: 2.

[15] A. Heidari. Simulation of Temperature Distribution of DNA/RNA of Human Cancer Cells Using Time-Dependent Bio-Heat Equation and Nd: YAG Lasers. Arch Cancer Res., 2016, 4: 2.

[16] A. Heidari. Quantitative Structure-Activity Relationship (QSAR) Approximation for Cadmium Oxide (CdO) and Rhodium (III) Oxide (Rh2O3) Nanoparticles as Anti-Cancer Drugs for the Catalytic Formation of Proviral DNA from Viral RNA Using Multiple Linear and Non-Linear Correlation Approach. Ann Clin Lab Res., 2016, 4: 1.

[17] A. Heidari. Biomedical Study of Cancer Cells DNA Therapy Using Laser Irradiations at Presence of Intelligent Nanoparticles. J Biomedical Sci., 2016, 5: 2.

[18] A. Heidari. Measurement the Amount of Vitamin D2 (Ergocalciferol), Vitamin D3 (Cholecalciferol) and Absorbable Calcium (Ca2+), Iron (II) (Fe2+), Magnesium (Mg2+), Phosphate (PO4-) and Zinc (Zn2+)

DOI: https://doi.org/10.30564/ssid.v1i2.1827

in Apricot Using High-Performance Liquid Chromatography (HPLC) and Spectroscopic Techniques. J Biom Biostat, 2016, 7: 292.

[19] A. Heidari. Spectroscopy and Quantum Mechanics of the Helium Dimer (He2+), Neon Dimer (Ne2+), Argon Dimer (Ar2+), Krypton Dimer (Kr2+), Xenon Dimer (Xe2+), Radon Dimer(Rn2+) and Ununoctium Dimer (Uuo2+) Molecular Cations. Chem Sci J, 2016, 7: e112.

[20] A. Heidari. Human Toxicity Photodynamic Therapy Studies on DNA/RNA Complexes as a Promising New Sensitizer for the Treatment of Malignant Tumors Using Bio-Spectroscopic Techniques. J Drug Metab Toxicol, 2016, 7: e129.

[21] A. Heidari. Novel and Stable Modifications of Intelligent Cadmium Oxide (CdO) Nanoparticles as Anti-Cancer Drug in Formation of Nucleic Acids Complexes for Human Cancer Cells' Treatment. Biochem Pharmacol (Los Angel), 2016, 5: 207.

[22] A. Heidari. A Combined Computational and QM/MM Molecular Dynamics Study on Boron Nitride Nanotubes (BNNTs), Amorphous Boron Nitride Nanotubes (a-BNNTs) and Hexagonal Boron Nitride Nanotubes (h-BNNTs) as Hydrogen Storage. Struct Chem Crystallogr Commun, 2016, 2: 1.

[23] A. Heidari. Pharmaceutical and Analytical Chemistry Study of Cadmium Oxide (CdO) Nanoparticles Synthesis Methods and Properties as Anti-Cancer Drug and its Effect on Human Cancer Cells. Pharm Anal Chem Open Access, 2016, 2: 113.

[24] A. Heidari. A Chemotherapeutic and Biospectroscopic Investigation of the Interaction of Double-Standard DNA/RNA-Binding Molecules with Cadmium Oxide (CdO) and Rhodium (III) Oxide (Rh2O3) Nanoparticles as Anti-Cancer Drugs for Cancer Cells' Treatment. Chemo Open Access, 2016, 5: e129.

[25] A. Heidari. Pharmacokinetics and Experimental Therapeutic Study of DNA and Other Biomolecules Using Lasers: Advantages and Applications. J Pharmacokinet Exp Ther 1: e005.

[26] A. Heidari. Determination of Ratio and Stability Constant of DNA/RNA in Human Cancer Cells and Cadmium Oxide (CdO) Nanoparticles Complexes Using Analytical Electrochemical and Spectroscopic Techniques. Insights Anal Electrochem, 2016, 2: 1.

[27] A. Heidari. Discriminate between Antibacterial and Non-Antibacterial Drugs Artificial Neutral Networks of a Multilayer Perceptron (MLP) Type Using a Set of Topological Descriptors. J Heavy Met Toxicity Dis., 2016, 1: 2.

[28] A. Heidari. Combined Theoretical and Computational Study of the Belousov-Zhabotinsky Chaotic Reaction and Curtius Rearrangement for Synthesis of Mechlorethamine, Cisplatin, Streptozotocin, Cyclophosphamide, Melphalan, Busulphan and BCNU as Anti-Cancer Drugs. Insights Med Phys., 2016, 1: 2.

[29] A. Heidari. A Translational Biomedical Approach to Structural Arrangement of Amino Acids' Complexes: A Combined Theoretical and Computational Study. Transl Biomed., 2016, 7: 2.

[30] A. Heidari. Ab Initio and Density Functional Theory (DFT) Studies of Dynamic NMR Shielding Tensors and Vibrational Frequencies of DNA/RNA and Cadmium Oxide (CdO) Nanoparticles Complexes in Human Cancer Cells. J Nanomedine Biotherapeutic Discov., 2016, 6: e144.

[31] A. Heidari. Molecular Dynamics and Monte-Carlo Simulations for Replacement Sugars in Insulin Resistance, Obesity, LDL Cholesterol, Triglycerides, Metabolic Syndrome, Type 2 Diabetes and Cardiovascular Disease: A Glycobiological Study. J Glycobiol., 2016, 5: e111.

[32] A. Heidari. Synthesis and Study of 5-[(Phenylsulfonyl)Amino]-1,3,4-Thiadiazole-2-Sulfonamide as Potential Anti-Pertussis Drug Using Chromatography and Spectroscopy Techniques. Transl Med (Sunnyvale), 2016, 6: e138.

[33] A. Heidari. Nitrogen, Oxygen, Phosphorus and Sulphur Heterocyclic Anti-Cancer Nano Drugs Separation in the Supercritical Fluid of Ozone (O3) Using Soave-Redlich-Kwong (SRK) and Pang-Robinson (PR) Equations. Electronic J Biol., 2016, 12: 4.

[34] A. Heidari. An Analytical and Computational Infrared Spectroscopic Review of Vibrational Modes in Nucleic Acids. Austin J Anal Pharm Chem., 2016, 3(1): 1058.

[35] A. Heidari, C. Brown. Phase, Composition and Morphology Study and Analysis of Os-Pd/HfC Nanocomposites. Nano Res Appl., 2016, 2: 1.

[36] A. Heidari, C. Brown. Vibrational Spectroscopic Study of Intensities and Shifts of Symmetric Vibration Modes of Ozone Diluted by Cumene. International Journal of Advanced Chemistry, 2016, 4(1): 5-9.

[37] A. Heidari. Study of the Role of Anti-Cancer Molecules with Different Sizes for Decreasing Corresponding Bulk Tumor Multiple Organs or Tissues. Arch Can Res., 2016, 4: 2.

[38] A. Heidari. Genomics and Proteomics Studies of Zolpidem, Necopidem, Alpidem, Saripidem, Miroprofen, Zolimidine, Olprinone and Abafungin as Anti-Tumor, Peptide Antibiotics, Antiviral and Central Nervous System (CNS) Drugs. J Data Mining Genomics & Proteomics, 2016, 7: e125.

 DOI: https://doi.org/10.30564/ssid.v1i2.1827

[39] A. Heidari. Pharmacogenomics and Pharmacoproteomics Studies of Phosphodiesterase-5 (PDE5) Inhibitors and Paclitaxel Albumin-Stabilized Nanoparticles as Sandwiched Anti-Cancer Nano Drugs between Two DNA/RNA Molecules of Human Cancer Cells. J Pharmacogenomics Pharmacoproteomics, 2016, 7: e153.

[40] A. Heidari. Biotranslational Medical and Biospectroscopic Studies of Cadmium Oxide (CdO) Nanoparticles-DNA/RNA Straight and Cycle Chain Complexes as Potent Anti-Viral, Anti-Tumor and Anti-Microbial Drugs: A Clinical Approach. Transl Biomed. 7: 2, 2016.

[41] A. Heidari. A Comparative Study on Simultaneous Determination and Separation of Adsorbed Cadmium Oxide (CdO) Nanoparticles on DNA/RNA of Human Cancer Cells Using Biospectroscopic Techniques and Dielectrophoresis (DEP) Method. Arch Can Res., 2016, 4: 2.

[42] A. Heidari. Cheminformatics and System Chemistry of Cisplatin, Carboplatin, Nedaplatin, Oxaliplatin, Heptaplatin and Lobaplatin as Anti-Cancer Nano Drugs: A Combined Computational and Experimental Study. J Inform Data Min., 2016, 1: 3.

[43] A. Heidari. Linear and Non-Linear Quantitative Structure-Anti-Cancer-Activity Relationship (QSACAR) Study of Hydrous Ruthenium (IV) Oxide (RuO2) Nanoparticles as Non-Nucleoside Reverse Transcriptase Inhibitors (NNRTIs) and Anti-Cancer Nano Drugs. J Integr Oncol., 2016, 5: e110.

[44] A. Heidari. Synthesis, Characterization and Biospectroscopic Studies of Cadmium Oxide (CdO) Nanoparticles-Nucleic Acids Complexes Absence of Soluble Polymer as a Protective Agent Using Nucleic Acids Condensation and Solution Reduction Method. J Nanosci Curr Res., 2016, 1: e101.

[45] A. Heidari. Coplanarity and Collinearity of 4'-Dinonyl-2,2'-Bithiazole in One Domain of Bleomycin and Pingyangmycin to be Responsible for Binding of Cadmium Oxide (CdO) Nanoparticles to DNA/RNA Bidentate Ligands as Anti-Tumor Nano Drug. Int J Drug Dev & Res., 2016, 8: 007-008.

[46] A. Heidari. A Pharmacovigilance Study on Linear and Non-Linear Quantitative Structure (Chromatographic) Retention Relationships (QSRR) Models for the Prediction of Retention Time of Anti-Cancer Nano Drugs under Synchrotron Radiations. J Pharmacovigil, 2016, 4: e161.

[47] A. Heidari. Nanotechnology in Preparation of Semipermeable Polymers. J Adv Chem Eng., 2016, 6: 157.

[48] A. Heidari. A Gastrointestinal Study on Linear and Non-Linear Quantitative Structure (Chromatographic) Retention Relationships (QSRR) Models for Analysis 5-Aminosalicylates Nano Particles as Digestive System Nano Drugs under Synchrotron Radiations. J Gastrointest Dig Syst., 2016, 6: e119.

[49] A. Heidari. DNA/RNA Fragmentation and Cytolysis in Human Cancer Cells Treated with Diphthamide Nano Particles Derivatives. Biomedical Data Mining, 2016, 5: e102.

[50] A. Heidari. A Successful Strategy for the Prediction of Solubility in the Construction of Quantitative Structure-Activity Relationship (QSAR) and Quantitative Structure-Property Relationship (QSPR) under Synchrotron Radiations Using Genetic Function Approximation (GFA) Algorithm. J Mol Biol Biotechnol, 2016, 1: 1.

[51] A. Heidari. Computational Study on Molecular Structures of C20, C60, C240, C540, C960, C2160 and C3840 Fullerene Nano Molecules under Synchrotron Radiations Using Fuzzy Logic", J Material Sci Eng., 2016, 5: 282.

[52] A. Heidari. Graph Theoretical Analysis of Zigzag Polyhexamethylene Biguanide, Polyhexamethylene Adipamide, Polyhexamethylene Biguanide Gauze and Polyhexamethylene Biguanide Hydrochloride (PHMB) Boron Nitride Nanotubes (BNNTs), Amorphous Boron Nitride Nanotubes (a-BNNTs) and Hexagonal Boron Nitride Nanotubes (h-BNNTs). J Appl Computat Math, 2016, 5: e143.

[53] A. Heidari. The Impact of High Resolution Imaging on Diagnosis. Int J Clin Med Imaging, 2016, 3: 1000e101.

[54] A. Heidari. A Comparative Study of Conformational Behavior of Isotretinoin (13-Cis Retinoic Acid) and Tretinoin (All-Trans Retinoic Acid (ATRA)) Nano Particles as Anti-Cancer Nano Drugs under Synchrotron Radiations Using Hartree-Fock (HF) and Density Functional Theory (DFT) Methods. Insights in Biomed, 2016, 1: 2.

[55] A. Heidari. Advances in Logic, Operations and Computational Mathematics. J Appl Computat Math, 2016, 5: 5.

[56] A. Heidari. Mathematical Equations in Predicting Physical Behavior. J Appl Computat Math, 2016, 5: 5.

[57] A. Heidari. Chemotherapy a Last Resort for Cancer Treatment. Chemo Open Access, 2016, 5: 4.

[58] A. Heidari. Separation and Pre-Concentration of Metal Cations-DNA/RNA Chelates Using Molecular Beam Mass Spectrometry with Tunable Vacuum Ultraviolet (VUV) Synchrotron Radiation and Various Analytical Methods. Mass Spectrom Purif Tech., 2016, 2: e101.

DOI: https://doi.org/10.30564/ssid.v1i2.1827

[59] A. Heidari. Yoctosecond Quantitative Structure-Activity Relationship (QSAR) and Quantitative Structure-Property Relationship (QSPR) under Synchrotron Radiations Studies for Prediction of Solubility of Anti-Cancer Nano Drugs in Aqueous Solutions Using Genetic Function Approximation (GFA) Algorithm. Insight Pharm Res., 2016, 1: 1.

[60] A. Heidari. Cancer Risk Prediction and Assessment in Human Cells under Synchrotron Radiations Using Quantitative Structure Activity Relationship (QSAR) and Quantitative Structure Properties Relationship (QSPR) Studies. Int J Clin Med Imaging, 2016, 3: 516.

[61] A. Heidari. A Novel Approach to Biology. Electronic J Biol., 2016, 12: 4.

[62] A. Heidari. Innovative Biomedical Equipment's for Diagnosis and Treatment. J Bioengineer & Biomedical Sci., 2016, 6: 2.

[63] A. Heidari. Integrating Precision Cancer Medicine into Healthcare, Medicare Reimbursement Changes and the Practice of Oncology: Trends in Oncology Medicine and Practices. J Oncol Med & Pract, 2016, 1: 2.

[64] A. Heidari. Promoting Convergence in Biomedical and Biomaterials Sciences and Silk Proteins for Biomedical and Biomaterials Applications: An Introduction to Materials in Medicine and Bioengineering Perspectives. J Bioengineer & Biomedical Sci., 2016, 6: 3.

[65] A. Heidari. X-Ray Fluorescence and X-Ray Diffraction Analysis on Discrete Element Modeling of Nano Powder Metallurgy Processes in Optimal Container Design. J Powder Metall Min., 2017, 6: 1.

[66] A. Heidari. Biomolecular Spectroscopy and Dynamics of Nano-Sized Molecules and Clusters as Cross-Linking-Induced Anti-Cancer and Immune-Oncology Nano Drugs Delivery in DNA/RNA of Human Cancer Cells' Membranes under Synchrotron Radiations: A Payload-Based Perspective. Arch Chem Res., 2017, 1: 2.

[67] A. Heidari. Deficiencies in Repair of Double-Standard DNA/RNA-Binding Molecules Identified in Many Types of Solid and Liquid Tumors Oncology in Human Body for Advancing Cancer Immunotherapy Using Computer Simulations and Data Analysis: Number of Mutations in a Synchronous Tumor Varies by Age and Type of Synchronous Cancer. J Appl Bioinforma Comput Biol, 2017, 6: 1.

[68] A. Heidari. Electronic Coupling among the Five Nanomolecules Shuts Down Quantum Tunneling in the Presence and Absence of an Applied Magnetic Field for Indication of the Dimer or other Provide Different Influences on the Magnetic Behavior of Single Molecular Magnets (SMMs) as Qubits for Quantum Computing. Glob J Res Rev., 2017, 4: 2.

[69] A. Heidari. Polymorphism in Nano-Sized Graphene Ligand-Induced Transformation of Au38-xAgx/xCux(SPh-tBu)24 to Au36-xAgx/xCux-(SPh-tBu)24 (x = 1-12) Nanomolecules for Synthesis of Au144-xAgx/xCux[(SR)60, (SC4)60, (SC6)60, (SC12)60, (PET)60, (p-MBA)60, (F)60, (Cl)60, (Br)60, (I)60, (At)60, (Uus)60 and (SC6H13)60] Nano Clusters as Anti-Cancer Nano Drugs. J Nanomater Mol Nanotechnol, 2017, 6: 3.

[70] A. Heidari. Biomedical Resource Oncology and Data Mining to Enable Resource Discovery in Medical, Medicinal, Clinical, Pharmaceutical, Chemical and Translational Research and Their Applications in Cancer Research. Int J Biomed Data Min., 2017, 6: e103.

[71] A. Heidari. Study of Synthesis, Pharmacokinetics, Pharmacodynamics, Dosing, Stability, Safety and Efficacy of Olympiadane Nanomolecules as Agent for Cancer Enzymotherapy, Immunotherapy, Chemotherapy, Radiotherapy, Hormone Therapy and Targeted Therapy under Synchrotorn Radiation. J Dev Drugs, 2017, 6: e154.

[72] A. Heidari. A Novel Approach to Future Horizon of Top Seven Biomedical Research Topics to Watch in 2017: Alzheimer's, Ebola, Hypersomnia, Human Immunodeficiency Virus (HIV), Tuberculosis (TB), Microbiome/Antibiotic Resistance and Endovascular Stroke. J Bioengineer & Biomedical Sci., 2017, 7: e127.

[73] A. Heidari. Opinion on Computational Fluid Dynamics (CFD) Technique. Fluid Mech Open Acc., 2017, 4: 157.

[74] A. Heidari. Concurrent Diagnosis of Oncology Influence Outcomes in Emergency General Surgery for Colorectal Cancer and Multiple Sclerosis (MS) Treatment Using Magnetic Resonance Imaging (MRI) and Au329(SR)84, Au329-xAgx-(SR)84, Au144(SR)60, Au68(SR)36, Au30(SR)18, Au102(SPh)44, Au38(SPh)24, Au38(SC2H4Ph)24, Au21S(SAdm)15, Au36(pMBA)24 and Au25(pMBA)18 Nano Clusters. J Surgery Emerg Med., 2017, 1: 21.

[75] A. Heidari. Developmental Cell Biology in Adult Stem Cells Death and Autophagy to Trigger a Preventive Allergic Reaction to Common Airborne Allergens under Synchrotron Radiation Using Nanotechnology for Therapeutic Goals in Particular Allergy Shots (Immunotherapy). Cell Biol (Henderson, NV), 2017, 6: 1.

 DOI: https://doi.org/10.30564/ssid.v1i2.1827

[76] A. Heidari. Changing Metal Powder Characteristics for Elimination of the Heavy Metals Toxicity and Diseases in Disruption of Extracellular Matrix (ECM) Proteins Adjustment in Cancer Metastases Induced by Osteosarcoma, Chondrosarcoma, Carcinoid, Carcinoma, Ewing's Sarcoma, Fibrosarcoma and Secondary Hematopoietic Solid or Soft Tissue Tumors. J Powder Metall Min., 2017, 6: 170.

[77] A. Heidari. Nanomedicine-Based Combination Anti-Cancer Therapy between Nucleic Acids and Anti-Cancer Nano Drugs in Covalent Nano Drugs Delivery Systems for Selective Imaging and Treatment of Human Brain Tumors Using Hyaluronic Acid, Alguronic Acid and Sodium Hyaluronate as Anti-Cancer Nano Drugs and Nucleic Acids Delivery under Synchrotron Radiation. Am J Drug Deliv., 2017, 5: 2.

[78] A. Heidari. Clinical Trials of Dendritic Cell Therapies for Cancer Exposing Vulnerabilities in Human Cancer Cells' Metabolism and Metabolomics: New Discoveries, Unique Features Inform New Therapeutic Opportunities, Biotech's Bumpy Road to the Market and Elucidating the Biochemical Programs that Support Cancer Initiation and Progression. J Biol Med Science, 2017, 1: e103.

[79] A. Heidari. The Design Graphene-Based Nanosheets as a New Nanomaterial in Anti-Cancer Therapy and Delivery of Chemotherapeutics and Biological Nano Drugs for Liposomal Anti-Cancer Nano Drugs and Gene Delivery. Br Biomed Bull, 2017, 5: 305.

[80] A. Haidari. Integrative Approach to Biological Networks for Emerging Roles of Proteomics, Genomics and Transcriptomics in the Discovery and Validation of Human Colorectal Cancer Biomarkers from DNA/RNA Sequencing Data under Synchrotron Radiation. Transcriptomics, 2017, 5: e117.

[81] A. Heidari. Elimination of the Heavy Metals Toxicity and Diseases in Disruption of Extracellular Matrix (ECM) Proteins and Cell Adhesion Intelligent Nanomolecules Adjustment in Cancer Metastases Using Metalloenzymes and under Synchrotron Radiation. Lett Health Biol Sci., 2017, 2 (2): 1-4.

[82] A. Heidari. Treatment of Breast Cancer Brain Metastases through a Targeted Nanomolecule Drug Delivery System Based on Dopamine Functionalized Multi-Wall Carbon Nanotubes (MWCNTs) Coated with Nano Graphene Oxide (GO) and Protonated Polyaniline (PANI) in Situ During the Polymerization of Aniline Autogenic Nanoparticles for the Delivery of Anti-Cancer Nano Drugs under Synchrotron Radiation. Br J Res., 2017, 4 (3): 16.

[83] A. Heidari. Sedative, Analgesic and Ultrasound-Mediated Gastrointestinal Nano Drugs Delivery for Gastrointestinal Endoscopic Procedure, Nano Drug-Induced Gastrointestinal Disorders and Nano Drug Treatment of Gastric Acidity. Res Rep Gastroenterol, 2017, 1: 1.

[84] A. Heidari. Synthesis, Pharmacokinetics, Pharmacodynamics, Dosing, Stability, Safety and Efficacy of Orphan Nano Drugs to Treat High Cholesterol and Related Conditions and to Prevent Cardiovascular Disease under Synchrotron Radiation. J Pharm Sci Emerg Drugs, 2017, 5: 1.

[85] A. Heidari. Non-Linear Compact Proton Synchrotrons to Improve Human Cancer Cells and Tissues Treatments and Diagnostics through Particle Therapy Accelerators with Monochromatic Microbeams. J Cell Biol Mol Sci., 2017, 2 (1): 1-5.

[86] A. Heidari. Design of Targeted Metal Chelation Therapeutics Nanocapsules as Colloidal Carriers and Blood-Brain Barrier (BBB) Translocation to Targeted Deliver Anti-Cancer Nano Drugs into the Human Brain to Treat Alzheimer's Disease under Synchrotron Radiation. J Nanotechnol Material Sci., 2017, 4 (2): 1-5.

[87] R. Gobato, A. Heidari. Calculations Using Quantum Chemistry for Inorganic Molecule Simulation BeLi2SeSi. Science Journal of Analytical Chemistry, 2017, 5(6): 76-85.

[88] A. Heidari. Different High-Resolution Simulations of Medical, Medicinal, Clinical, Pharmaceutical and Therapeutics Oncology of Human Lung Cancer Translational Anti-Cancer Nano Drugs Delivery Treatment Process under Synchrotron and X-Ray Radiations. J Med Oncol., 2017, 1(1): 1.

[89] A. Heidari. A Modern Ethnomedicinal Technique for Transformation, Prevention and Treatment of Human Malignant Gliomas Tumors into Human Benign Gliomas Tumors under Synchrotron Radiation. Am J Ethnomed, 2017, 4(1): 10.

[90] A. Heidari. Active Targeted Nanoparticles for Anti-Cancer Nano Drugs Delivery across the Blood-Brain Barrier for Human Brain Cancer Treatment, Multiple Sclerosis (MS) and Alzheimer's Diseases Using Chemical Modifications of Anti-Cancer Nano Drugs or Drug-Nanoparticles through Zika Virus (ZIKV) Nanocarriers under Synchrotron Radiation. J Med Chem Toxicol, 2017, 2 (3): 1-5.

[91] A. Heidari. Investigation of Medical, Medicinal, Clinical and Pharmaceutical Applications of Estradiol, Mestranol (Norlutin), Norethindrone (NET), Norethisterone Acetate (NETA), Norethisterone Enanthate (NETE) and Testosterone Nanoparticles as Biological Imaging, Cell Labeling, Anti-Microbial Agents and Anti-Cancer Nano Drugs in Nanomedi-

DOI: https://doi.org/10.30564/ssid.v1i2.1827

cines Based Drug Delivery Systems for Anti-Cancer Targeting and Treatment. Parana Journal of Science and Education (PJSE), 2017, 3(4): 10-19.

[92] A. Heidari. A Comparative Computational and Experimental Study on Different Vibrational Biospectroscopy Methods, Techniques and Applications for Human Cancer Cells in Tumor Tissues Simulation, Modeling, Research, Diagnosis and Treatment. Open J Anal Bioanal Chem, 2017, 1(1): 014-020.

[93] A. Heidari. Combination of DNA/RNA Ligands and Linear/Non-Linear Visible-Synchrotron Radiation-Driven N-Doped Ordered Mesoporous Cadmium Oxide (CdO) Nanoparticles Photocatalysts Channels Resulted in an Interesting Synergistic Effect Enhancing Catalytic Anti-Cancer Activity. Enz Eng., 2017, 6: 1.

[94] A. Heidari. Modern Approaches in Designing Ferritin, Ferritin Light Chain, Transferrin, Beta-2 Transferrin and Bacterioferritin-Based Anti-Cancer Nano Drugs Encapsulating Nanosphere as DNA-Binding Proteins from Starved Cells (DPS). Mod Appro Drug Des., 2017, 1(1): MADD.000504.

[95] A. Heidari. Potency of Human Interferon β-1a and Human Interferon β-1b in Enzymotherapy, Immunotherapy, Chemotherapy, Radiotherapy, Hormone Therapy and Targeted Therapy of Encephalomyelitis Disseminate/Multiple Sclerosis (MS) and Hepatitis A, B, C, D, E, F and G Virus Enter and Targets Liver Cells. J Proteomics Enzymol, 2017, 6: 1.

[96] A. Heidari. Transport Therapeutic Active Targeting of Human Brain Tumors Enable Anti-Cancer Nanodrugs Delivery across the Blood-Brain Barrier (BBB) to Treat Brain Diseases Using Nanoparticles and Nanocarriers under Synchrotron Radiation. J Pharm Pharmaceutics, 2017, 4(2): 1-5.

[97] A. Heidari, C. Brown. Combinatorial Therapeutic Approaches to DNA/RNA and Benzylpenicillin (Penicillin G), Fluoxetine Hydrochloride (Prozac and Sarafem), Propofol (Diprivan), Acetylsalicylic Acid (ASA) (Aspirin), Naproxen Sodium (Aleve and Naprosyn) and Dextromethamphetamine Nanocapsules with Surface Conjugated DNA/RNA to Targeted Nano Drugs for Enhanced Anti-Cancer Efficacy and Targeted Cancer Therapy Using Nano Drugs Delivery Systems. Ann Adv Chem., 2017, 1(2): 061-069.

[98] A. Heidari. High-Resolution Simulations of Human Brain Cancer Translational Nano Drugs Delivery Treatment Process under Synchrotron Radiation. J Transl Res., 2017, 1(1): 1-3.

[99] A. Heidari. Investigation of Anti-Cancer Nano Drugs' Effects' Trend on Human Pancreas Cancer Cells and Tissues Prevention, Diagnosis and Treatment Process under Synchrotron and X-Ray Radiations with the Passage of Time Using Mathematica. Current Trends Anal Bioanal Chem, 2017, 1(1): 36-41.

[100] A. Heidari. Pros and Cons Controversy on Molecular Imaging and Dynamics of Double-Standard DNA/RNA of Human Preserving Stem Cells-Binding Nano Molecules with Androgens/Anabolic Steroids (AAS) or Testosterone Derivatives through Tracking of Helium-4 Nucleus (Alpha Particle) Using Synchrotron Radiation. Arch Biotechnol Biomed, 2017, 1(1): 067-0100.

[101] A. Heidari. Visualizing Metabolic Changes in Probing Human Cancer Cells and Tissues Metabolism Using Vivo ^{1}H or Proton NMR, ^{13}C NMR, ^{15}N NMR and ^{31}P NMR Spectroscopy and Self-Organizing Maps under Synchrotron Radiation. SOJ Mater Sci Eng., 2017, 5 (2): 1-6.

[102] A. Heidari. Cavity Ring-Down Spectroscopy (CRDS), Circular Dichroism Spectroscopy, Cold Vapour Atomic Fluorescence Spectroscopy and Correlation Spectroscopy Comparative Study on Malignant and Benign Human Cancer Cells and Tissues with the Passage of Time under Synchrotron Radiation. Enliven: Challenges Cancer Detect Ther, 2017, 4 (2): e001.

[103] A. Heidari. Laser Spectroscopy, Laser-Induced Breakdown Spectroscopy and Laser-Induced Plasma Spectroscopy Comparative Study on Malignant and Benign Human Cancer Cells and Tissues with the Passage of Time under Synchrotron Radiation. Int J Hepatol Gastroenterol, 2017, 3 (4): 079-084.

[104] A. Heidari. Time-Resolved Spectroscopy and Time-Stretch Spectroscopy Comparative Study on Malignant and Benign Human Cancer Cells and Tissues with the Passage of Time under Synchrotron Radiation. Enliven: Pharmacovigilance and Drug Safety, 2017, 4 (2): e001.

[105] A. Heidari. Overview of the Role of Vitamins in Reducing Negative Effect of Decapeptyl (Triptorelin Acetate or Pamoate Salts) on Prostate Cancer Cells and Tissues in Prostate Cancer Treatment Process through Transformation of Malignant Prostate Tumors into Benign Prostate Tumors under Synchrotron Radiation. Open J Anal Bioanal Chem, 2017, 1(1): 021-026.

[106] A. Heidari. Electron Phenomenological Spectroscopy, Electron Paramagnetic Resonance (EPR) Spectroscopy and Electron Spin Resonance (ESR) Spectroscopy Comparative Study on Malignant and Benign Human Cancer Cells and Tissues with the Passage of Time under Synchrotron Radiation. Aus-

 DOI: https://doi.org/10.30564/ssid.v1i2.1827

tin J Anal Pharm Chem., 2017, 4(3): 1091.

[107] A. Heidari. Therapeutic Nanomedicine Different High-Resolution Experimental Images and Computational Simulations for Human Brain Cancer Cells and Tissues Using Nanocarriers Deliver DNA/RNA to Brain Tumors under Synchrotron Radiation with the Passage of Time Using Mathematica and MATLAB. Madridge J Nano Tech. Sci., 2017, 2(2): 77-83.

[108] A. Heidari. A Consensus and Prospective Study on Restoring Cadmium Oxide (CdO) Nanoparticles Sensitivity in Recurrent Ovarian Cancer by Extending the Cadmium Oxide (CdO) Nanoparticles-Free Interval Using Synchrotron Radiation Therapy as Antibody-Drug Conjugate for the Treatment of Limited-Stage Small Cell Diverse Epithelial Cancers. Cancer Clin Res Rep, 2017, 1: 2, e001.

[109] A. Heidari. A Novel and Modern Experimental Imaging and Spectroscopy Comparative Study on Malignant and Benign Human Cancer Cells and Tissues with the Passage of Time under White Synchrotron Radiation. Cancer Sci Res Open Access, 2017, 4(2): 1-8.

[110] A. Heidari. Different High-Resolution Simulations of Medical, Medicinal, Clinical, Pharmaceutical and Therapeutics Oncology of Human Breast Cancer Translational Nano Drugs Delivery Treatment Process under Synchrotron and X-Ray Radiations. J Oral Cancer Res., 2017, 1(1): 12-17.

[111] A. Heidari. Vibrational Decihertz (dHz), Centihertz (cHz), Millihertz (mHz), Microhertz (μHz), Nanohertz (nHz), Picohertz (pHz), Femtohertz (fHz), Attohertz (aHz), Zeptohertz (zHz) and Yoctohertz (yHz) Imaging and Spectroscopy Comparative Study on Malignant and Benign Human Cancer Cells and Tissues under Synchrotron Radiation. International Journal of Biomedicine, 2017, 7(4): 335-340.

[112] A. Heidari. Force Spectroscopy and Fluorescence Spectroscopy Comparative Study on Malignant and Benign Human Cancer Cells and Tissues with the Passage of Time under Synchrotron Radiation. EC Cancer, 2017, 2(5): 239-246.

[113] A. Heidari. Photoacoustic Spectroscopy, Photoemission Spectroscopy and Photothermal Spectroscopy Comparative Study on Malignant and Benign Human Cancer Cells and Tissues with the Passage of Time under Synchrotron Radiation. BAOJ Cancer Res Ther., 2017, 3(3): 045-052.

[114] A. Heidari. J-Spectroscopy, Exchange Spectroscopy (EXSY), Nuclear Overhauser Effect Spectroscopy (NOESY) and Total Correlation Spectroscopy (TOCSY) Comparative Study on Malignant and Benign Human Cancer Cells and Tissues under Synchrotron Radiation. EMS Eng Sci J, 2017, 1(2): 006-013.

[115] A. Heidari. Neutron Spin Echo Spectroscopy and Spin Noise Spectroscopy Comparative Study on Malignant and Benign Human Cancer Cells and Tissues with the Passage of Time under Synchrotron Radiation. Int J Biopharm Sci, 2017, 1: 103-107.

[116] A. Heidari. Vibrational Decahertz (daHz), Hectohertz (hHz), Kilohertz (kHz), Megahertz (MHz), Gigahertz (GHz), Terahertz (THz), Petahertz (PHz), Exahertz (EHz), Zettahertz (ZHz) and Yottahertz (YHz) Imaging and Spectroscopy Comparative Study on Malignant and Benign Human Cancer Cells and Tissues under Synchrotron Radiation. Madridge J Anal Sci Instrum, 2017, 2(1): 41-46.

[117] A. Heidari. Two-Dimensional Infrared Correlation Spectroscopy, Linear Two-Dimensional Infrared Spectroscopy and Non-Linear Two-Dimensional Infrared Spectroscopy Comparative Study on Malignant and Benign Human Cancer Cells and Tissues under Synchrotron Radiation with the Passage of Time. J Mater Sci Nanotechnol, 2018, 6(1): 101.

[118] A. Heidari. Fourier Transform Infrared (FTIR) Spectroscopy, Near-Infrared Spectroscopy (NIRS) and Mid-Infrared Spectroscopy (MIRS) Comparative Study on Malignant and Benign Human Cancer Cells and Tissues under Synchrotron Radiation with the Passage of Time. Int J Nanotechnol Nanomed, 2018, 3(1): 1-6.

[119] A. Heidari. Infrared Photo Dissociation Spectroscopy and Infrared Correlation Table Spectroscopy Comparative Study on Malignant and Benign Human Cancer Cells and Tissues under Synchrotron Radiation with the Passage of Time. Austin Pharmacol Pharm, 2018, 3(1): 1011.

[120] A. Heidari. Novel and Transcendental Prevention, Diagnosis and Treatment Strategies for Investigation of Interaction among Human Blood Cancer Cells, Tissues, Tumors and Metastases with Synchrotron Radiation under Anti-Cancer Nano Drugs Delivery Efficacy Using MATLAB Modeling and Simulation. Madridge J Nov Drug Res, 2017, 1(1): 18-24.

[121] A. Heidari. Comparative Study on Malignant and Benign Human Cancer Cells and Tissues with the Passage of Time under Synchrotron Radiation. Open Access J Trans Med Res., 2018, 2 (1): 00026-00032.

[122] M. R. R. Gobato, R. Gobato, A. Heidari. Planting of Jaboticaba Trees for Landscape Repair of Degraded Area. Landscape Architecture and Regional Planning, 2018, 3(1): 1-9.

[123] A. Heidari. Fluorescence Spectroscopy, Phospho-

DOI: https://doi.org/10.30564/ssid.v1i2.1827

rescence Spectroscopy and Luminescence Spectroscopy Comparative Study on Malignant and Benign Human Cancer Cells and Tissues under Synchrotron Radiation with the Passage of Time. SM J Clin. Med. Imaging, 2018, 4(1): 1018.

[124] A. Heidari. Nuclear Inelastic Scattering Spectroscopy (NISS) and Nuclear Inelastic Absorption Spectroscopy (NIAS) Comparative Study on Malignant and Benign Human Cancer Cells and Tissues under Synchrotron Radiation. Int J Pharm Sci., 2018, 2(1): 1-14.

[125] A. Heidari. X-Ray Diffraction (XRD), Powder X-Ray Diffraction (PXRD) and Energy-Dispersive X-Ray Diffraction (EDXRD) Comparative Study on Malignant and Benign Human Cancer Cells and Tissues under Synchrotron Radiation. J Oncol Res., 2018, 2(1): 1-14.

[126] A. Heidari. Correlation Two-Dimensional Nuclear Magnetic Resonance (NMR) (2D-NMR) (COSY) Imaging and Spectroscopy Comparative Study on Malignant and Benign Human Cancer Cells and Tissues under Synchrotron Radiation. EMS Can Sci., 2018, 1-1-001.

[127] A. Heidari. Thermal Spectroscopy, Photothermal Spectroscopy, Thermal Microspectroscopy, Photothermal Microspectroscopy, Thermal Macrospectroscopy and Photothermal Macrospectroscopy Comparative Study on Malignant and Benign Human Cancer Cells and Tissues with the Passage of Time under Synchrotron Radiation. SM J Biometrics Biostat, 2018, 3(1): 1024.

[128] A. Heidari. A Modern and Comprehensive Experimental Biospectroscopic Comparative Study on Human Common Cancers' Cells, Tissues and Tumors before and after Synchrotron Radiation Therapy. Open Acc J Oncol Med., 2018, 1(1).

[129] A. Heidari. Heteronuclear Correlation Experiments such as Heteronuclear Single-Quantum Correlation Spectroscopy (HSQC), Heteronuclear Multiple-Quantum Correlation Spectroscopy (HMQC) and Heteronuclear Multiple-Bond Correlation Spectroscopy (HMBC) Comparative Study on Malignant and Benign Human Endocrinology and Thyroid Cancer Cells and Tissues under Synchrotron Radiation. J Endocrinol Thyroid Res., 2018, 3(1): 555603.

[130] A. Heidari. Nuclear Resonance Vibrational Spectroscopy (NRVS), Nuclear Inelastic Scattering Spectroscopy (NISS), Nuclear Inelastic Absorption Spectroscopy (NIAS) and Nuclear Resonant Inelastic X-Ray Scattering Spectroscopy (NRIXSS) Comparative Study on Malignant and Benign Human Cancer Cells and Tissues under Synchrotron Radiation. Int J Bioorg Chem Mol Biol., 2018, 6(1e): 1-5.

[131] A. Heidari. A Novel and Modern Experimental Approach to Vibrational Circular Dichroism Spectroscopy and Video Spectroscopy Comparative Study on Malignant and Benign Human Cancer Cells and Tissues with the Passage of Time under White and Monochromatic Synchrotron Radiation. Glob J Endocrinol Metab, 2018 1(3). GJEM. 000514-000519.

[132] A. Heidari. Pros and Cons Controversy on Heteronuclear Correlation Experiments such as Heteronuclear Single-Quantum Correlation Spectroscopy (HSQC), Heteronuclear Multiple-Quantum Correlation Spectroscopy (HMQC) and Heteronuclear Multiple-Bond Correlation Spectroscopy (HMBC) Comparative Study on Malignant and Benign Human Cancer Cells and Tissues under Synchrotron Radiation. EMS Pharma J., 2018, 1(1): 002-008.

[133] A. Heidari. A Modern Comparative and Comprehensive Experimental Biospectroscopic Study on Different Types of Infrared Spectroscopy of Malignant and Benign Human Cancer Cells and Tissues with the Passage of Time under Synchrotron Radiation. J Analyt Molecul Tech., 2018, 3(1): 8.

[134] A. Heidari. Investigation of Cancer Types Using Synchrotron Technology for Proton Beam Therapy: An Experimental Biospectroscopic Comparative Study. European Modern Studies Journal, 2018, 2(1): 13-29.

[135] A. Heidari. Saturated Spectroscopy and Unsaturated Spectroscopy Comparative Study on Malignant and Benign Human Cancer Cells and Tissues with the Passage of Time under Synchrotron Radiation. Imaging J Clin Medical Sci., 2018, 5(1): 001-007.

[136] A. Heidari. Small-Angle Neutron Scattering (SANS) and Wide-Angle X-Ray Diffraction (WAXD) Comparative Study on Malignant and Benign Human Cancer Cells and Tissues under Synchrotron Radiation. Int J Bioorg Chem Mol Biol., 2018, 6(2e): 1-6.

[137] A. Heidari. Investigation of Bladder Cancer, Breast Cancer, Colorectal Cancer, Endometrial Cancer, Kidney Cancer, Leukemia, Liver, Lung Cancer, Melanoma, Non-Hodgkin Lymphoma, Pancreatic Cancer, Prostate Cancer, Thyroid Cancer and Non-Melanoma Skin Cancer Using Synchrotron Technology for Proton Beam Therapy: An Experimental Biospectroscopic Comparative Study. Ther Res Skin Dis., 2018, 1(1).

[138] A. Heidari. Attenuated Total Reflectance Fourier Transform Infrared (ATR-FTIR) Spectroscopy, Micro-Attenuated Total Reflectance Fourier Transform Infrared (Micro-ATR-FTIR) Spectroscopy and Macro-Attenuated Total Reflectance Fourier Transform

 DOI: https://doi.org/10.30564/ssid.v1i2.1827

Infrared (Macro-ATR-FTIR) Spectroscopy Comparative Study on Malignant and Benign Human Cancer Cells and Tissues under Synchrotron Radiation with the Passage of Time. International Journal of Chemistry Papers, 2018, 2(1): 1-12.

[139] A. Heidari. Mössbauer Spectroscopy, Mössbauer Emission Spectroscopy and ^{57}Fe Mössbauer Spectroscopy Comparative Study on Malignant and Benign Human Cancer Cells and Tissues under Synchrotron Radiation. Acta Scientific Cancer Biology, 2018, 2.3: 17-20.

[140] A. Heidari. Comparative Study on Malignant and Benign Human Cancer Cells and Tissues under Synchrotron Radiation with the Passage of Time. Organic & Medicinal Chem IJ., 2018, 6(1): 555676.

[141] A. Heidari. Correlation Spectroscopy, Exclusive Correlation Spectroscopy and Total Correlation Spectroscopy Comparative Study on Malignant and Benign Human AIDS-Related Cancers Cells and Tissues with the Passage of Time under Synchrotron Radiation. Int J Bioanal Biomed, 2018, 2(1): 001-007.

[142] A. Heidari. Biomedical Instrumentation and Applications of Biospectroscopic Methods and Techniques in Malignant and Benign Human Cancer Cells and Tissues Studies under Synchrotron Radiation and Anti-Cancer Nano Drugs Delivery. Am J Nanotechnol Nanomed, 2018, 1(1): 001-009.

[143] A. Heidari. Vivo ^{1}H or Proton NMR, ^{13}C NMR, ^{15}N NMR and ^{31}P NMR Spectroscopy Comparative Study on Malignant and Benign Human Cancer Cells and Tissues under Synchrotron Radiation", Ann Biomet Biostat., 2018, 1(1): 1001.

[144] A. Heidari. Grazing-Incidence Small-Angle Neutron Scattering (GISANS) and Grazing-Incidence X-Ray Diffraction (GIXD) Comparative Study on Malignant and Benign Human Cancer Cells, Tissues and Tumors under Synchrotron Radiation. Ann Cardiovasc Surg., 2018, 1(2): 1006.

[145] A. Heidari. Adsorption Isotherms and Kinetics of Multi-Walled Carbon Nanotubes (MWCNTs), Boron Nitride Nanotubes (BNNTs), Amorphous Boron Nitride Nanotubes (a-BNNTs) and Hexagonal Boron Nitride Nanotubes (h-BNNTs) for Eliminating Carcinoma, Sarcoma, Lymphoma, Leukemia, Germ Cell Tumor and Blastoma Cancer Cells and Tissues. Clin Med Rev Case Rep., 2018, 5: 201.

[146] A. Heidari. Correlation Spectroscopy (COSY), Exclusive Correlation Spectroscopy (ECOSY), Total Correlation Spectroscopy (TOCSY), Incredible Natural-Abundance Double-Quantum Transfer Experiment (INADEQUATE), Heteronuclear Single-Quantum Correlation Spectroscopy (HSQC), Heteronuclear Multiple-Bond Correlation Spectroscopy (HMBC), Nuclear Overhauser Effect Spectroscopy (NOESY) and Rotating Frame Nuclear Overhauser Effect Spectroscopy (ROESY) Comparative Study on Malignant and Benign Human Cancer Cells and Tissues under Synchrotron Radiation. Acta Scientific Pharmaceutical Sciences, 2018, 2.5: 30-35.

[147] A. Heidari. Small-Angle X-Ray Scattering (SAXS), Ultra-Small Angle X-Ray Scattering (USAXS), Fluctuation X-Ray Scattering (FXS), Wide-Angle X-Ray Scattering (WAXS), Grazing-Incidence Small-Angle X-Ray Scattering (GISAXS), Grazing-Incidence Wide-Angle X-Ray Scattering (GIWAXS), Small-Angle Neutron Scattering (SANS), Grazing-Incidence Small-Angle Neutron Scattering (GISANS), X-Ray Diffraction (XRD), Powder X-Ray Diffraction (PXRD), Wide-Angle X-Ray Diffraction (WAXD), Grazing-Incidence X-Ray Diffraction (GIXD) and Energy-Dispersive X-Ray Diffraction (EDXRD) Comparative Study on Malignant and Benign Human Cancer Cells and Tissues under Synchrotron Radiation. Oncol Res Rev., 2018, 1(1): 1-10.

[148] A. Heidari. Pump-Probe Spectroscopy and Transient Grating Spectroscopy Comparative Study on Malignant and Benign Human Cancer Cells and Tissues with the Passage of Time under Synchrotron Radiation. Adv Material Sci Engg, 2018, 2(1): 1-7.

[149] A. Heidari. Grazing-Incidence Small-Angle X-Ray Scattering (GISAXS) and Grazing-Incidence Wide-Angle X-Ray Scattering (GIWAXS) Comparative Study on Malignant and Benign Human Cancer Cells and Tissues under Synchrotron Radiation. Insights Pharmacol Pharm Sci., 2018, 1(1): 1-8.

[150] A. Heidari. Acoustic Spectroscopy, Acoustic Resonance Spectroscopy and Auger Spectroscopy Comparative Study on Anti-Cancer Nano Drugs Delivery in Malignant and Benign Human Cancer Cells and Tissues with the Passage of Time under Synchrotron Radiation. Nanosci Technol, 2018, 5(1): 1-9.

[151] A. Heidari. Niobium, Technetium, Ruthenium, Rhodium, Hafnium, Rhenium, Osmium and Iridium Ions Incorporation into the Nano Polymeric Matrix (NPM) by Immersion of the Nano Polymeric Modified Electrode (NPME) as Molecular Enzymes and Drug Targets for Human Cancer Cells, Tissues and Tumors Treatment under Synchrotron and Synchrocyclotron Radiations. Nanomed Nanotechnol, 2018, 3(2): 000138.

[152] A. Heidari. Homonuclear Correlation Experiments

DOI: https://doi.org/10.30564/ssid.v1i2.1827

such as Homonuclear Single-Quantum Correlation Spectroscopy (HSQC), Homonuclear Multiple-Quantum Correlation Spectroscopy (HMQC) and Homonuclear Multiple-Bond Correlation Spectroscopy (HMBC) Comparative Study on Malignant and Benign Human Cancer Cells and Tissues under Synchrotron Radiation. Austin J Proteomics Bioinform & Genomics, 2018, 5(1): 1024.

[153] A. Heidari. Atomic Force Microscopy Based Infrared (AFM-IR) Spectroscopy and Nuclear Resonance Vibrational Spectroscopy Comparative Study on Malignant and Benign Human Cancer Cells and Tissues under Synchrotron Radiation with the Passage of Time. J Appl Biotechnol Bioeng, 2018, 5(3): 142-148.

[154] A. Heidari. Time-Dependent Vibrational Spectral Analysis of Malignant and Benign Human Cancer Cells and Tissues under Synchrotron Radiation. J Cancer Oncol., 2018, 2(2): 000124.

[155] A. Heidari. Palauamine and Olympiadane Nano Molecules Incorporation into the Nano Polymeric Matrix (NPM) by Immersion of the Nano Polymeric Modified Electrode (NPME) as Molecular Enzymes and Drug Targets for Human Cancer Cells, Tissues and Tumors Treatment under Synchrotron and Synchrocyclotron Radiations. Arc Org Inorg Chem Sci., 2018, 3(1).

[156] R. Gobato, A. Heidari. Infrared Spectrum and Sites of Action of Sanguinarine by Molecular Mechanics and ab initio Methods. International Journal of Atmospheric and Oceanic Sciences, 2018, 2(1): 1-9.

[157] A. Heidari. Angelic Acid, Diabolic Acids, Draculin and Miraculin Nano Molecules Incorporation into the Nano Polymeric Matrix (NPM) by Immersion of the Nano Polymeric Modified Electrode (NPME) as Molecular Enzymes and Drug Targets for Human Cancer Cells, Tissues and Tumors Treatment Under Synchrotron and Synchrocyclotron Radiations. Med & Analy Chem Int J, 2018, 2(1): 000111.

[158] A. Heidari. "Gamma Linolenic Methyl Ester, 5-Heptadeca-5,8,11-Trienyl 1,3,4-Oxadiazole-2-Thiol, Sulphoquinovosyl Diacyl Glycerol, Ruscogenin, Nocturnoside B, Protodioscine B, Parquisoside-B, Leiocarposide, Narangenin, 7-Methoxy Hespertin, Lupeol, Rosemariquinone, Rosmanol and Rosemadiol Nano Molecules Incorporation into the Nano Polymeric Matrix (NPM) by Immersion of the Nano Polymeric Modified Electrode (NPME) as Molecular Enzymes and Drug Targets for Human Cancer Cells, Tissues and Tumors Treatment under Synchrotron and Synchrocyclotron Radiations. Int J Pharma Anal Acta, 2018, 2(1): 007-014.

[159] A. Heidari. Fourier Transform Infrared (FTIR) Spectroscopy, Attenuated Total Reflectance Fourier Transform Infrared (ATR-FTIR) Spectroscopy, Micro-Attenuated Total Reflectance Fourier Transform Infrared (Micro-ATR-FTIR) Spectroscopy, Macro-Attenuated Total Reflectance Fourier Transform Infrared (Macro-ATR-FTIR) Spectroscopy, Two-Dimensional Infrared Correlation Spectroscopy, Linear Two-Dimensional Infrared Spectroscopy, Non-Linear Two-Dimensional Infrared Spectroscopy, Atomic Force Microscopy Based Infrared (AFM-IR) Spectroscopy, Infrared Photodissociation Spectroscopy, Infrared Correlation Table Spectroscopy, Near-Infrared Spectroscopy (NIRS), Mid-Infrared Spectroscopy (MIRS), Nuclear Resonance Vibrational Spectroscopy, Thermal Infrared Spectroscopy and Photothermal Infrared Spectroscopy Comparative Study on Malignant and Benign Human Cancer Cells and Tissues under Synchrotron Radiation with the Passage of Time", Glob Imaging Insights, 2018, 3(2): 1-14.

[160] A. Heidari. Heteronuclear Single-Quantum Correlation Spectroscopy (HSQC) and Heteronuclear Multiple-Bond Correlation Spectroscopy (HMBC) Comparative Study on Malignant and Benign Human Cancer Cells, Tissues and Tumors under Synchrotron and Synchrocyclotron Radiations. Chronicle of Medicine and Surgery, 2018, 2(3): 144-156.

[161] A. Heidari. Tetrakis [3, 5-bis (Trifluoromethyl) Phenyl] Borate (BARF)-Enhanced Precatalyst Preparation Stabilization and Initiation (EPPSI) Nano Molecules. Medical Research and Clinical Case Reports, 2018, 2(1): 113-126.

[162] A. Heidari. Sydnone, Münchnone, Montréalone, Mogone, Montelukast, Quebecol and Palau'amine-Enhanced Precatalyst Preparation Stabilization and Initiation (EPPSI) Nano Molecules. Sur Cas Stud Op Acc J., 2018, 1(3).

[163] A. Heidari. Fornacite, Orotic Acid, Rhamnetin, Sodium Ethyl Xanthate (SEX) and Spermine (Spermidine or Polyamine) Nanomolecules Incorporation into the Nanopolymeric Matrix (NPM). International Journal of Biochemistry and Biomolecules, 2018, 4(1): 1-19.

[164] A. Heidari, R. Gobato. Putrescine, Cadaverine, Spermine and Spermidine-Enhanced Precatalyst Preparation Stabilization and Initiation (EPPSI) Nano Molecules. Parana Journal of Science and Education (PJSE), 2018, 4(5): 1-14.

[165] A. Heidari. Cadaverine (1,5-Pentanediamine or Pentamethylenediamine), Diethyl Azodicarboxylate (DEAD or DEADCAT) and Putrescine (Tetramethylenediamine) Nano Molecules Incorporation into

 DOI: https://doi.org/10.30564/ssid.v1i2.1827

the Nano Polymeric Matrix (NPM) by Immersion of the Nano Polymeric Modified Electrode (NPME) as Molecular Enzymes and Drug Targets for Human Cancer Cells, Tissues and Tumors Treatment under Synchrotron and Synchrocyclotron Radiations. Hiv and Sexual Health Open Access Open Journal, 2018, 1(1): 4-11.

[166] A. Heidari. Improving the Performance of Nano-Endofullerenes in Polyaniline Nanostructure-Based Biosensors by Covering Californium Colloidal Nanoparticles with Multi-Walled Carbon Nanotubes. Journal of Advances in Nanomaterials, 2018, 3(1): 1-28.

[167] R. Gobato, A. Heidari. Molecular Mechanics and Quantum Chemical Study on Sites of Action of Sanguinarine Using Vibrational Spectroscopy Based on Molecular Mechanics and Quantum Chemical Calculations. Malaysian Journal of Chemistry, 2018, 20(1), 1-23.

[168] A. Heidari. Vibrational Biospectroscopic Studies on Anti-cancer Nanopharmaceuticals (Part I). Malaysian Journal of Chemistry, 2018, 20(1), 33-73.

[169] A. Heidari. Vibrational Biospectroscopic Studies on Anti-cancer Nanopharmaceuticals (Part II). Malaysian Journal of Chemistry, 2018, 20(1): 74-117.

[170] A. Heidari. Uranocene ($U(C_8H_8)_2$) and Bis(Cyclooctatetraene)Iron ($Fe(C_8H_8)_2$ or $Fe(COT)_2$)-Enhanced Precatalyst Preparation Stabilization and Initiation (EPPSI) Nano Molecules. Chemistry Reports, 2018, 1(2): 1-16.

[171] A. Heidari. Biomedical Systematic and Emerging Technological Study on Human Malignant and Benign Cancer Cells and Tissues Biospectroscopic Analysis under Synchrotron Radiation. Glob Imaging Insights, 2018, 3(3): 1-7.

[172] A. Heidari. Deep-Level Transient Spectroscopy and X-Ray Photoelectron Spectroscopy (XPS) Comparative Study on Malignant and Benign Human Cancer Cells and Tissues with the Passage of Time under Synchrotron Radiation. Res Dev Material Sci., 2018, 7(2). RDMS.000659.

[173] A. Heidari. C70-Carboxyfullerenes Nano Molecules Incorporation into the Nano Polymeric Matrix (NPM) by Immersion of the Nano Polymeric Modified Electrode (NPME) as Molecular Enzymes and Drug Targets for Human Cancer Cells, Tissues and Tumors Treatment under Synchrotron and Synchrocyclotron Radiations. Glob Imaging Insights, 2018, (3): 1-7.

[174] A. Heidari. The Effect of Temperature on Cadmium Oxide (CdO) Nanoparticles Produced by Synchrotron Radiation in the Human Cancer Cells, Tissues and Tumors. International Journal of Advanced Chemistry, 2018, 6(2): 140-156.

[175] A. Heidari. A Clinical and Molecular Pathology Investigation of Correlation Spectroscopy (COSY), Exclusive Correlation Spectroscopy (ECOSY), Total Correlation Spectroscopy (TOCSY), Heteronuclear Single-Quantum Correlation Spectroscopy (HSQC) and Heteronuclear Multiple-Bond Correlation Spectroscopy (HMBC) Comparative Study on Malignant and Benign Human Cancer Cells, Tissues and Tumors under Synchrotron and Synchrocyclotron Radiations Using Cyclotron versus Synchrotron, Synchrocyclotron and the Large Hadron Collider (LHC) for Delivery of Proton and Helium Ion (Charged Particle) Beams for Oncology Radiotherapy. European Journal of Advances in Engineering and Technology, 2018, 5(7): 414-426.

[176] A. Heidari. Nano Molecules Incorporation into the Nano Polymeric Matrix (NPM) by Immersion of the Nano Polymeric Modified Electrode (NPME) as Molecular Enzymes and Drug Targets for Human Cancer Cells, Tissues and Tumors Treatment under Synchrotron and Synchrocyclotron Radiations. J Oncol Res., 2018, 1(1): 1-20.

[177] A. Heidari. Use of Molecular Enzymes in the Treatment of Chronic Disorders. Canc Oncol Open Access J., 2018, 1(1): 12-15.

[178] A. Heidari. Vibrational Biospectroscopic Study and Chemical Structure Analysis of Unsaturated Polyamides Nanoparticles as Anti-Cancer Polymeric Nanomedicines Using Synchrotron Radiation. International Journal of Advanced Chemistry, 2018, 6(2): 167-189.

[179] A. Heidari. Adamantane, Irene, Naftazone and Pyridine-Enhanced Precatalyst Preparation Stabilization and Initiation (PEPPSI) Nano Molecules. Madridge J Nov Drug Res., 2018, 2(1): 61-67.

[180] A. Heidari. Heteronuclear Single-Quantum Correlation Spectroscopy (HSQC) and Heteronuclear Multiple-Bond Correlation Spectroscopy (HMBC) Comparative Study on Malignant and Benign Human Cancer Cells and Tissues with the Passage of Time under Synchrotron Radiation. Madridge J Nov Drug Res., 2018, 2(1): 68-74.

[181] A. Heidari, R. Gobato. A Novel Approach to Reduce Toxicities and to Improve Bioavailabilities of DNA/RNA of Human Cancer Cells-Containing Cocaine (Coke), Lysergide (Lysergic Acid Diethyl Amide or LSD), Δ□-Tetrahydrocannabinol (THC) [(-)-trans-Δ□-Tetrahydrocannabinol], Theobromine (Xantheose), Caffeine, Aspartame (APM) (NutraSweet) and Zidovudine (ZDV) [Azidothy-

DOI: https://doi.org/10.30564/ssid.v1i2.1827

midine (AZT)] as Anti-Cancer Nano Drugs by Coassembly of Dual Anti-Cancer Nano Drugs to Inhibit DNA/RNA of Human Cancer Cells Drug Resistance. Parana Journal of Science and Education, 2018, 4(6): 1-17.

[182] A. Heidari, R. Gobato. Ultraviolet Photoelectron Spectroscopy (UPS) and Ultraviolet-Visible (UV-Vis) Spectroscopy Comparative Study on Malignant and Benign Human Cancer Cells and Tissues with the Passage of Time under Synchrotron Radiation. Parana Journal of Science and Education, 2018, 4(6): 18-33.

[183] R. Gobato, A. Heidari, A. Mitra. The Creation of $C_{13}H_{20}BeLi_2SeSi$. The Proposal of a Bio-Inorganic Molecule, Using Ab Initio Methods for the Genesis of a Nano Membrane. Arc Org Inorg Chem Sci., 2018, 3(4). AOICS.MS.ID.000167.

[184] R. Gobato, A. Heidari, A. Mitra. Using the Quantum Chemistry for Genesis of a Nano Biomembrane with a Combination of the Elements Be, Li, Se, Si, C and H. ResearchGate, 2018. See discussions, stats, and author profiles for this publication at: https://www.researchgate.net/publication/326201181.

[185] R. Gobato, A. Heidari. Using the Quantum Chemistry for Genesis of a Nano Biomembrane with a Combination of the Elements Be, Li, Se, Si, C and H. J Nanomed Res., 2018, 7(4): 241-252.

[186] A. Heidari. Bastadins and Bastaranes-Enhanced Precatalyst Preparation Stabilization and Initiation (EPPSI) Nano Molecules. Glob Imaging Insights, 2018, 3(4): 1-7.

[187] A. Heidari. Fucitol, Pterodactyladiene, DEAD or DEADCAT (DiEthyl AzoDiCArboxylaTe), Skatole, the NanoPutians, Thebacon, Pikachurin, Tie Fighter, Spermidine and Mirasorvone Nano Molecules Incorporation into the Nano Polymeric Matrix (NPM) by Immersion of the Nano Polymeric Modified Electrode (NPME) as Molecular Enzymes and Drug Targets for Human Cancer Cells, Tissues and Tumors Treatment under Synchrotron and Synchrocyclotron Radiations. Glob Imaging Insights, 2018, 3(4): 1-8.

[188] E. Dadvar, A. Heidari. A Review on Separation Techniques of Graphene Oxide (GO)/Base on Hybrid Polymer Membranes for Eradication of Dyes and Oil Compounds: Recent Progress in Graphene Oxide (GO)/Base on Polymer Membranes-Related Nanotechnologies. Clin Med Rev Case Rep., 2018, 5: 228.

[189] A. Heidari, R. Gobato. First-Time Simulation of Deoxyuridine Monophosphate (dUMP) (Deoxyuridylic Acid or Deoxyuridylate) and Vomitoxin (Deoxynivalenol (DON)) ((3α,7α)-3,7,15-Trihydroxy-12,13-Epoxytrichothec-9-En-8-One)-Enhanced Precatalyst Preparation Stabilization and Initiation (EPPSI) Nano Molecules Incorporation into the Nano Polymeric Matrix (NPM) by Immersion of the Nano Polymeric Modified Electrode (NPME) as Molecular Enzymes and Drug Targets for Human Cancer Cells, Tissues and Tumors Treatment under Synchrotron and Synchrocyclotron Radiations. Parana Journal of Science and Education, 2018, 4(6): 46-67.

[190] A. Heidari. Buckminsterfullerene (Fullerene), Bullvalene, Dickite and Josiphos Ligands Nano Molecules Incorporation into the Nano Polymeric Matrix (NPM) by Immersion of the Nano Polymeric Modified Electrode (NPME) as Molecular Enzymes and Drug Targets for Human Hematology and Thromboembolic Diseases Prevention, Diagnosis and Treatment under Synchrotron and Synchrocyclotron Radiations. Glob Imaging Insights, 2018, 3(4): 1-7.

[191] A. Heidari. Fluctuation X-Ray Scattering (FXS) and Wide-Angle X-Ray Scattering (WAXS) Comparative Study on Malignant and Benign Human Cancer Cells and Tissues under Synchrotron Radiation. Glob Imaging Insights, 2018, 3(4): 1-7.

[192] A. Heidari. A Novel Approach to Correlation Spectroscopy (COSY), Exclusive Correlation Spectroscopy (ECOSY), Total Correlation Spectroscopy (TOCSY), Incredible Natural-Abundance Double-Quantum Transfer Experiment (INADEQUATE), Heteronuclear Single-Quantum Correlation Spectroscopy (HSQC), Heteronuclear Multiple-Bond Correlation Spectroscopy (HMBC), Nuclear Overhauser Effect Spectroscopy (NOESY) and Rotating Frame Nuclear Overhauser Effect Spectroscopy (ROESY) Comparative Study on Malignant and Benign Human Cancer Cells and Tissues under Synchrotron Radiation. Glob Imaging Insights, 2018, 3(5): 1-9.

[193] A. Heidari. Terphenyl-Based Reversible Receptor with Rhodamine, Rhodamine-Based Molecular Probe, Rhodamine-Based Using the Spirolactam Ring Opening, Rhodamine B with Ferrocene Substituent, Calix[4]Arene-Based Receptor, Thioether + Aniline-Derived Ligand Framework Linked to a Fluorescein Platform, Mercuryfluor-1 (Flourescent Probe), N,N'-Dibenzyl-1,4,10,13-Tetraoxa-7,16-Diazacyclooctadecane and Terphenyl-Based Reversible Receptor with Pyrene and Quinoline as the Fluorophores-Enhanced Precatalyst Preparation Stabilization and Initiation (EPPSI) Nano Molecules. Glob Imaging Insights, 2018, 3(5): 1-9.

[194] A. Heidari. Small-Angle X-Ray Scattering (SAXS),

 DOI: https://doi.org/10.30564/ssid.v1i2.1827

Ultra-Small Angle X-Ray Scattering (USAXS), Fluctuation X-Ray Scattering (FXS), Wide-Angle X-Ray Scattering (WAXS), Grazing-Incidence Small-Angle X-Ray Scattering (GISAXS), Grazing-Incidence Wide-Angle X-Ray Scattering (GIWAXS), Small-Angle Neutron Scattering (SANS), Grazing-Incidence Small-Angle Neutron Scattering (GISANS), X-Ray Diffraction (XRD), Powder X-Ray Diffraction (PXRD), Wide-Angle X-Ray Diffraction (WAXD), Grazing- Incidence X-Ray Diffraction (GIXD) and Energy-Dispersive X-Ray Diffraction (EDXRD) Comparative Study on Malignant and Benign Human Cancer Cells and Tissues under Synchrotron Radiation. Glob Imaging Insights, 2018, 3(5): 1-10.

[195] A. Heidari. Nuclear Resonant Inelastic X-Ray Scattering Spectroscopy (NRIXSS) and Nuclear Resonance Vibrational Spectroscopy (NRVS) Comparative Study on Malignant and Benign Human Cancer Cells and Tissues under Synchrotron Radiation. Glob Imaging Insights, 2018, 3(5): 1-7.

[196] A. Heidari. Small-Angle X-Ray Scattering (SAXS) and Ultra-Small Angle X-Ray Scattering (USAXS) Comparative Study on Malignant and Benign Human Cancer Cells and Tissues under Synchrotron Radiation. Glob Imaging Insights, 2018, 3(5): 1-7.

[197] A. Heidari. Curious Chloride ($CmCl_3$) and Titanic Chloride ($TiCl_4$)-Enhanced Precatalyst Preparation Stabilization and Initiation (EPPSI) Nano Molecules for Cancer Treatment and Cellular Therapeutics. J. Cancer Research and Therapeutic Interventions, 2018, 1(1): 01-10.

[198] R. Gobato, M. R. R. Gobato, A. Heidari, A. Mitra. Spectroscopy and Dipole Moment of the Molecule $C_{13}H_{20}BeLi_2SeSi$ via Quantum Chemistry Using Ab Initio, Hartree-Fock Method in the Base Set CC-pVTZ and 6-311G**(3df, 3pd). Arc Org Inorg Chem Sci., 2018, 3(5): 402-409.

[199] A. Heidari. C_{60} and C_{70}-Encapsulating Carbon Nanotubes Incorporation into the Nano Polymeric Matrix (NPM) by Immersion of the Nano Polymeric Modified Electrode (NPME) as Molecular Enzymes and Drug Targets for Human Cancer Cells, Tissues and Tumors Treatment under Synchrotron and Synchrocyclotron Radiations. Integr Mol Med, 2018, 5(3): 1-8.

[200] A. Heidari. Two-Dimensional (2D) ^{1}H or Proton NMR, ^{13}C NMR, ^{15}N NMR and ^{31}P NMR Spectroscopy Comparative Study on Malignant and Benign Human Cancer Cells and Tissues under Synchrotron Radiation with the Passage of Time. Glob Imaging Insights, 2018, 3(6): 1-8.

[201] A. Heidari. FT-Raman Spectroscopy, Coherent Anti-Stokes Raman Spectroscopy (CARS) and Raman Optical Activity Spectroscopy (ROAS) Comparative Study on Malignant and Benign Human Cancer Cells and Tissues with the Passage of Time under Synchrotron Radiation. Glob Imaging Insights, 2018, 3(6): 1-8.

[202] A. Heidari. A Modern and Comprehensive Investigation of Inelastic Electron Tunneling Spectroscopy (IETS) and Scanning Tunneling Spectroscopy on Malignant and Benign Human Cancer Cells, Tissues and Tumors through Optimizing Synchrotron Microbeam Radiotherapy for Human Cancer Treatments and Diagnostics: An Experimental Biospectroscopic Comparative Study. Glob Imaging Insights, 2018, 3(6): 1-8.

[203] A. Heidari. A Hypertension Approach to Thermal Infrared Spectroscopy and Photothermal Infrared Spectroscopy Comparative Study on Malignant and Benign Human Cancer Cells and Tissues under Synchrotron Radiation with the Passage of Time. Glob Imaging Insights, 2018, 3(6): 1-8.

[204] A. Heidari. Incredible Natural-Abundance Double-Quantum Transfer Experiment (INADEQUATE), Nuclear Overhauser Effect Spectroscopy (NOESY) and Rotating Frame Nuclear Overhauser Effect Spectroscopy (ROESY) Comparative Study on Malignant and Benign Human Cancer Cells and Tissues under Synchrotron Radiation. Glob Imaging Insights, 2018, 3 (6): 1-8.

[205] A. Heidari. 2-Amino-9-((1S, 3R, 4R)-4-Hydroxy-3-(Hydroxymethyl)-2-Methylenecyclopentyl)-1H-Purin-6(9H)-One, 2-Amino-9-((1R, 3R, 4R)-4-Hydroxy-3-(Hydroxymethyl)-2-Methylenecyclopentyl)-1H-Purin-6(9H)-One, 2-Amino-9-((1R, 3R, 4S)-4-Hydroxy-3-(Hydroxymethyl)-2-Methylenecyclopentyl)-1H-Purin-6(9H)-One and 2-Amino-9-((1S, 3R, 4S)-4-Hydroxy-3-(Hydroxymethyl)-2-Methylenecyclopentyl)-1H-Purin-6(9H)-One-Enhanced Precatalyst Preparation Stabilization and Initiation Nano Molecules. Glob Imaging Insights, 2018, 3(6): 1-9.

[206] R. Gobato, M. R. R. Gobato, A. Heidari, A. Mitra. Spectroscopy and Dipole Moment of the Molecule $C_{13}H_{20}BeLi_2SeSi$ via Quantum Chemistry Using Ab Initio, Hartree-Fock Method in the Base Set CC-pVTZ and 6-311G**(3df, 3pd). American Journal of Quantum Chemistry and Molecular Spectroscopy, 2018, 2(1): 9-17.

[207] A. Heidari. Production of Electrochemiluminescence (ECL) Biosensor Using Os-Pd/HfC Nanocomposites for Detecting and Tracking of Human Gastroentero-

DOI: https://doi.org/10.30564/ssid.v1i2.1827

logical Cancer Cells, Tissues and Tumors. Int J Med Nano Res., 2018, 5(1): 022-034.

[208] A. Heidari. Enhancing the Raman Scattering for Diagnosis and Treatment of Human Cancer Cells, Tissues and Tumors Using Cadmium Oxide (CdO) Nanoparticles. J Toxicol Risk Assess, 2018, 4(1): 012-025.

[209] A. Heidari. Human Malignant and Benign Human Cancer Cells and Tissues Biospectroscopic Analysis under Synchrotron Radiation Using Anti-Cancer Nano Drugs Delivery. Integr Mol Med, 2018, 5(5): 1-13.

[210] A. Heidari. Analogous Nano Compounds of the Form $M(C_8H_8)_2$ Exist for M = (Nd, Tb, Pu, Pa, Np, Th, and Yb)-Enhanced Precatalyst Preparation Stabilization and Initiation (EPPSI) Nano Molecules. Integr Mol Med, 2018, 5(5): 1-8.

[211] A. Heidari. Hadron Spectroscopy, Baryon Spectroscopy and Meson Spectroscopy Comparative Study on Malignant and Benign Human Cancer Cells and Tissues under Synchrotron Radiation. Integr Mol Med, 2018, 5(5): 1-8.

[212] R. Gobato, M. R. R. Gobato, A. Heidari. Raman Spectroscopy Study of the Nano Molecule $C_{13}H_{20}BeLi_2SeSi$ Using ab initio and Hartree-Fock Methods in the Basis Set CC-pVTZ and 6-311G** (3df, 3pd). International Journal of Advanced Engineering and Science, 2019, 7(1): 14-35.

[213] A. Heidari, R. Gobato. Evaluating the Effect of Anti-Cancer Nano Drugs Dosage and Reduced Leukemia and Polycythemia Vera Levels on Trend of the Human Blood and Bone Marrow Cancers under Synchrotron Radiation. Trends in Res., 2019, 2(1): 1-8.

[214] A. Heidari, R. Gobato. Assessing the Variety of Synchrotron, Synchrocyclotron and LASER Radiations and Their Roles and Applications in Human Cancer Cells, Tissues and Tumors Diagnosis and Treatment. Trends in Res., 2019, 2(1): 1-8.

[215] A. Heidari, R. Gobato. Pros and Cons Controversy on Malignant Human Cancer Cells, Tissues and Tumors Transformation Process to Benign Human Cancer Cells, Tissues and Tumors. Trends in Res., 2019, 2(1): 1-8.

[216] A. Heidari, R. Gobato. Three-Dimensional (3D) Simulations of Human Cancer Cells, Tissues and Tumors for Using in Human Cancer Cells, Tissues and Tumors Diagnosis and Treatment as a Powerful Tool in Human Cancer Cells, Tissues and Tumors Research and Anti-Cancer Nano Drugs Sensitivity and Delivery Area Discovery and Evaluation. Trends in Res., 2019, 2(1): 1-8.

[217] A. Heidari, R. Gobato. Investigation of Energy Production by Synchrotron, Synchrocyclotron and LASER Radiations in Human Cancer Cells, Tissues and Tumors and Evaluation of Their Effective on Human Cancer Cells, Tissues and Tumors Treatment Trend. Trends in Res., 2019, 2(1): 1-8.

[218] A. Heidari, R. Gobato. High-Resolution Mapping of DNA/RNA Hypermethylation and Hypomethylation Process in Human Cancer Cells, Tissues and Tumors under Synchrotron Radiation. Trends in Res., 2019, 2(2): 1-9.

[219] A. Heidari. A Novel and Comprehensive Study on Manufacturing and Fabrication Nanoparticles Methods and Techniques for Processing Cadmium Oxide (CdO) Nanoparticles Colloidal Solution. Glob Imaging Insights, 2019, 4(1): 1-8.

[220] A. Heidari. A Combined Experimental and Computational Study on the Catalytic Effect of Aluminum Nitride Nanocrystal (AlN) on the Polymerization of Benzene, Naphthalene, Anthracene, Phenanthrene, Chrysene and Tetracene. Glob Imaging Insights, 2019, 4(1): 1-8.

[221] A. Heidari. Novel Experimental and Three-Dimensional (3D) Multiphysics Computational Framework of Michaelis-Menten Kinetics for Catalyst Processes Innovation, Characterization and Carrier Applications. Glob Imaging Insights, 2019, 4(1): 1-8.

[222] A. Heidari. The Hydrolysis Constants of Copper (I) (Cu^+) and Copper (II) (Cu^{2+}) in Aqueous Solution as a Function of pH Using a Combination of pH Measurement and Biospectroscopic Methods and Techniques. Glob Imaging Insights, 2019, 4(1): 1-8.

[223] A. Heidari. Vibrational Biospectroscopic Study of Ginormous Virus-Sized Macromolecule and Polypeptide Macromolecule as Mega Macromolecules Using Attenuated Total Reflectance-Fourier Transform Infrared (ATR-FTIR) Spectroscopy and Mathematica 11.3. Glob Imaging Insights, 2019, 4(1): 1-8.

[224] A. Heidari. Three-Dimensional (3D) Imaging Spectroscopy of Carcinoma, Sarcoma, Leukemia, Lymphoma, Multiple Myeloma, Melanoma, Brain and Spinal Cord Tumors, Germ Cell Tumors, Neuroendocrine Tumors and Carcinoid Tumors under Synchrotron Radiation. Glob Imaging Insights, 2019, 4(1): 1-9.

[225] R. Gobato, M. R. R. Gobato, A. Heidari. Storm Vortex in the Center of Paraná State on June 6, 2017: A Case Study. Sumerianz Journal of Scientific Research, 2019, 2(2): 24-31.

[226] R. Gobato, M. R. R. Gobato, A. Heidari. Attenuated Total Reflection-Fourier Transform Infrared (ATR-FTIR) Spectroscopy Study of the Nano Molecule

 DOI: https://doi.org/10.30564/ssid.v1i2.1827

$C_{13}H_{20}BeLi_2SeSi$ Using ab initio and Hartree-Fock Methods in the Basis Set RHF/CC-pVTZ and RHF/6-311G** (3df, 3pd): An Experimental Challenge to Chemists. Chemistry Reports, 2019, 2(1): 1-26.

[227] A. Heidari. Three-Dimensional (3D) Imaging Spectroscopy of Carcinoma, Sarcoma, Leukemia, Lymphoma, Multiple Myeloma, Melanoma, Brain and Spinal Cord Tumors, Germ Cell Tumors, Neuroendocrine Tumors and Carcinoid Tumors under Synchrocyclotron Radiation. Res Adv Biomed Sci Technol., 2019, 1(1): 01-17.

[228] R. Gobato, M. R. R. Gobato, A. Heidari, A. Mitra. New Nano-Molecule Kurumi-$C_{13}H_{20}BeLi_2SeSi$/$C_{13}H_{19}BeLi_2SeSi$, and Raman Spectroscopy Using ab initio, Hartree-Fock Method in the Base Set CC-pVTZ and 6-311G** (3df, 3pd). J Anal Pharm Res., 2019, 8 (1): 1-6.

[229] A. Heidari, J. Esposito, A. Caissutti. The Importance of Attenuated Total Reflectance Fourier Transform Infrared (ATR-FTIR) and Raman Biospectroscopy of Single-Walled Carbon Nanotubes (SWCNT) and Multi-Walled Carbon Nanotubes (MWCNT) in Interpreting Infrared and Raman Spectra of Human Cancer Cells, Tissues and Tumors. Oncogen, 2019, 2(2): 1-21.

[230] A. Heidari. Mechanism of Action and Their Side Effects at a Glance Prevention, Treatment and Management of Immune System and Human Cancer Nano Chemotherapy. Nanosci Technol., 2019, 6(1): 1-4.

[231] A. Heidari, J. Esposito, A. Caissutti. The Quantum Entanglement Dynamics Induced by Non-Linear Interaction between a Moving Nano Molecule and a Two-Mode Field with Two-Photon Transitions Using Reduced Von Neumann Entropy and Jaynes-Cummings Model for Human Cancer Cells, Tissues and Tumors Diagnosis. Int J Crit Care Emerg Med., 2019, 5 (2): 071-084.

[232] A. Heidari, J. Esposito, A. Caissutti. Palytoxin Time-Resolved Absorption and Resonance FT-IR and Raman Biospectroscopy and Density Functional Theory (DFT) Investigation of Vibronic-Mode Coupling Structure in Vibrational Spectra Analysis. J Pharm Drug Res., 2019, 3(1): 150-170.

[233] A. Heidari, J. Esposito, A. Caissutti. Aplysiatoxin Time-Resolved Absorption and Resonance FT-IR and Raman Biospectroscopy and Density Functional Theory (DFT) Investigation of Vibronic-Mode Coupling Structure in Vibrational Spectra Analysis. J Chem Sci Eng., 2019, 2(2): 70-89.

[234] R. Gobato, M. R. R. Gobato, A. Heidari, A. Mitra. Spectroscopy and Dipole Moment of the Molecule $C_{13}H_{20}BeLi_2SeSi$ via Quantum Chemistry Using Ab initio, Hartree-Fock Method in the Base Set CC-pVTZ and 6-311G** (3df, 3pd). American Journal of Quantum Chemistry and Molecular Spectroscopy, 2018, 2(1): 9-17.

[235] A. Heidari, J. Esposito, A. Caissutti. Cyanotoxin Time-Resolved Absorption and Resonance FT-IR and Raman Biospectroscopy and Density Functional Theory (DFT) Investigation of Vibronic-Mode Coupling Structure in Vibrational Spectra Analysis. Br J Med Health Res., 2019, 6(04): 21-60.

[236] A. Heidari. Potential and Theranostics Applications of Novel Anti-Cancer Nano Drugs Delivery Systems in Preparing for Clinical Trials of Synchrotron Microbeam Radiation Therapy (SMRT) and Synchrotron Stereotactic Radiotherapy (SSRT) for Treatment of Human Cancer Cells, Tissues and Tumors Using Image Guided Synchrotron Radiotherapy (IGSR). Ann Nanosci Nanotechnol., 2019, 3(1): 1006-1019.

[237] A. Heidari, J. Esposito, A. Caissutti. Study of Anti-Cancer Properties of Thin Layers of Cadmium Oxide (CdO) Nanostructure. Int J Analyt Bioanalyt Methods, 2019, 1(1): 003-022.

[238] A. Heidari, J. Esposito, A. Caissutti. Alpha-Conotoxin, Omega-Conotoxin and Mu-Conotoxin Time-Resolved Absorption and Resonance FT-IR and Raman Biospectroscopy and Density Functional Theory (DFT) Investigation of Vibronic-Mode Coupling Structure in Vibrational Spectra Analysis. International Journal of Advanced Chemistry, 2019, 7(1): 52-66.

[239] A. Heidari. Clinical and Medical Pros and Cons of Human Cancer Cells' Enzymotherapy, Immunotherapy, Chemotherapy, Radiotherapy, Hormone Therapy and Targeted Therapy Process under Synchrotron Radiation: A Case Study on Mechanism of Action and Their Side Effects. Parana Journal of Science and Education (PJSE), 2019, 5(3): 1-23.

[240] A. Heidari. The Importance of the Power in CMOS Inverter Circuit of Synchrotron and Synchrocyclotron Radiations Using 50 (nm) and 100 (nm) Technologies and Reducing the Voltage of Power Supply. Radiother Oncol Int., 2019, 1(1): 1002-1015.

[241] A. Heidari, J. Esposito, A. Caissutti. The Importance of Quantum Hydrodynamics (QHD) Approach to Single-Walled Carbon Nanotubes (SWCNT) and Multi-Walled Carbon Nanotubes (MWCNT) in Genetic Science. SCIOL Genet Sci., 2019, 2(1): 113-129.

[242] A. Heidari, J. Esposito, A. Caissutti. Anatoxin-a and Anatoxin-a(s) Time-Resolved Absorption and Resonance FT-IR and Raman Biospectroscopy and

DOI: https://doi.org/10.30564/ssid.v1i2.1827

Density Functional Theory (DFT) Investigation of Vibronic-Mode Coupling Structure in Vibrational Spectra Analysis. Saudi J Biomed Res., 2019, 4(4): 174-194.

[243] R. Gobato, M. R. R. Gobato, A. Heidari. Evidence of Tornado Storm Hit the Counties of Rio Branco do Ivaí and Rosario de Ivaí, Southern Brazil. Sci Lett, 2019, 7(1): 32-40.

[244] M. Jeyaraj, V. Mahalingam, A. Indhuleka, P. Sennu, M. S. Ho, A. Heidari. Chemical Analysis of Surface Water Quality of River Noyyal Connected Tank in Tirupur District, Tamil Nadu, India. Water and Energy International, 2019, 62r(1): 63-68.

[245] A. Heidari, J. Esposito, A. Caissutti. 6-Methoxy-8-[[6-Methoxy-8-[[6-Methoxy-2-Methyl-1-(2-Methylpropyl)-3,4- Dihydro-1H-Isoquinolin-7-yl] Oxy]-2-Methyl-1-(2-Methylpropyl)-3,4-Dihydro-1H-Isoquinolin-7-yl]Oxy]-2-Methyl-1-(2-Methylpropyl)-3,4-Dihydro-1H-Isoquinolin-7-ol Time-Resolved Absorption and Resonance FT-IR and Raman Biospectroscopy and Density Functional Theory (DFT) Investigation of Vibronic-Mode Coupling Structure in Vibrational Spectra Analysis. J. Adv. Phys. Chem., 2019, 1(1): 1-6.

[246] A. Heidari, J. Esposito, A. Caissutti. Shiga Toxin and Shiga-Like Toxin (SLT) Time-Resolved Absorption and Resonance FT-IR and Raman Biospectroscopy and Density Functional Theory (DFT) Investigation of Vibronic-Mode Coupling Structure in Vibrational Spectra Analysis. Annal Biostat & Biomed Appli., 2019, 2(3): 1-4.

[247] A. Heidari, J. Esposito, A. Caissutti. Alpha-Bungarotoxin, Beta-Bungarotoxin and Kappa-Bungarotoxin Time-Resolved Absorption and Resonance FT-IR and Raman Biospectroscopy and Density Functional Theory (DFT) Investigation of Vibronic-Mode Coupling Structure in Vibrational Spectra Analysis. Archives of Pharmacology and Pharmaceutical Sciences, ReDelve, 2019, 2019(01): 1-24.

[248] A. Heidari, J. Esposito, A. Caissutti. Okadaic Acid Time-Resolved Absorption and Resonance FT-IR and Raman Biospectroscopy and Density Functional Theory (DFT) Investigation of Vibronic-Mode Coupling Structure in Vibrational Spectra Analysis. Int J Analyt Bioanalyt Methods, 2019, 1(1): 1-19.

[249] A. Heidari. Investigation of the Processes of Absorption, Distribution, Metabolism and Elimination (ADME) as Vital and Important Factors for Modulating Drug Action and Toxicity. Open Access J Oncol., 2019, 2(1): 180010-180012.

[250] A. Heidari, J. Esposito, A. Caissutti. Pertussis Toxin Time-Resolved Absorption and Resonance FT-IR and Raman Biospectroscopy and Density Functional Theory (DFT) Investigation of Vibronic-Mode Coupling Structure in Vibrational Spectra Analysis. Chemistry Reports, 2019, 1(2): 1-5.

[251] R. Gobato, M. R. R. Gobato, A. Heidari. Rhodochrosite as Crystal Oscillator. Am J Biomed Sci & Res., 2019, 3(2): 187.

[252] A. Heidari, J. Esposito, A. Caissutti. Tetrodotoxin (TTX) Time-Resolved Absorption and Resonance FT-IR and Raman Biospectroscopy and Density Functional Theory (DFT) Investigation of Vibronic-Mode Coupling Structure in Vibrational Spectra Analysis. Journal of New Developments in Chemistry, 2019, 2(3): 26-48.

[253] A. Heidari, J. Esposito, A. Caissutti. The Importance of Analysis of Vibronic-Mode Coupling Structure in Vibrational Spectra of Supramolecular Aggregates of (CA*M) Cyanuric Acid (CA) and Melamine (M) beyond the Franck-Condon Approximation. Journal of Clinical and Medical Images, 2019, 2(2): 1-20.

[254] A. Heidari, J. Esposito, A. Caissutti. Microcystin-LR Time-Resolved Absorption and Resonance FT-IR and Raman Biospectroscopy and Density Functional Theory (DFT) Investigation of Vibronic-Mode Coupling Structure in Vibrational Spectra Analysis. Malaysian Journal of Chemistry, 2019, 21(1): 70-95.

[255] A. Heidari, J. Esposito, A. Caissutti. Botulinum Toxin Time-Resolved Absorption and Resonance FT-IR and Raman Biospectroscopy and Density Functional Theory (DFT) Investigation of Vibronic-Mode Coupling Structure in Vibrational Spectra Analysis. Journal of Mechanical Design and Vibration, 2019, 7(1): 1-15.

[256] A. Heidari, J. Esposito, A. Caissutti. Domoic Acid (DA) Time-Resolved Absorption and Resonance FT-IR and Raman Biospectroscopy and Density Functional Theory (DFT) Investigation of Vibronic-Mode Coupling Structure in Vibrational Spectra Analysis. Cientific Clinical Oncology Journal, 2019, 1(2): 03-07.

[257] A. Heidari, J. Esposito, A. Caissutti. Surugatoxin (SGTX) Time-Resolved Absorption and Resonance FT-IR and Raman Biospectroscopy and Density Functional Theory (DFT) Investigation of Vibronic-Mode Coupling Structure in Vibrational Spectra Analysis. Cientific Clinical Oncology Journal, 2019, 1(2): 14-18.

[258] A. Heidari, J. Esposito, A. Caissutti. Decarbamoylsaxitoxin Time-Resolved Absorption and Resonance FT-IR and Raman Biospectroscopy and Density Functional Theory (DFT) Investigation of Vibronic-Mode Coupling Structure in Vibrational Spectra

 DOI: https://doi.org/10.30564/ssid.v1i2.1827

Analysis. Cientific Clinical Oncology Journal, 2019, 1(2): 19-23.

[259] A. Heidari, J. Esposito, A. Caissutti. Gonyautoxin (GTX) Time-Resolved Absorption and Resonance FT-IR and Raman Biospectroscopy and Density Functional Theory (DFT) Investigation of Vibronic-Mode Coupling Structure in Vibrational Spectra Analysis. Cientific Clinical Oncology Journal, 2019, 1(2): 24-28.

[260] A. Heidari, J. Esposito, A. Caissutti. Hislrionicotoxin Time-Resolved Absorption and Resonance FT-IR and Raman Biospectroscopy and Density Functional Theory (DFT) Investigation of Vibronic-Mode Coupling Structure in Vibrational Spectra Analysis. Cientific Drug Delivery Research, 2019, 1(1): 01-06.

[261] A. Heidari, J. Esposito, A. Caissutti. Dihydrokainic Acid Time-Resolved Absorption and Resonance FT-IR and Raman Biospectroscopy and Density Functional Theory (DFT) Investigation of Vibronic-Mode Coupling Structure in Vibrational Spectra Analysis. Cientific Drug Delivery Research, 2019, 1(1): 07-12.

[262] A. Heidari, J. Esposito, A. Caissutti. Aflatoxin B1 (AFB1), B2 (AFB2), G1 (AFG1), G2 (AFG2), M1 (AFM1), M2 (AFM2), Q1 (AFQ1) and P1 (AFP1) Time-Resolved Absorption and Resonance FT-IR and Raman Biospectroscopy and Density Functional Theory (DFT) Investigation of Vibronic-Mode Coupling Structure in Vibrational Spectra Analysis. Cientific Drug Delivery Research, 2019, 1(1): 25-32.

[263] A. Heidari, J. Esposito, A. Caissutti. Mycotoxin Time-Resolved Absorption and Resonance FT-IR and Raman Biospectroscopy and Density Functional Theory (DFT) Investigation of Vibronic-Mode Coupling Structure in Vibrational Spectra Analysis. Cientific Drug Delivery Research, 2019, 1(1): 13-18.

[264] A. Heidari, J. Esposito, A. Caissutti. Bufotoxin Time-Resolved Absorption and Resonance FT-IR and Raman Biospectroscopy and Density Functional Theory (DFT) Investigation of Vibronic-Mode Coupling Structure in Vibrational Spectra Analysis. Cientific Drug Delivery Research, 2019, 1(1): 19-24.

[265] A. Heidari, J. Esposito, A. Caissutti. Kainic Acid (Kainite) Time-Resolved Absorption and Resonance FT-IR and Raman Biospectroscopy and Density Functional Theory (DFT) Investigation of Vibronic-Mode Coupling Structure in Vibrational Spectra Analysis. Cientific Journal of Neurology, 2019, 1(2): 02-07.

[266] A. Heidari, J. Esposito, A. Caissutti. Nereistoxin Time-Resolved Absorption and Resonance FT-IR and Raman Biospectroscopy and Density Functional Theory (DFT) Investigation of Vibronic-Mode Coupling Structure in Vibrational Spectra Analysis. Cientific Journal of Neurology, 2019, 1(2): 19-24.

[267] A. Heidari, J. Esposito, A. Caissutti. Spider Toxin and Raventoxin Time-Resolved Absorption and Resonance FT-IR and Raman Biospectroscopy and Density Functional Theory (DFT) Investigation of Vibronic-Mode Coupling Structure in Vibrational Spectra Analysis. Parana Journal of Science and Education, 2019, 5(4): 1-28.

[268] A. Heidari, J. Esposito, A. Caissutti. Ochratoxin A, Ochratoxin B, Ochratoxin C, Ochratoxin α and Ochratoxin TA Time-Resolved Absorption and Resonance FT-IR and Raman Biospectroscopy and Density Functional Theory (DFT) Investigation of Vibronic-Mode Coupling Structure in Vibrational Spectra Analysis. Cientific Drug Delivery Research, 2019, 1(2): 03-10.

[269] A. Heidari, J. Esposito, A. Caissutti. Brevetoxin A and B Time-Resolved Absorption and Resonance FT-IR and Raman Biospectroscopy and Density Functional Theory (DFT) Investigation of Vibronic-Mode Coupling Structure in Vibrational Spectra Analysis. Cientific Drug Delivery Research, 2019, 1(2): 11-16.

[270] A. Heidari, J. Esposito, A. Caissutti. Lyngbyatoxin-a Time-Resolved Absorption and Resonance FT-IR and Raman Biospectroscopy and Density Functional Theory (DFT) Investigation of Vibronic-Mode Coupling Structure in Vibrational Spectra Analysis. Cientific Drug Delivery Research, 2019, 1(2): 23-28.

[271] A. Heidari, J. Esposito, A. Caissutti. Balraechotoxin (BTX) Time-Resolved Absorption and Resonance FT-IR and Raman Biospectroscopy and Density Functional Theory (DFT) Investigation of Vibronic-Mode Coupling Structure in Vibrational Spectra Analysis. Cientific Journal of Neurology, 2019, 1(3): 01-05.

[272] A. Heidari, J. Esposito, A. Caissutti. Hanatoxin Time-Resolved Absorption and Resonance FT-IR and Raman Biospectroscopy and Density Functional Theory (DFT) Investigation of Vibronic-Mode Coupling Structure in Vibrational Spectra Analysis. Int. J. Pharm. Sci. Rev. Res., 2019, 57(1): 21-32.

[273] A. Heidari, J. Esposito, A. Caissutti. Neurotoxin and Alpha-Neurotoxin Time-Resolved Absorption and Resonance FT-IR and Raman Biospectroscopy and Density Functional Theory (DFT) Investigation of Vibronic-Mode Coupling Structure in Vibrational Spectra Analysis. J Biomed Sci & Res., 2019, 3(6): 550-563.

[274] A. Heidari, J. Esposito, A. Caissutti. Antillatoxin

DOI: https://doi.org/10.30564/ssid.v1i2.1827

(ATX) Time-Resolved Absorption and Resonance FT-IR and Raman Biospectroscopy and Density Functional Theory (DFT) Investigation of Vibronic-Mode Coupling Structure. American Journal of Optics and Photonics, 2019, 7(1): 18-27.

[275] R. Gobato, M. R. R. Gobato, A. Heidari. Calculation by UFF Method of Frequencies and Vibrational Temperatures of the Unit Cell of the Rhodochrosite Crystal. International Journal of Advanced Chemistry, 2019, 7(2): 77-81.

[276] A. Heidari, J. Esposito, A. Caissutti. Analysis of Vibronic-Mode Coupling Structure in Vibrational Spectra of Fuzeon as a 36 Amino Acid Peptide for HIV Therapy beyond the Multi-Dimensional Franck-Condon Integrals Approximation. International Journal of Advanced Chemistry, 2019, 7(2): 82-96.

[277] A. Heidari, J. Esposito, A. Caissutti. Debromoaplysiatoxin Time-Resolved Absorption and Resonance FT-IR and Raman Biospectroscopy and Density Functional Theory (DFT) Investigation of Vibronic-Mode Coupling Structure in Vibrational Spectra Analysis. Applied Chemistry, 2019, 2(1): 17-54.

[278] A. Heidari, J. Esposito, A. Caissutti. Enterotoxin Time-Resolved Absorption and Resonance FT-IR and Raman Biospectroscopy and Density Functional Theory (DFT) Investigation of Vibronic-Mode Coupling Structure in Vibrational Spectra Analysis. JRL J Sci Technol., 2019, 2(1001): 1-16.

[279] R. Gobato, M. R. R. Gobato, A. Heidari, A. Mitra. Rhodochrosite Optical Indicatrix. Peer Res Nest, 2019, 1(3): 1-2.

[280] A. Heidari, J. Esposito, A. Caissutti. Anthrax Toxin Time-Resolved Absorption and Resonance FT-IR and Raman Biospectroscopy and Density Functional Theory (DFT) Investigation of Vibronic-Mode Coupling Structure in Vibrational Spectra Analysis. Research & Reviews: Journal of Computational Biology, 2019, 8(2): 23-51.

[281] A. Heidari, J. Esposito, A. Caissutti. Kalkitoxin Time-Resolved Absorption and Resonance FT-IR and Raman Biospectroscopy and Density Functional Theory (DFT) Investigation of Vibronic-Mode Coupling Structure in Vibrational Spectra Analysis. Can J Biomed Res & Tech., 2019, 2(1): 1-21.

[282] A. Heidari, J. Esposito, A. Caissutti. Neosaxitoxin Time-Resolved Absorption and Resonance FT-IR and Raman Biospectroscopy and Density Functional Theory (DFT) Investigation of Vibronic-Mode Coupling Structure in Vibrational Spectra Analysis. Clin Case Studie Rep., 2019, 2(3): 1-14.

[283] A. Heidari, J. Esposito, A. Caissutti. 6-Methoxy-8-[[6-Methoxy-8-[[6-Methoxy-2-Methyl-1-(2-Methylpropyl)-3,4-Dihydro-1H-Isoquinolin-7-yl] Oxy]-2-Methyl-1-(2-Methylpropyl)-3,4-Dihydro-1H-Isoquinolin-7-yl]Oxy]-2-Methyl-1-(2-Methylpropyl)-3,4-Dihydro-1H-Isoquinolin-7-ol Time-Resolved Absorption and Resonance FT-IR and Raman Biospectroscopy and Density Functional Theory (DFT) Investigation of Vibronic-Mode Coupling Structure in Vibrational Spectra Analysis. Clin Case Studie Rep., 2019, 2(3): 1-14.

[284] A. Heidari. Comparison of Synchrotron Radiation and Synchrocyclotron Radiation Performance in Monitoring of Human Cancer Cells, Tissues and Tumors. Clin Case Studie Rep., 2019, 2(3): 1-12.

[285] A. Heidari, J. Esposito, A. Caissutti. Kalkitoxin Time-Resolved Absorption and Resonance FT-IR and Raman Biospectroscopy and Density Functional Theory (DFT) Investigation of Vibronic-Mode Coupling Structure in Vibrational Spectra Analysis. Clin Case Studie Rep., 2019, 2(3): 1-14.

[286] A. Heidari, J. Esposito, A. Caissutti. Diphtheria Toxin Time-Resolved Absorption and Resonance FT-IR and Raman Biospectroscopy and Density Functional Theory (DFT) Investigation of Vibronic-Mode Coupling Structure in Vibrational Spectra Analysis: A Spectroscopic Study on an Anti-Cancer Drug. Clin Case Studie Rep., 2019, 2(3): 1-14.

[287] A. Heidari, J. Esposito, A. Caissutti. Symbiodinolide Time-Resolved Absorption and Resonance FT-IR and Raman Biospectroscopy and Density Functional Theory (DFT) Investigation of Vibronic-Mode Coupling Structure in Vibrational Spectra Analysis. Clin Case Studie Rep., 2019, 2(3): 1-14.

[288] A. Heidari, J. Esposito, A. Caissutti. Saxitoxin Time-Resolved Absorption and Resonance FT-IR and Raman Biospectroscopy and Density Functional Theory Investigation of Vibronic-Mode Coupling Structure in Vibrational Spectra Analysis. Am J Exp Clin Res., 2019, 6(4): 364-377.

[289] R. Gobato, M. R. R. Gobato, A. Heidari, A. Mitra. Hartree-Fock Methods Analysis Protonated Rhodochrosite Crystal and Potential in the Elimination of Cancer Cells through Synchrotron Radiation, 2019, 5(3): 27-36.

[290] R. Gobato, I. K. K. Dosh, A. Heidari, A. Mitra, M. R. R. Gobato. Perspectives on the Elimination of Cancer Cells Using Rhodochrosite Crystal Through Synchrotron Radiation, and Absorption the Tumoral and Non-Tumoral Tissues. Arch Biomed Eng & Biotechnol., 2019, 3(2): 1-2.

[291] R. Gobato, M. R. R. Gobato, A. Heidari, A. Mitra. Unrestricted Hartree-Fock Computational Simula-

 DOI: https://doi.org/10.30564/ssid.v1i2.1827

tion in a Protonated Rhodochrosite Crystal. Phys Astron Int J., 2019, 3(6): 220-228.

[292] A. Heidari, K. Schmitt, M. Henderson, E. Besana. Perspectives on Sub-Nanometer Level of Electronic Structure of the Synchrotron with Mendelevium Nanoparticles for Elimination of Human Cancer Cells, Tissues and Tumors Treatment Using Mathematica 12.0. Journal of Energy Conservation, 2019, 1(2): 46-73.

[293] A. Heidari, K. Schmitt, M. Henderson, E. Besana. Simulation of Interaction of Synchrotron Radiation Emission as a Function of the Beam Energy and Bohrium Nanoparticles Using 3D Finite Element Method (FEM) as an Optothermal Human Cancer Cells, Tissues and Tumors Treatment. Current Research in Biochemistry and Molecular Biology, 2019, 1(1), 17-44.

[294] A. Heidari, K. Schmitt, M. Henderson, E. Besana. Investigation of Interaction between Synchrotron Radiation and Thulium Nanoparticles for Human Cancer Cells, Tissues and Tumors Treatment. European Journal of Scientific Exploration, 2019, 2(3): 1-8.

[295] A. Heidari, K. Schmitt, M. Henderson, E. Besana. The Effectiveness of the Treatment Human Cancer Cells, Tissues and Tumors Using Darmstadtium Nanoparticles and Synchrotron Radiation. International Journal of Advanced Engineering and Science, 2020, 9(1): 9-39.

[296] A. Heidari, K. Schmitt, M. Henderson, E. Besana. Using 3D Finite Element Method (FEM) as an Optothermal Human Cancer Cells, Tissues and Tumors Treatment in Simulation of Interaction of Synchrotron Radiation Emission as a Function of the Beam Energy and Uranium Nanoparticles. Nano Prog., 2019, 1(2): 1-6.

[297] A. Heidari, K. Schmitt, M. Henderson, E. Besana. A New Approach to Interaction between Beam Energy and Erbium Nanoparticles. Saudi J Biomed Res., 2019, 4(11): 372-396.

[298] A. Heidari, K. Schmitt, M. Henderson, E. Besana. Consideration of Energy Functions and Wave Functions of the Synchrotron Radiation and Samarium Nanoparticles Interaction During Human Cancer Cells, Tissues and Tumors Treatment Process. Sci. Int. (Lahore), 2019, 31(6), 885-908.

[299] A. Heidari, K. Schmitt, M. Henderson, E. Besana. An Outlook on Optothermal Human Cancer Cells, Tissues and Tumors Treatment Using Lanthanum Nanoparticles under Synchrotron Radiation. Journal of Materials Physics and Chemistry, 2019, 7(1): 29-45.

[300] A. Heidari, K. Schmitt, M. Henderson, E. Besana. Effectiveness of Einsteinium Nanoparticles in Optothermal Human Cancer Cells, Tissues and Tumors Treatment under Synchrotron Radiation. Journal of Analytical Oncology, 2019, 8(1): 43-62.

[301] A. Heidari, K. Schmitt, M. Henderson, E. Besana. Study of Relation between Synchrotron Radiation and Dubnium Nanoparticles in Human Cancer Cells, Tissues and Tumors Treatment Process. Int. Res. J. Applied Sci., 2019, 1(4): 1-20.

[302] A. Heidari, K. Schmitt, M. Henderson, E. Besana. A Novel Prospect on Interaction of Synchrotron Radiation Emission and Europium Nanoparticles for Human Cancer Cells, Tissues and Tumors Treatment. European Modern Studies Journal, 2019, 3(5): 11-24.

[303] A. Heidari, K. Schmitt, M. Henderson, E. Besana. Advantages, Effectiveness and Efficiency of Using Neodymium Nanoparticles by 3D Finite Element Method (FEM) as an Optothermal Human Cancer Cells, Tissues and Tumors Treatment under Synchrotron Radiation. International Journal of Advanced Chemistry, 2019, 7(2): 119-135.

[304] A. Heidari, K. Schmitt, M. Henderson, E. Besana. Role and Applications of Promethium Nanoparticles in Human Cancer Cells, Tissues and Tumors Treatment. Scientific Modelling and Research, 2019, 4(1): 8-14.

[305] A. Heidari, J. Esposito, A. Caissutti. Maitotoxin Time-Resolved Absorption and Resonance FT-IR and Raman Biospectroscopy and Density Functional Theory (DFT) Investigation of Vibronic-Mode Coupling Structure in Vibrational Spectra Analysis: A Spectroscopic Study on an Anti-Cancer Drug. Glob Imaging Insights, 2019, 4(2): 1-13.

[306] A. Heidari, J. Esposito, A. Caissutti. Biotoxin Time-Resolved Absorption and Resonance FT-IR and Raman Biospectroscopy and Density Functional Theory (DFT) Investigation of Vibronic-Mode Coupling Structure in Vibrational Spectra Analysis. Glob Imaging Insights, 2019, 4(2): 1-14.

[307] A. Heidari, J. Esposito, A. Caissutti: Time-Resolved Resonance FT-IR and Raman Spectroscopy and Density Functional Theory Investigation of Vibronic-Mode Coupling Structure in Vibrational Spectra of Nanopolypeptide Macromolecule beyond the Multi-Dimensional Franck-Condon Integrals Approximation and Density Matrix Method. Glob Imaging Insights, 2019, 4(2): 1-14.

[308] A. Heidari, J. Esposito, A. Caissutti. Cholera Toxin Time-Resolved Absorption and Resonance FT-IR and Raman Biospectroscopy and Density Functional

DOI: https://doi.org/10.30564/ssid.v1i2.1827

Theory (DFT) Investigation of Vibronic-Mode Coupling Structure in Vibrational Spectra Analysis. Glob Imaging Insights, 2019, 4(2): 1-14.

[309] A. Heidari, J. Esposito, A. Caissutti. Nodularin Time-Resolved Absorption and Resonance FT-IR and Raman Biospectroscopy and Density Functional Theory (DFT) Investigation of Vibronic-Mode Coupling Structure in Vibrational Spectra Analysis. Glob Imaging Insights, 2019, 4(2): 1-14.

[310] A. Heidari, J. Esposito, A. Caissutti. Cangitoxin Time-Resolved Absorption and Resonance FT-IR and Raman Biospectroscopy and Density Functional Theory (DFT) Investigation of Vibronic-Mode Coupling Structure in Vibrational Spectra Analysis. Glob Imaging Insights, 2019, 4(2): 1-13.

[311] A. Heidari, J. Esposito, A. Caissutti. Ciguatoxin Time-Resolved Absorption and Resonance FT-IR and Raman Biospectroscopy and Density Functional Theory (DFT) Investigation of Vibronic-Mode Coupling Structure in Vibrational Spectra Analysis. Glob Imaging Insights, 2019, 4(2): 1-14.

[312] A. Heidari, J. Esposito, A. Caissutti. Brevetoxin (a) and (b) Time-Resolved Absorption and Resonance FT-IR and Raman Biospectroscopy and Density Functional Theory (DFT) Investigation of Vibronic-Mode Coupling Structure in Vibrational Spectra Analysis: A Spectroscopic Study on an Anti-HIV Drug. Cientific Drug Delivery Research, 2019, 1(2): 11-16.

[313] A. Heidari, J. Esposito, A. Caissutti. Cobrotoxin Time-Resolved Absorption and Resonance FT-IR and Raman Biospectroscopy and Density Functional Theory (DFT) Investigation of Vibronic-Mode Coupling Structure in Vibrational Spectra Analysis. Trends in Res., 2019, 3(1): 1-13.

[314] A. Heidari, J. Esposito, A. Caissutti. Cylindrospermopsin Time-Resolved Absorption and Resonance FT-IR and Raman Biospectroscopy and Density Functional Theory (DFT) Investigation of Vibronic-Mode Coupling Structure in Vibrational Spectra Analysis. Trends in Res., 2019, 3(1): 1-14.

[315] A. Heidari, J. Esposito, A. Caissutti. Anthrax Toxin Time-Resolved Absorption and Resonance FT-IR and Raman Biospectroscopy and Density Functional Theory (DFT) Investigation of Vibronic-Mode Coupling Structure in Vibrational Spectra Analysis. Trends in Res., 2019, 3(1): 1-14.

[316] A. Heidari, K. Schmitt, M. Henderson, E. Besana. Investigation of Moscovium Nanoparticles as Anti-Cancer Nano Drugs for Human Cancer Cells, Tissues and Tumors Treatment. Elixir Appl. Chem., 2019, 137A: 53943-53963.

[317] A. Heidari, K. Schmitt, M. Henderson, E. Besana. Study of Function of the Beam Energy and Holmium Nanoparticles Using 3D Finite Element Method (FEM) as an Optothermal Human Cancer Cells, Tissues and Tumors Treatment. European Journal of Advances in Engineering and Technology, 2019, 6(12): 34-62.

[318] A. Heidari, K. Schmitt, M. Henderson, E. Besana. Human Cancer Cells, Tissues and Tumors Treatment Using Dysprosium Nanoparticles. Asian J. Mat. Chem., 2019, 4(3-4): 47-51.

[319] A. Heidari, K. Schmitt, M. Henderson, E. Besana. Simulation of Interaction of Synchrotron Radiation Emission as a Function of the Beam Energy and Plutonium Nanoparticles Using 3D Finite Element Method (FEM) as an Optothermal Human Cancer Cells, Tissues and Tumors Treatment. J. Cancer Research and Cellular Therapeutics, 2019, 2(4): 1-19.

[320] A. Heidari, K. Schmitt, M. Henderson, E. Besana. Study of Gadolinium Nanoparticles Delivery Effect on Human Cancer Cells, Tissues and Tumors Treatment under Synchrotron Radiation. Applied Chemistry, 2019, 2(2): 55-97.

[321] A. Heidari, K. Schmitt, M. Henderson, E. Besana, R. Gobato. Pros and Cons of Livermorium Nanoparticles for Human Cancer Cells, Tissues and Tumors Treatment under Synchrotron Radiation Using Mathematica 12.0. Parana Journal of Science and Education (PJSE), 2020, 6(1): 1-31.

[322] R. Gobato, M. R. R. Gobato, A. Heidari, A. Mitra. Challenging Giants. Hartree-Fock Methods Analysis Protonated Rhodochrosite Crystal and Potential in the Elimination of Cancer Cells Through Synchrotron Radiation. Biomed J Sci & Tech Res., 2020, 25(1): 18843-18848.

[323] A. Heidari, K. Schmitt, M. Henderson, E. Besana. Simulation of Interaction between Ytterbium Nanoparticles and Human Gum Cancer Cells, Tissues and Tumors Treatment under Synchrotron Radiation. Dent Oral Maxillofac Res., 2019, 5(5): 1-18.

[324] A. Heidari, K. Schmitt, M. Henderson, E. Besana. Modelling of Interaction between Curium Nanoparticles and Human Gum Cancer Cells, Tissues and Tumors Treatment under Synchrotron Radiation. Dent Oral Maxillofac Res. , 2019, 5(5): 1-18.

[325] A. Heidari, K. Schmitt, M. Henderson, E. Besana. Study of Berkelium Nanoparticles Delivery Effectiveness and Efficiency on Human Gum Cancer Cells, Tissues and Tumors Treatment under Synchrotron Radiation. Dent Oral Maxillofac Res., 2019, 5(5): 1-18.

[326] A. Heidari, K. Schmitt, M. Henderson, E. Besana.

 DOI: https://doi.org/10.30564/ssid.v1i2.1827

Fermium Nanoparticles Delivery Mechanism in Human Gum Cancer Cells, Tissues and Tumors Treatment under Synchrotron Radiation. Dent Oral Maxillofac Res., 2019, 5(5): 1-17.

[327] A. Heidari, K. Schmitt, M. Henderson, E. Besana. Advantages of Lawrencium Nanoparticles for Human Gum Cancer Cells, Tissues and Tumors Treatment under Synchrotron Radiation. Dent Oral Maxillofac Res., 2019, 5(5): 1-18.

[328] A. Heidari, K. Schmitt, M. Henderson, E. Besana. Pros and Cons of the Roentgenium Nanoparticles for Human Gum Cancer Cells, Tissues and Tumors Treatment under Synchrotron Radiation. Dent Oral Maxillofac Res., 2019, 5(5): 1-17.

[329] A. Heidari, K. Schmitt, M. Henderson, E. Besana. Imagery of Flerovium Nanoparticles Delivery Process in Human Gum Cancer Cells, Tissues and Tumors Treatment under Synchrotron Radiation. Dent Oral Maxillofac Res., 2019, 5(5): 1-18.

[330] A. Heidari, J. Esposito, A. Caissutti. Maitotoxin Time-Resolved Absorption and Resonance FT-IR and Raman Biospectroscopy and Density Functional Theory (DFT) Investigation of Vibronic-Mode Coupling Structure in Vibrational Spectra Analysis: A Spectroscopic Study on an Anti-Gum Cancer Drug. Dent Oral Maxillofac Res., 2019, 5(5): 1-16.

[331] A. Heidari, J. Esposito, A. Caissutti. Batrachotoxin Time-Resolved Absorption and Resonance FT-IR and Raman Biospectroscopy and Density Functional Theory (DFT) Investigation of Vibronic-Mode Coupling Structure in Vibrational Spectra Analysis: A Spectroscopic Study on an Anti-Gum Cancer Drug. Dent Oral Maxillofac Res., 2019, 5(6): 1-16.

[332] A. Heidari, K. Schmitt, M. Henderson, E. Besana. Hafnium Nanoparticles and Their Roles and Applications in Human Gum Cancer Cells, Tissues and Tumors Treatment under Synchrotron Radiation. Dent Oral Maxillofac Res., 2019, 5(6): 1-17.

[333] A. Heidari, K. Schmitt, M. Henderson, E. Besana. Dramaturgy of Technetium Nanoparticles Delivery Process in Human Gum Cancer Cells, Tissues and Tumors Treatment under Synchrotron Radiation. Dent Oral Maxillofac Res., 2019, 5(6): 1-19.

[334] A. Heidari, K. Schmitt, M. Henderson, E. Besana. Computational Approach to Interaction between Synchrotron Radiation Emission as a Function of the Beam Energy and Ruthenium Nanoparticles in Human Gum Cancer Cells, Tissues and Tumors Treatment. Dent Oral Maxillofac Res., 2019, 5(6): 1-18.

[335] A. Heidari, K. Schmitt, M. Henderson, E. Besana. Appearance Check of Rhodium Nanoparticles Delivery Trend in Human Gum Cancer Cells, Tissues and Tumors Treatment under Synchrotron Radiation. Dent Oral Maxillofac Res., 2019, 5(6): 1-19.

[336] A. Heidari, K. Schmitt, M. Henderson, E. Besana. Orientation Rhenium Nanoparticles Delivery Target on Human Gum Cancer Cells, Tissues and Tumors under Synchrotron Radiation. Dent Oral Maxillofac Res., 2019, 5(6): 1-18.

[337] A. Heidari, K. Schmitt, M. Henderson, E. Besana. Drug Delivery Systems (DDSs) of Osmium Nanoparticles on Human Gum Cancer Cells, Tissues and Tumors Treatment under Synchrotron Radiation. Dent Oral Maxillofac Res., 2019, 5(6): 1-18.

[338] A. Heidari, K. Schmitt, M. Henderson, E. Besana. Development of Successful Formulations for Oral Drug Delivery Concepts of Iridium Nanoparticles in Human Gum Cancer Cells, Tissues and Tumors Treatment under Synchrotron Radiation. Dent Oral Maxillofac Res., 2019, 5(6): 1-19.

[339] A. Heidari, K. Schmitt, M. Henderson, E. Besana. Classification of Drug Delivery System of Niobium Nanoparticles in Human Gum Cancer Gum Cells, Tissues and Tumors Treatment under Synchrotron Radiation. Dent Oral Maxillofac Res., 2020, 6(1): 1-17.

[340] A. Heidari, K. Schmitt, M. Henderson, E. Besana. Types of Drug Delivery System Slideshare of Protactinium Nanoparticles in Human Gum Cancer Cells, Tissues and Tumors Treatment under Synchrotron Radiation. Dent Oral Maxillofac Res., 2020, 6(1): 1-17.

[341] A. Heidari, K. Schmitt, M. Henderson, E. Besana. New Drug Delivery System in Pharmaceutics of Neptunium Nanoparticles in Human Gum Cancer Cells, Tissues and Tumors Treatment under Synchrotron Radiation. Dent Oral Maxillofac Res., 2020, 6(1): 1-18.

[342] A. Heidari, K. Schmitt, M. Henderson, E. Besana. Drug Delivery Describes the Method and Approach to Delivering Drugs or Pharmaceuticals and Other Xenobiotics to Their Site of Action within Radon Nanoparticles Effects on Human Gum Cancer Cells, Tissues and Tumors Treatment under Synchrotron Radiation. Dent Oral Maxillofac Res., 2020, 6(1): 1-18.

[343] A. Heidari, K. Schmitt, M. Henderson, E. Besana. Applications of Oganesson Nanoparticles in Increasing Rapidly with the Promise of Targeted and Efficient Drug Delivery in Human Gum Cancer Cells, Tissues and Tumors Treatment under Synchrotron Radiation. Dent Oral Maxillofac Res., 2020, 6(1): 1-19.

DOI: https://doi.org/10.30564/ssid.v1i2.1827

[344] A. Heidari, K. Schmitt, M. Henderson, E. Besana. Wheeler-Feynman Time- Symmetric Study of Effectiveness and Efficiency of Terbium Nanoparticles Delivery Mechanism in Human Cancer Cells, Tissues and Tumors under Synchrotron Radiation. Frontiers Drug Chemistry Clinical Res., 2020, 3(1): 1-13.

[345] A. Heidari, K. Schmitt, M. Henderson, E. Besana. Simulation of Interaction of Synchrotron Radiation Emission as a Function of the Beam Energy and Californium Nanoparticles Using 3D Finite Element Method (FEM) as an Optothermal Human Cancer Cells, Tissues and Tumors Treatment. Oncol Res: Open Acce., 2019, 1(1): 1-17.

[346] A. Heidari. Market Analysis of Glycobiology and Glycochemistry 2020. J Genet Disor Genet Rep., 2019, 8: 1.

[347] A. Heidari, K. Schmitt, M. Henderson, E. Besana. Synchrotron Radiation Emission as a Function of the Beam Energy and Thorium Nanoparticles. International Medicine, 2020, 2(1): 67-73.

[348] A. Heidari, K. Schmitt, M. Henderson, E. Besana. Stochastic Study of Relativistic Lutetium Nanoparticles Moving in a Quantum Field of Synchrotron Radiation Emission When Charged Lutetium Nanoparticles Are Accelerated Radially in Human Cancer Cells, Tissues and Tumors Treatment. Frontiers Drug Chemistry Clinical Res., 2020, 3(1): 1-15.

[349] A. Heidari, A. Caissutti, M. Henderson, K. Schmitt, E. Besana, J. Esposito, V. Peterson. Recent New Results and Achievements of California South University (CSU) BioSpectroscopy Core Research Laboratory for COVID-19 or 2019-nCoV Treatment: Diagnosis and Treatment Methodologies of "Coronavirus. Journal of Current Viruses and Treatment Methodologies, 2020, 1(1): 3-41.

[350] A. Heidari, K. Schmitt, M. Henderson, E. Besana. Study of Human Cancer Cells, Tissues and Tumors Treatment Through Interaction Between Synchrotron Radiation and Cerium Nanoparticles. Sci Lett., 2020, 8(1): 7-17.

[351] A. Heidari, K. Schmitt, M. Henderson, E. Besana. Study of Characteristic Polarization and the Frequencies Generated in Interaction of Synchrotron Radiation Emission and Actinium Nanoparticles in Human Cancer Cells, Tissues and Tumors Treatment Process. Parana Journal of Science and Education (PJSE), 2020, 6(3): 13-47.

[352] A. Heidari, K. Schmitt, M. Henderson, E. Besana. Californium Nanoparticles and Human Cancer Treatment: Commemorating the 100 th (1920-2020) Anniversary of the California South University (CSU). Parana Journal of Science and Education (PJSE), 2020, 6(3): 48-83.

[353] R. Gobato, M. R. R. Gobato, A. Heidari, A. Mitra, I. K. K. Dosh. Secret Messages in Enigmatic Playful Texts. ABEB., 2020, 4(2): 1-10.

[354] A. Heidari, K. Schmitt, M. Henderson, E. Besana. A Chemical Review on Cancer Immunology and Immunodeficiency. International Journal of Advanced Chemistry, 2020, 8(1): 27-43.

[355] A. Heidari, V. Peterson. A Comprehensive Review on Functional Roles of Cancerous Immunoglobulins and Potential Applications in Cancer Immunodiagnostics and Immunotherapy. International Journal of Advanced Chemistry, 2020, 8(1): 44-58.

[356] A. Heidari, V. Peterson. An Encyclopedic Review on Stereotactic Hypofractionated Radiotherapy, Re-Irradiation and Cancer Genome Research. International Journal of Advanced Chemistry, 2020, 8(1): 59-74.

[357] A. Heidari, V. Peterson. A Pervasive Review on Biomarker in Cervical Intraepithelial Lesions and Carcinoma. International Journal of Advanced Chemistry, 2020, 8(1): 75-88.

[358] A. Heidari. Future Advanced Study of Thin Layers of DNA/RNA Hybrid Molecule Nanostructure. J Mol Nanot Nanom, 2020, 2(1): 110.

 DOI: https://doi.org/10.30564/ssid.v1i2.1827

Author Guidelines

This document provides some guidelines to authors for submission in order to work towards a seamless submission process. While complete adherence to the following guidelines is not enforced, authors should note that following through with the guidelines will be helpful in expediting the copyediting and proofreading processes, and allow for improved readability during the review process.

Ⅰ. Format

- Program: Microsoft Word (preferred)
- Font: Times New Roman
- Size: 12
- Style: Normal
- Paragraph: Justified
- Required Documents

Ⅱ. Cover Letter

All articles should include a cover letter as a separate document.

The cover letter should include:

- Names and affiliation of author(s)

The corresponding author should be identified.

Eg. Department, University, Province/City/State, Postal Code, Country

- A brief description of the novelty and importance of the findings detailed in the paper

Declaration

v Conflict of Interest

Examples of conflicts of interest include (but are not limited to):

- Research grants
- Honoria
- Employment or consultation
- Project sponsors
- Author’s position on advisory boards or board of directors/management relationships
- Multiple affiliation
- Other financial relationships/support
- Informed Consent

This section confirms that written consent was obtained from all participants prior to the study.

- Ethical Approval

Eg. The paper received the ethical approval of XXX Ethics Committee.

- Trial Registration

Eg. Name of Trial Registry: Trial Registration Number

- Contributorship

The role(s) that each author undertook should be reflected in this section. This section affirms that each credited author has had a significant contribution to the article.

1. Main Manuscript
2. Reference List
3. Supplementary Data/Information

Supplementary figures, small tables, text etc.

As supplementary data/information is not copyedited/proofread, kindly ensure that the section is free from errors, and is presented clearly.

Ⅲ. Abstract

A general introduction to the research topic of the paper should be provided, along with a brief summary of its main results and implications. Kindly ensure the abstract is self-contained and remains readable to a wider audience. The abstract should also be kept to a maximum of 200 words.

Authors should also include 5-8 keywords after the abstract, separated by a semi-colon, avoiding the words already used in the title of the article.

Abstract and keywords should be reflected as font size 14.

Ⅳ. Title

The title should not exceed 50 words. Authors are encouraged to keep their titles succinct and relevant.

Titles should be reflected as font size 26, and in bold type.

Ⅳ. Section Headings

Section headings, sub-headings, and sub-subheadings should be differentiated by font size.

Section Headings: Font size 22, bold type

Sub-Headings: Font size 16, bold type

Sub-Subheadings: Font size 14, bold type

Main Manuscript Outline

Ⅴ. Introduction

The introduction should highlight the significance of the research conducted, in particular, in relation to current state of research in the field. A clear research objective should be conveyed within a single sentence.

Ⅵ. Methodology/Methods

In this section, the methods used to obtain the results in the paper should be clearly elucidated. This allows readers to be able to replicate the study in the future. Authors should ensure that any references made to other research or experiments should be clearly cited.

Ⅶ. Results

In this section, the results of experiments conducted should be detailed. The results should not be discussed at length in

this section. Alternatively, Results and Discussion can also be combined to a single section.

Ⅷ. Discussion

In this section, the results of the experiments conducted can be discussed in detail. Authors should discuss the direct and indirect implications of their findings, and also discuss if the results obtain reflect the current state of research in the field. Applications for the research should be discussed in this section. Suggestions for future research can also be discussed in this section.

Ⅸ. Conclusion

This section offers closure for the paper. An effective conclusion will need to sum up the principal findings of the papers, and its implications for further research.

Ⅹ. References

References should be included as a separate page from the main manuscript. For parts of the manuscript that have referenced a particular source, a superscript (ie. [x]) should be included next to the referenced text.

[x] refers to the allocated number of the source under the Reference List (eg. [1], [2], [3])

In the References section, the corresponding source should be referenced as:

[x] Author(s). Article Title [Publication Type]. Journal Name, Vol. No., Issue No.: Page numbers. (DOI number)

Ⅺ. Glossary of Publication Type

J = Journal/Magazine

M = Monograph/Book

C = (Article) Collection

D = Dissertation/Thesis

P = Patent

S = Standards

N = Newspapers

R = Reports

Kindly note that the order of appearance of the referenced source should follow its order of appearance in the main manuscript.

Graphs, Figures, Tables, and Equations

Graphs, figures and tables should be labelled closely below it and aligned to the center. Each data presentation type should be labelled as Graph, Figure, or Table, and its sequence should be in running order, separate from each other.

Equations should be aligned to the left, and numbered with in running order with its number in parenthesis (aligned right).

Ⅻ. Others

Conflicts of interest, acknowledgements, and publication ethics should also be declared in the final version of the manuscript. Instructions have been provided as its counterpart under Cover Letter.

About the Publisher

Bilingual Publishing Co. (BPC) is an international publisher of online, open access and scholarly peer-reviewed journals covering a wide range of academic disciplines including science, technology, medicine, engineering, education and social science. Reflecting the latest research from a broad sweep of subjects, our content is accessible world-wide——both in print and online.

BPC aims to provide an analytics as well as platform for information exchange and discussion that help organizations and professionals in advancing society for the betterment of mankind. BPC hopes to be indexed by well-known databases in order to expand its reach to the science community, and eventually grow to be a reputable publisher recognized by scholars and researchers around the world.

BPC adopts the Open Journal Systems, see on ojs.bilpublishing.com

Database Inclusion

Asia & Pacific Science Citation Index

Creative Commons

China National Knowledge Infrastructure

Google Scholar

Crossref

MyScienceWork

BILINGUAL
PUBLISHING CO.
Pioneer of Global Academics Since 1984

Tel:+65 65881289
E-mail:contact@bilpublishing.com
Website:www.bilpublishing.com